THESIS FOR THE DEGREE OF DOCTOR OF PHILOSOPHY

Ageing in Commercial Li-ion Batteries: Lifetime Testing and Modelling for Electrified Vehicle Applications

Evelina Wikner

Division of Electric Power Engineering
Department of Electrical Engineering
CHALMERS UNIVERSITY OF TECHNOLOGY
Göteborg, Sweden 2019

Ageing in Commercial Li-ion Batteries:
Lifetime Testing and Modelling for
Electrified Vehicle Applications
Evelina Wikner
ISBN 978-91-7905-166-2

Doktorsavhandlingar vid Chalmers tekniska högskola
Ny serie nr. 4633
ISSN 0346-718X

Division of Electric Power Engineering
Department of Electrical Engineering
CHALMERS UNIVERSITY OF TECHNOLOGY
SE-412 96 Göteborg
Sweden
Telephone + 46 (0)31 772 1000

Printed by Chalmers Reproservice
Göteborg, Sweden 2019

"As always in life, people want a simple answer . . .
and it's always wrong."

Susan Greenfield, neurochemist

Ageing in Commercial Li-ion Batteries:
Lifetime Testing and Modelling for Electrified Vehicle Applications
Evelina Wikner
Division of Electric Power Engineering
Chalmers University of Technology

Abstract

In this thesis, ageing in a commercial pouch cell for vehicle application is investigated through lifetime testing and modelling. The lifetime tests investigate the impact of temperature, current, depth of discharge (DOD) and state of charge (SOC).

Results from lifetime tests are used in the development of an empirical ageing model, to study the ageing as a result of different user cases in a vehicle application. The results showed that the battery lifetime in a vehicle application could be prolonged, without interfering with the driving itself, by better planning of the charging.

Lifetime test results and ageing analysis of the tested cells are used as guidance for the development of a physics-based ageing model. The model includes capacity loss and resistance increase due to resistive film formation and loss of active material.

The lifetime test results showed that for the studied cell, staying below 40% SOC level will improve the lifetime considerably. This was seen in both the calendar ageing tests and the cycling ageing tests. The lifetime tests performed in small SOC intervals at different SOC levels showed that the ageing is separated into two groups, with more pronounced ageing at high SOC and less ageing at low SOC.

The main ageing contribution is the growth of Solid Electrolyte Interphase (SEI), which is also the case seen in the model when using parameters for the SEI growth extracted from calendar ageing data. The more pronounced ageing at higher SOC levels can partly be explained by the SEI growth that is increased at higher SOC level and partly from the contribution of manganese dissolution. This was confirmed by Post Mortem (PM) analysis and successfully captured by the model.

Keywords: Plug-in Hybrid Electric Vehicle (PHEV), Battery lifetime tests, Calendar ageing, Physics-based modelling, Empiric model

Acknowledgements

I would like to begin to thank my family and friends, for the constant support and encouragement in perusing my goals, this thesis being one of them.

I'm very grateful to my main supervisor Prof. Torbjörn Thiringer, who is incredibly patient. He always finds the time to discuss problems and contemplations. My co-supervisor and project leader Dr. Johan Scheers has been a steady support providing structure, guidance and encouragement.

A special thanks to my colleagues at Electric Power Engineering for the open and welcoming working environment. Also for the interesting and fruitful/not so fruitful discussions. With you around, a grey day with a crashed simulation or failed test is so much easier to tackle.

I also would like to send a thanks to Dr. Erik Björklund for his work in the project. Without our combined effort I would not have come this far. It has been a great pleasure to cooperate with you.

Last also thank you Dr. Henrik Ekström for helping me improving my simulation skills, as well as contributing with extensive knowledge in electrochemistry.

Evelina Wikner
Göteborg, 2019

Preface

This thesis is a result of the project *Ageing mechanisms and how to prolong battery life in vehicles and energy storage applications* financed by the Swedish Energy Agency, through *Batterifonden*, in collaboration with ABB, Volvo Car Corporation (VCC) and Uppsala University (UU). Two PhD students have worked in the project together with senior researchers from the industry partners. The final year of the two PhD students (Evelina Wikner, Chalmers University of Technology, and Erik Björklund, UU) has been financed by two supportive 1-year grants from the Swedish Electromobility Centre (SEC).

Dr. Erik Björklund performed several measurements for parameterisation of the model and developed the model for electrode ageing analysis. He has also conducted all the post mortem analysis performed within the project. Further, UU has provided advice and expertise in electrochemical systems and of ageing mechanisms in batteries through Prof. Daniel Brandell and Prof. Kristina Edström.

The industry partners, ABB and VCC, have provided in-depth knowledge of the targeted applications, battery testing facilities, assistance in development of test regimes and test procedures. The extensive testing has been performed by Tomas Tengnér, Dr. Antonis Marinopoulos, Lukas Migas, Dr. Anneli Jedenmalm and Dr. Anna Andersson at ABB and by Johan Lesser and Michael Östrand at VCC.

VCC has been the project leader, where the project was started by Dr. Theresa Granérus and Dr. Henrik Markusson. Since 2017 Dr. Johan Scheers has taken over as the project leader and co-supervisor.

List of Publications

- E. Wikner, T. Thiringer, "Extending battery lifetime by avoiding high SOC", *Applied Sciences*, vol. 8, no. 10, 2018.
- E. Björklund, E. Wikner, R. Younesi, D. Brandell, K. Edström, "Influence of state-of-charge in commercial $LiNi_{0.33}Mn_{0.33}Co_{0.33}O_1/LiMn_2O_4$-graphite cells analyzed by synchrotron-based photoelectron spectroscopy", *J. Energy Storage*, vol. 15, pp. 172-180, 2018.
- E. Wikner, J. Lesser, T. Thiringer, "Accelerated lifetime testing in small SOC intervals on commercial pouch cells; challenges and countermeasures", *19th European Conference on Power Electronics and Applications (EPE'17 ECCE Europe) 2017.*
- E. Wikner, "Lithium ion Battery Aging: Battery Lifetime Testing and Physics-based Modeling for Electric Vehicle Applications", Licentiate Thesis, *Chalmers University of Technology (2017).*
- E. Wikner, "Effect of Intercalation Diffusivity When Simulating Mixed Electrode Materials in Li-Ion Batteries", *Proceedings of the 2016 COMSOL Conference in Munich 2016.*

Contents

List of Abbreviations

The following list presents abbreviations that are used throughout this thesis:

Li	Lithium
Mn	Manganese
LiB	Lithium ion Battery
Li^+	Lithium ion
Mn^{2+}	Manganese ion
BOL	Beginning of Life
MOL	Middle of Life
EOL	End of Life
SOC	State of Charge (0-100%)
SOL	State of Lithiation (0-100%)
OCV	Open Circuit Voltage
C-rate	C-rate is the rate at which a battery is completely discharged or charged in 1 h.
DOD	Depth of Discharge (0-100%)
FCE	Full Cycle Equivalent (Total current throughput over rated initial capacity)
CC	Constant Current
CV	Constant Voltage
RMS	Root Mean Square

LS	Least Square
SEI	Solid Electrolyte Interphase
CEI	Cathode Electrolyte Interphase
PHEV	Plug-in Hybrid Electric Vehicle
HEV	Hybrid Electric Vehicle
EV	Electric Vehicle
UU	Uppsala University
VCC	Volvo Car Corporation
SEC	Swedish Electromobility Centre
PE	Positive Electrode
NE	Negative Electrode
LTO	Lithium Titanium Oxide
NMC	Lithium Nickel Manganese Cobalt Oxide [$LiNi_xMn_yCo_zO_2$]
LMO	Lithium Manganese Oxide [$LiMn_2O_4$]
TM	Transition Metal
EC	Ethylene Carbonate
DMC	Dimethyl Carbonate
EMC	Ethyl Methyl Carbonate
ESW	Electrolyte stability window
LUMO	Lowest Unoccupied Molecular Orbital
HOMO	Highest Occupied Molecular Orbital
cc	Current Collector
RPT	Reference Performance Test
ICA	Incremental Capacity Analysis
GITT	Galvanostatic Intermittent Titration Technique
ESMLE	Electrode Slippage and Material Loss Estimation

EIS	Electrochemical Impedance Spectroscopy
PM	Post Mortem
XRD	X-Ray Diffraction
EDS	Energy-Dispersive X-ray Spectroscopy
SEM	Scanning Electron Microscope
XPS	X-Ray Photoelectron Spectroscopy
ICP-OES	Inductively Coupled Plasma–Optical Emission Spectrometry
GC-MS	Gas Chromatography—Mass Spectrometry
P2D	Physics-based Pseudo-2D model
FEM	Finite Element Method
BDF	Backward Differentiation Formulas
PDE	Partial Differential Equations
B-V	Butler-Volmer
es	Electronic State

List of Symbols

subscript $+/-$	Li^+/PF_6^-
subscript a/c	anodic/cathodic reaction
subscript s/l	solid/liquid
subscript p	Product
A_0	Pre-exponential factor
a_+	Relative activity
c	Concentration
c_{solv}	Solvent concentration
c_T	Total concentration
C_{dl}	Double layer capacitance
d_{SEI}	SEI thickness
D	Diffusivity
E_0	Activation energy
E_{eq}	Equilibrium potential
F	Faraday's constant
$f_\pm$	Salt mean molar activity coefficient
f	Fraction
i	Current density
i_0	Exchange current density

K	Empiric rate constant for change in ionic conductivity
k	Reaction rate
k_{iso}	Material loss enhancement coefficient
L	Length
M	Molar mass
N	Molar flux
n	Number of electrons
R	Gas constant
R_{film}	Film resistance $[\Omega/m^2]$
r_p	Particle radius
$\mathbf{S}$	Solvent
$\mathbf{S}^{',''',''''}$	Decomposed Solvent
S_a	Specific surface area
T	Temperature
t	Time
t_+	Transport number for Li^+ (Also called transference number)
u	Ionic mobility
V_m	Partial molar volume
V_{ov}	Open-circuit voltage
$\mathbf{v}$	Fluid velocity
z	Ionic charge
Q	Capacity
α	Reaction rate coefficient
β	Bruggeman coefficient
ϵ	Volume fraction

η	Activation overpotential
$\nu_{reactions}$	Reaction product, moles
$\nu_{+/-}$	Number of cations and anions formed when 1 mol salt dissolves
σ	Conductivity of solid material
κ	Conductivity of electrolyte
μ	Electrochemical potential
ϕ	Electric potential
$\Delta\phi_{film}$	Voltage drop over resistive film

Chapter 1

Introduction

1.1 Background

Electrification of vehicles is seen as one of the key solutions in reducing emissions from the transport sector. In particular, the tail-pipe emissions can be reduced, which is very important in most large cities. Today the transport sector is a major contributor to air pollution in cities and is responsible for almost a quarter of the total greenhouse gas emissions in Europe [1].

Electric vehicles (EVs) is not a new invention, in the late 19th and early 20th century they were the most common vehicles. They were very popular for being quiet and relatively easy to operate compared to the combustion vehicles, but were soon out-competed by the combustion vehicles due to shorter drive range and being more expensive to buy [2].

During the last decade, EVs have started to reappear due to the strong developments in battery technology that have revolutionised our society. Since 1991, when Sony introduced the first commercial lithium ion batteries (LiBs) [3], the number of possible applications have constantly increased.

The by far most common solution for EVs, Hybrid EVs (HEVs), and Plugin-HEVs (PHEVs) is to use LiBs for the on-board energy storage. The LiB is the most expensive component in the vehicle. Improved lifetime, by optimised usage of batteries in vehicles, facilitates a lower total cost of ownership. A deepened understanding of which current and power limits to use for the batteries is essential in order to prolong the lifetime. With improved understanding of the ageing, the trade-off between lifetime and usage can be balanced in an optimal way.

LiBs is today a mature battery technology, where the ageing mechanisms have been vastly studied [4–11]. However, still unanswered questions remain.

The number of different processes occurring and their complex coupling have made it difficult to construct a unified picture of the ageing processes. The consequence is that it is very difficult to correlate normal battery usage to a specific ageing process.

Physics-based models can be used to predict the battery behaviour and also to improve the understanding of the processes occurring in a battery [12–16]. These models have the potential to be a strong tool in connecting the effect of different ageing mechanisms to different usage [17–20].

Today, the development of physics-based ageing models requires correlation to expensive and time consuming lifetime tests, as well as difficult parameterisation. Thus, an ambition is that with continuous development of the models, in time, the required amount of lifetime tests could be reduced.

The initiative for improving the performance and at the same time reduce the cost for the LiBs is high. Improving the system efficiency will only result in a small cost saving. However, improving the performance and durability of the energy storage will have a large impact on the resulting cost.

1.2 Previous Work

The LiBs are continuously developed and improved, for each new battery chemistry extensive tests have to be performed to be able to estimate the ageing during operation. This is an expensive and time consuming task. Several empirical [21–23], semi-empirical [19, 24, 25] and circuit models [26] have been presented over the years. The downside of these models is that they are parameterised from extensive test matrices performed on the LiB to be modelled, thus are only applicable to that specific LiB. These models cannot simply be coupled to the electrochemical processes occurring in the battery during its lifetime.

To better understand the battery degradation, physics-based models are used to describe the underlying electrochemical processes. Physics-based models are used to describe the fundamental electrochemical processes taking place in a battery during operation. The foundation for this type of physics-based pseudo-2D models, generally referred to as P2D or Newman models, were introduced by Newman and Tiedemann in 1975 [12] and has since continuously been developed further [13, 14, 18, 27].

There are some different approaches described in the literature for simulating ageing. The most common is to simulate parasitic side reactions on the electrode materials, including resistive film growth and capacity fade due to the resistance increase and loss of lithium ions (Li^+) [16, 19, 28, 29]. Models including the effects of transition metal dissolution from the positive electrode [30] and in some cases also describing deposition on the negative

electrode [17, 31, 32] are also available in the literature. However, there are some diversity in the understanding of the details of this process. There are also some examples where the two above mentioned ageing mechanisms are combined [31,32]. However, how these two mechanisms influence one another has yet to be understood and included. Overall, there are many more ageing mechanisms occurring in the battery during use, and the complexity and inter-dependency of these make it difficult to account for the contribution from each mechanism.

A large drawback with the physics-based models is that they require a large number of material and design parameters. Due to different cell and material designs, there are large differences in the values reported for various parameters in the literature. This leads to large uncertainties in the parameter values. Schmalstieg et al. recently demonstrated how a large commercial cell can be parameterised for this type of model from various measurements [33, 34]. However, determining the parameters is a tedious and difficult task that requires several different types of experiments.

To estimate the parameters for various ageing processes is even more difficult, the material used and the electrolyte composition will highly influence how fast the cell will age. Lifetime tests can be used to find approximate values for some of the ageing parameters. Ecker et al. has demonstrated how ageing parameters can be estimated from calendar ageing tests on small commercial cells [35]. Another approach from Spotnitz et al. [36] is to develop polynomial expressions from empirical studies, estimating the irreversible and reversible Li^+ loss.

Furthermore, several of the models presented in the literature are based on lab-scale cells or small (mAh-Ah) commercial cells [14, 31, 35–38], which are not fully representative of large commercial cells for automotive applications. The need for lifetime testing of large commercial cells in correlation with physics-based models is therefore a key factor in further developing the understanding of battery cell ageing.

In this thesis, lifetime testing of large commercial cells is the foundation of the development of a physics-based ageing model. An important test series conducted here is a detailed study on how the state of charge (SOC) of the battery relates to the ageing. Only a few such studies have been published [22,26,35] and, in addition, only on small commercial cells. The information from this type of studies is highly valuable and have been used in the modelling development. The model includes two main ageing mechanisms; solid electrolyte interphase (SEI) growth and manganese (Mn) dissolution as well as coupling between the two.

1.3 Purpose of Work

To find the best LiB for an application requires not only knowledge of the LiB itself, but also an understanding for the application where it will be used. There is a need to combine these two fields. This project, combining the vehicle application with modelling, and experimental work on cell and material level has been a response to this need.

The understanding of ageing mechanisms occurring in controlled systems such as lab-scale and lab-prototype cells is fairly well developed. This thesis is an attempt to improve the understanding of ageing in mass-produced large LiBs used in electrified vehicles today, through a combination of experiments and model studies. To fulfil the purpose, the work was separated into a number of steps:

- Develop the test matrix and test regimes.
- Perform lifetime and characterisation tests.
- Analyse the test results.
- Develop an empirical model to study how the usage impacts the ageing.
- Set up and parameterise a physics-based battery ageing model.

The experiments consisted of lifetime tests to study the ageing at different conditions as well as characterisation measurements to extract parameters for the physics-based model. The physics-based ageing model was built for a large commercial pouch type LiB. The model is capable of studying the effects of SEI growth and Mn dissolution.

1.4 Contributions

This thesis has two main fields of focus, lifetime testing and physics-based ageing modelling. However, in the process to achieve this, several additional contributions were made:

- The life expectancy for large depth of discharge (DOD) was confirmed to be shorter in comparison to small DOD, where 10% DOD can more than double the lifetime.
- The ageing consequences for cells tested in 10% intervals of SOC were quantified at three different temperatures and it was shown that:

- The ageing trajectory for a small DOD has a different behaviour compared to that of a large DOD. While the ageing in large DODs accelerate with number of cycles, the ageing in small DODs seems to level out with very moderate ageing. Furthermore, it was established that the capacity loss before this moderate ageing is linked to the test regime and SOC level. It was also demonstrated that the fluctuation in the measured capacity for the small DODs was larger compared to that of the large DODs.
- Operating in SOC intervals lower than 30% SOC can significantly improve cyc lifetime with more than 3x the expected full cycle equivalent (FCE) lifetime, compared to 90% DOD operation using the same cycles.
- There is a large difference in ageing between the different 10% SOC intervals; at low SOC the ageing levelled out at 90-95% capacity retention and did not reach end of life (EOL) within 10000 FCEs, while at higher SOC ($\geq$50%) EOL was reached after approximately 2000-8000 FCEs depending on temperature and C-rate.
- The importance of temperature for 10% SOC intervals was proven to be small for intervals $\leq$50% SOC in contrast to larger DODs. The results presented here also show that a temperature close to 35°C is more beneficial compared to a temperature of 25°C.
- For SOC intervals above 60%, ageing increases with temperature.

- Lifetime test development:
  - A method for testing in small DODs, to maintain the targeted SOC interval, was developed and its effectiveness proven.
  - Automatised capacity checks to determine when a full Reference Performance Test (RPT) test should be performed were introduced to reduce the test time and operator supervision for tests with slow ageing.

- Experimental observations:
  - It is difficult to perform controlled accelerated lifetime tests without stressing the cell to unexpected ageing behaviour. Two duplicates were subject to a longer pause in the testing and showed a slightly improved lifetime.
  - It is difficult to account for the effects of breaks in long term testing due to planned or unplanned interrupts.

- An empirical model was developed to estimate ageing in a vehicle application due to drive and charge behaviour, including cycling ageing and calendar ageing. A case study demonstrated how the driver of an EV or PHEV can prolong the battery lifetime by simple adjustments of the charge and usage strategy.
- An electrochemically based ageing model was developed for lifetime prediction and its base functionalities were demonstrated. The model includes loss of recyclable Li^+ due to resistive film growth, loss of electrolyte volume in the electrode, Mn dissolution, and deposition.
  - The contributions of different ageing mechanism during various test regimes were quantified.
  - A linear time factor was introduced to reduce the required number of simulated cycles when performing ageing simulations and the accuracy demonstrated.
  - The sensitivity to various model parameters was quantified through a sensitivity analysis.
- Quantification of ageing using:
  - Potential curve analysis to estimate the electrode slippage and active material loss from the individual electrodes. The model for this was developed in corporation with Dr. Erik Björklund at Uppsala University (UU) who made the largest contribution. The model results were in coherence with results from the Post Mortem (PM) analysis; SEI growth with resulting impedance increase on the negative electrode (NE) and material loss from the PE dominates.

Chapter 2

Lithium ion Batteries and Battery Materials

LiBs is the collective name for a large family of batteries that operate by a similar mechanism. The term battery, in the automotive context, often refers to a complete battery system or pack, which includes packaging, cooling, wiring and monitoring of intermediate units called battery modules that host multiple LiB cells connected in parallel or series. The LiB cells themselves consist of multiple electrochemical cells stacked or rolled together and sealed in a rectangular hard (prismatic) or soft (pouch) aluminium casing, or less commonly in a hard cylindrical case. Depending of the size of the cells and the number of cells in parallel or series the capacity of a LiB can vary from mAh to MAh.

In this thesis, a 26 Ah LiB pouch cell with graphite, Lithium Manganese Oxide (LMO) and Lithium Nickel Manganese Cobalt Oxide (NMC) has been studied. The following chapter will give some background to LiBs in general although the focus is on the material pertinent to this study.

2.1 Lithium ion Batteries

LiBs is a chemical energy storage technology, transforming chemical energy to electricity through redox reactions. A comparison between different battery technologies is shown in Figure 2.1. The blue group shows the energy density range of LiB cells. The high energy density in relation to volume and weight is the reason for LiBs being used in a large range of different applications.

The three main components in a LiB, and what constitutes an electrochemical cell, is the NE, positive electrode (PE), and electrolyte. A separator

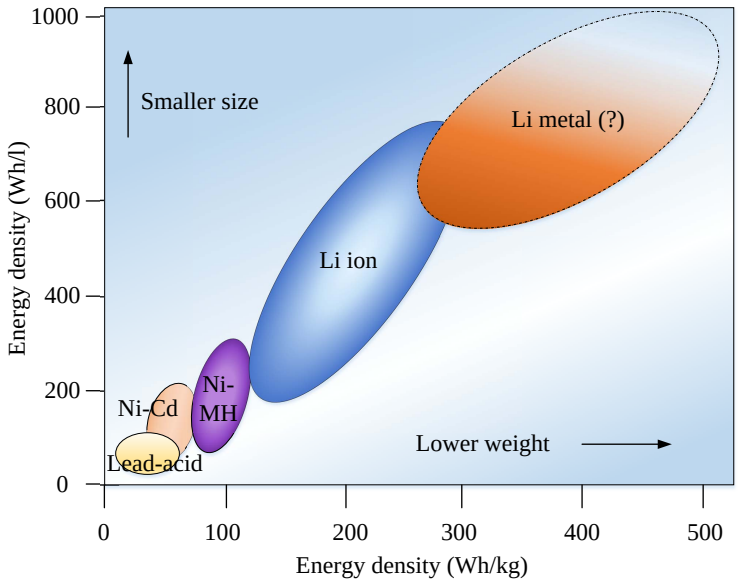

Figure 2.1: Summation of different battery technologies cell energy densities as a function of weight and volume [39, 40].

is often used to prevent short-circuit of the electrode materials. The electrode materials are used as a host material where lithium (Li) is stored in the crystal structure or between layers of the host material. Both electrodes and the separator is drenched with the electrolyte that enables the transport of Li^+ between the electrodes.

In the charged state the NE has a high concentration of Li and a low potential. The PE has a low concentration of Li and a high potential. When connecting the electrodes via an external load, electrons move spontaneously from the NE, increasing its potential, through the load to the PE, decreasing its potential, therefore reducing the driving force, i.e the overall cell voltage. Li^+ are simultaneously transported by the electrolyte from the NE, through the separator, to the PE to conserve charge neutrality (Figure 2.2).

The described processes are those of a discharge. The processes is reversed during charging of the battery [41]. The overall cell reaction during discharge and charge is the sum of the separate electrode reactions [42]:

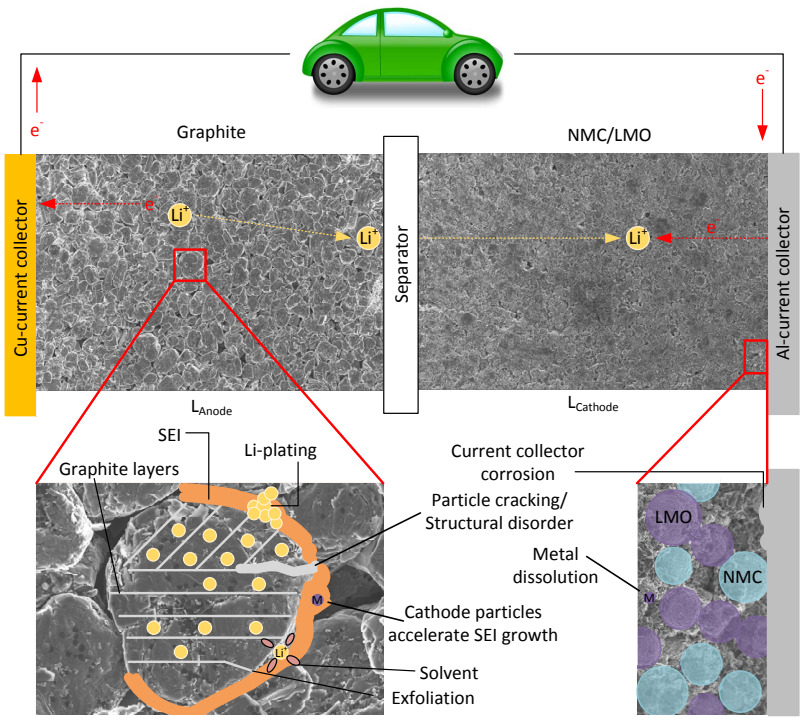

Figure 2.2: Top part illustrates how a LiB works during discharge and the bottom part shows some of the ageing mechanisms that can occur during usage [6].

Overall cell reaction:

$$\mathrm{Li}_x\mathrm{C}_6 + \mathrm{Li}_{1-y}[\mathrm{Ni}_{1/3}\mathrm{Mn}_{1/3}\mathrm{Co}_{1/3}]\mathrm{O}_2 + \mathrm{Li}_{1-z}\mathrm{Mn}_2\mathrm{O}_4$$

$$\overset{discharge}{\underset{charge}{\rightleftharpoons}}$$

$$\mathrm{C}_6 + \mathrm{Li}[\mathrm{Ni}_{1/3}\mathrm{Mn}_{1/3}\mathrm{Co}_{1/3}]\mathrm{O}_2 + \mathrm{LiMn}_2\mathrm{O}_4$$

Graphite: $\mathrm{Li}_x\mathrm{C}_6 \rightleftharpoons x\,\mathrm{Li}^+ + \mathrm{xe}^- + \mathrm{C}_6$

NMC: $\mathrm{Li}_{1-y}[\mathrm{Ni}_{1/3}\mathrm{Mn}_{1/3}\mathrm{Co}_{1/3}]\mathrm{O}_2 + \mathrm{yLi}^+ + \mathrm{ye}^- \rightleftharpoons \mathrm{Li}[\mathrm{Ni}_{1/3}\mathrm{Mn}_{1/3}\mathrm{Co}_{1/3}]\mathrm{O}_2$

LMO: $\mathrm{Li}_{1-z}\mathrm{Mn}_2\mathrm{O}_4 + \mathrm{zLi}^+ + \mathrm{ze}^- \rightleftharpoons \mathrm{LiMn}_2\mathrm{O}_4$

where x=y+z, 0<x<1, 0<y<1 and 0<z<1.

2.1.1 Electrode Materials

There are today several different electrode materials, the usable capacity of some of these are summarised in Figure 2.3. Depending on the application, materials with desired properties are matched. Some examples of the properties of interest are capacity, potential curve, kinetics, lifetime and cost.

Graphite is the most commonly used NE due to its abundance, high electrical conductivity, high capacity, low potential, and low price [43,44]. For high power applications Lithium Titanium Oxide (LTO) is an alternative to graphite due to its safety, fast kinetics, superior thermal stability, high cycle life, and practically no SEI. The lack of an SEI on LTO is due to its high potential that is within the electrolyte stability window (see next section), but a drawback is that this will result in a lower cell voltage and higher cost [44, 45].

The PE materials have lower capacity than graphite, which means that there is a need for more of the PE material to make a balanced cell (Figure 2.3). The cost of the PE material is therefore also an important property. The relative importance of properties is determined by the targeted application.

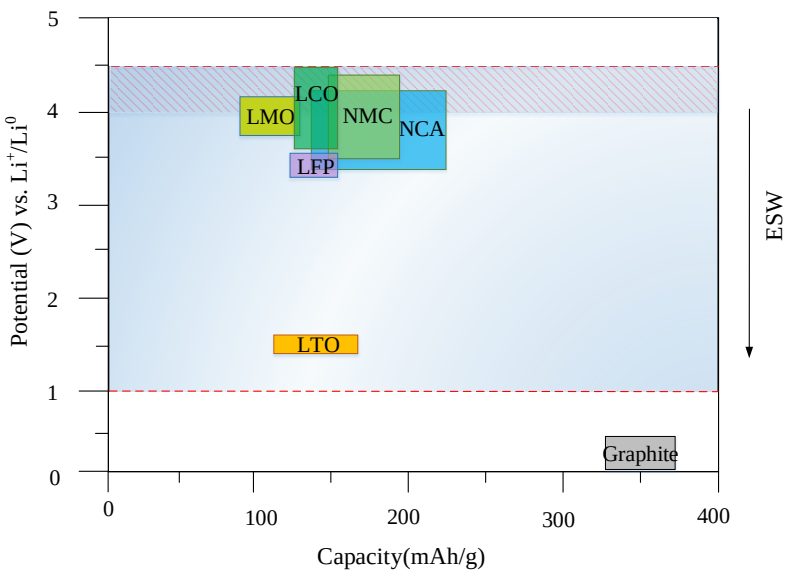

Figure 2.3: Approximate electrode potential vs capacity for various electrode materials [44, 46, 47]. The blue area indicates the ESW for the electrolyte and the dashed area the variation in ESW for different combinations of electrolytes and materials.

2.1.2 Electrolyte

The electrolyte mediates the ion transfer between the two electrodes. The electrode materials decide the energy content, in most cases the electrodes can be designed so that the electrolyte is rate limiting for the mass flow within the battery, i.e it defines how fast the energy can be released. The electrolyte should therefore have high ion conductivity over a wide temperature range and be electrically insulating.

The electrolyte components should also be chemically and electrochemically stable towards the electrodes [48]. In Figure 2.4 a schematic graph of the electrolyte stability window (ESW) for the electrolyte is visualised. The stability window is defined by the lowest unoccupied molecular orbital (LUMO) and the highest occupied molecular orbital (HOMO). If the NE potential, μ_a, is above the LUMO, the electrolyte will be reduced, and if the PE potential, μ_c, is lower than the HOMO it will be oxidised. For thermodynamic stability the electrochemical potentials μ_a and μ_c must be within ESW, constraining the open-circuit voltage (OCV), V_{oc}, of a battery cell to a small interval. Organic liquid electrolytes typically have a HOMO below 4.5 V [48, 49] and a LUMO around 1 V [46].

The potential window of the ESW is highly depending on the electrolyte composition, electrode materials and temperature [48, 49]. As seen in Figure 2.3, the potential for graphite is outside this thermodynamic stability window. The graphite electrode is, instead, kinetically stabilised by a passivisation film, the SEI, formed on the electrode surface by reduced electrolyte components [50]. A similar stabilisation can be inferred on the PE by the formation of a cathode electrolyte interphase (CEI).

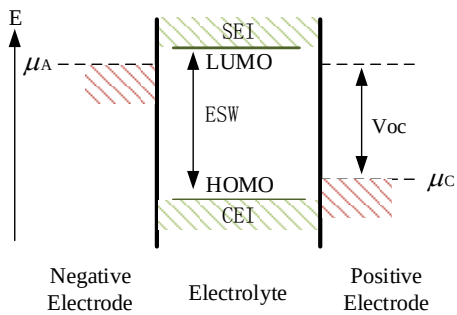

Figure 2.4: Illustration of the thermodynamic electrolyte stability window, ESW. If the electrode electrochemical potentials μ_c<HOMO and μ_a>LUMO the system can be kinetically stabilised by formation of CEI or SEI [46].

The safety aspect is also important and the overall cell should be stable and have a tolerance to electric, mechanical, and thermal abuse, preferably nonflammable and nonexplosive if short-circuited. In addition it should consist of materials that have low cost, are non-toxic, and renewable [46, 48]. To meet these requirements the liquid organic electrolytes, most commonly used in commercial cells, consist of one lithium salt in two or more organic solvents. A number of additives are also added to decrease flammability, hinder side reactions, protect the cell from overcharge, to form stable passivation films etc [50].

2.2 Ageing in Lithium ion Batteries

LiBs degrade with time and usage, they experience power and energy fade associated with impedance rise and capacity loss. The main contribution to capacity loss has been linked to loss of cyclable Li^+ and loss of active electrode material [6]. The loss in power capability originates from increased contact resistance at interfaces between the materials, growth of resistive films on the active materials, loss of active surface areas and impaired mass transport [51].

2.2.1 Ageing Mechanisms

All the components of the battery experience different ageing processes. The current collectors (cc) often experience corrosion while the separator mainly suffers from mechanical damage inflicted by other components or high temperatures. The binder, gluing the active material particles together, and other organic components such as the electrolyte, decomposes by electrochemical and chemical reactions accelerated by high temperatures, high and low electrode potentials. The active electrode materials can experience structural disorder, cracking of particles, surface film formation and some cathode materials experience metal dissolution [52]. Structural changes, corrosion and degradation of the binder can result in loss of contact between the active particles, and between particles and the cc, which leads to impedance increase and loss of capacity [6].

The dominating ageing mechanisms for the type of cell studied in this project will be described in the following sections. The main ageing mechanisms reported in the graphite electrode are SEI formation, loss of active material, and contact loss between active particles and active particle-current collector (Figure 2.2) [6]. The main ageing mechanism reported for LMO is manganese dissolution [4, 53]. For NMC it has been shown to be structural changes to the particle surface introducing stress in the particles leading to

cracking and at high potentials, transition metal (TM) dissolution of manganese and nickel [54, 55].

Solid Electrolyte Interphase

In cells with graphite as NE material the main ageing mechanisms have been proven to be the side reactions taking place on the graphite surface reducing the electrolyte solvents to build an SEI [56].

The decomposition of electrolyte has been shown to start below 0.8 V vs Li/Li^+ [8, 50]. The typical operating potential for graphite is 0.3-0.0 V vs Li/Li^+ [20], and the electrolyte coming into contact with any pure graphite surface will therefore be reduced and form SEI. During the formation of the SEI there is an irreversible loss of Li^+. It is therefore of high importance to build a mechanically stable and flexible SEI that prevents further electrolyte reduction and thereby reduces the growth speed of the SEI. The SEI has to be both electronically insulating to stop further reduction and ionicly conducting to enable Li^+ to pass through during cycling [11]. The properties of the SEI is optimised by adding selected additives to the electrolyte, such as film forming agents, that are reduced before the main components at potentials >1.0 V vs Li/Li^+ [50].

The SEI is dynamically changing during charging and discharging [8]. However, it continuously grows with the number of cycles where the main growth occurs during charging [8], and increase at higher battery SOC and higher temperatures [6, 23].

There have been many different models suggested to describe the complex structure of the SEI [11, 17, 57–61]. For this project, a two layer model is considered. An inorganic matrix, representing the inner SEI layer, and a porous organic layer, representing the outer SEI layer [7, 8, 17, 61].

The inner layer starts to form immediately when the graphite comes in contact with the non-aqueous electrolyte. It is this layer that is vital for the protective behaviour of the SEI [62]. It consist of both soluble and insoluble reduction products of electrolyte components [17], where an ideal inner SEI consists only of insoluble products and has a thickness that is limited by the electron tunnelling range [11].

The outer SEI growth has been proven to follow the parabolic law, $t^{1/2}$, under low load conditions (C/10) [17, 20, 29]. The mechanisms behind the growth of the layer is not yet fully identified. Several different mechanisms have been proposed, diffusion of solvent/salt molecules/anions though nano-sized pores [19, 29], electron tunnelling [63], electron conduction through the SEI [63, 64], diffusion of neutral radicals such as lithium interstitials [65], and properties similar to a solid membrane [62].

The SEI creates an impaired mass transport in the Li^+ flow and thereby increases the charge transfer resistance and total impedance of the NE [6]. This impedance increases with cycle number, charge rate, SOC, and in particular with high temperature. The formation of the SEI is the predominant source for the loss of Li^+ during storage conditions [56].

Transition Metal Dissolution

LMO and NMC are prone to TM dissolution resulting in loss of active material in the PE. The process accelerates at higher voltages and elevated temperatures [4, 53–55]. In LMO the metal dissolution start at voltages higher than 4.0 V [4, 53, 66]. In NMC the dissolution starts at a slightly higher voltage, above 4.2-4.3 V [10, 54].

Several different processes have been suggested to lead to TM dissolution in LMO and NMC; loss of oxygen from the electrode structure, disproportionation reaction, Jahn-Teller distortions in LMO, differences in lattice parameters during charge/discharge, instability in the delithiated structure (loss of MnO) and acid attack from HF or other impurities or products originating from side reactions/oxidation of the electrolyte [4, 53–55, 66].

The oxidation of the electrolyte occurs at the PE and starts at 4.0 V in LMO. The oxidation rate is strongly correlated to the specific electrolyte and increase exponentially with increasing voltage [4].

Structural Changes

Another ageing mechanism include cracking of particles, which can occur in all three materials, but in particular NMC has shown to be at higher risk, where the particles are prone to intergranular cracking [67]. This leads to increased impedance and loss of capacity [54, 67].

Cross-talk Between Electrodes

To study ageing of electrodes separately only gives a part of the answer. When two electrode materials are put together in a cell there will be cross-talk between the electrodes [9, 10]. One of the best known example is Mn dissolution from the PE and migration to the NE where it deposits. Interaction of gaseous products from the PE on the NE has also been reported [10].

Cross-talk has been studied using separated electrodes, where a high impedance rise was seen on the NMC, likely from oxidised species depositing on the PE surface, while in a full cell the same species migrates to and is deposited on the NE, resulting in a small impedance rise on the PE [10, 68].

On the NE, the positive TM-ions, cations such as Mn^{2+}, Ni^{2+} or Co^{2+}, and other oxidised species from the PE, contaminates the NE surface and hinder the intercalation process [69]. The underlying deposition mechanism is not fully understood. The deposited Mn has been found to be in metallic form in some studies [70, 71] and with a valence +2 in others [38, 68, 72]. Zhan et al. [38] proposed a metathesis reaction while a reduction reaction is proposed for metallic Mn [70, 71]. Solchenbach et al. [68] proposed a 5 step reaction scheme, where i) Mn^{2+} is absorbed in the SEI, ii) reduced to metallic Mn, iii) re-oxidised to Mn^{2+}, iv) electrolyte is reduced and finally v) catalytic electrolyte decomposition by Mn^{2+}.

Exactly how contaminants such as Mn^{2+} affects the SEI layer and the mechanisms occurring is still not known, but the TM-ions cause the SEI layer to be less passivating and contributes to a faster growth of the SEI [53, 62] and increased impedance [38, 73].

2.2.2 Characterisation Methods

To study changes in the battery during ageing or to characterise the battery for modelling requires different types of tests. For ageing testing it is important to design a test that enables the study of the changes in performance, a RPT. The test should: affect the cell as little as possible, be fairly quick, include the measurements required for a chosen analysis, and not be performed too often.

For the extraction of parameters for models, more time consuming tests can be used. It could be capacity measurements at different C-rates and temperatures, and various pulse tests with different lengths and C-rates. The test and analysis methods used in this thesis are Galvanostatic Intermittent Titration Technique (GITT), Incremental Capacity Analysis (ICA), and Electrode Slippage and Material Loss Estimation (ESMLE).

Reference Performance Test

The RPT is often limited to measure the capacity and impedance. The capacity is measured at one C-rate (often$\leq$1C) and the impedance through a pulse test or Electrochemical Impedance Spectroscopy (EIS). The results from the test is used to track changes in performance during the lifetime of the battery or compare the performance of different battery types. There is a large variation in how these tests are constructed based on the analysis desired and the type of cell. The different performance tests used in this project are described in section 3.3.

The cell resistance during the ageing tests were recorded by the RPT (see Section 3.3.1). The resistance is calculated from the voltage response to a

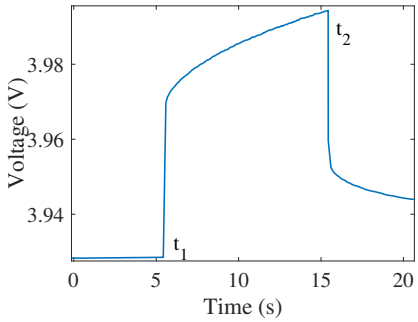

Figure 2.5: Voltage response to a 10s 1C current pulse showing t_1 and t_2 used for the resistance calculations.

current pulse;

$$R_{pulse} = \frac{u(t_1) - u(t_2)}{i(t_2) - i(t_1)} \tag{2.1}$$

where $u(t_1)$ is the voltage before the pulse and $u(t_2)$ the voltage at the end of the pulse, $i(t_2)$ and $i(t_1)$ are the currents at the respective points (Figure 2.5). This method does not take into account the change in OCV during the pulse. However, in an ageing test it is the change in resistance over time that is of interest rather than the absolute value.

Galvanostatic Intermittent Titration Technique

GITT is a pulsed current test method to map the OCV as a function of Ah or SOC. The pulse current is often low, in the order of C/10. The cell is charged in steps of 1-2% SOC from 0-100% SOC. Between each pulse the cell is relaxed for at least 1h, often longer. When 100% SOC is reached, the discharge is performed in the same steps 100-0% SOC.

Incremental Capacity Analysis

ICA is a method to evaluate changes in the electrochemical properties of the cell and is performed by calculating the change in capacity over the change in voltage from a slow charge and discharge cycle. The relative ageing of the electrodes can be identified in this way. By studying the intensity and position of the peaks, capacity loss from Li-loss or active material can be detected together with the effects of polarisation [26, 74]. The charge and discharge profiles are used to identify the phase equilibrium of the active materials, seen as plateaus in the voltage profiles and peaks in the ICA. Hence, the peaks correspond to phase changes in the intercalation material where two

or more phases with different lithium concentrations coexist with the same chemical potential [15, 75]. The differential capacity over the differential voltage ($\Delta Q/\Delta V$) is analysed as a function of the cell potential.

The result from the ICA depend on the current used for the charge and discharge cycle. A slow rate of C/10 or lower is desired to limit the effects of polarisation. Currents above this can still be used to provide a crude image of the processes occurring. However, the results should be treated with caution since the polarisation contribution can conceal processes and makes the analysis more difficult.

Electrode Slippage and Material Loss

When assembling a cell, the electrode materials are balanced in relation to their respective capacities. The full electrode capacity is not utilised in the normal operation of the cell, instead a usage window, typically a defined voltage interval, is determined to limit the amount of side reactions taking place during usage, to reduce ageing and prolong the life of the battery. The ageing processes occurring can be established by quantifying the electrode slippage and material loss at each electrode.

If electrolyte is reduced at the NE, the requirement for charge neutrality implies that the electrode must either receive an electron from the PE or release a Li^+. Receiving an electron from the PE means that the PE is forced to release a Li^+. Electrolyte oxidation at the PE leads to the opposite where the PE gains a negative charge that needs to be compensated for. The reduction or oxidation will cause a change of the lithium concentration in one of the electrodes and change the potential in that electrode, i.e cause a slip in the balance between the electrodes.

A schematic representation of the respective electrode potentials for a fresh and aged cell can be seen in Figure 2.6. The outermost vertical grey lines indicate the potentials of the separate electrodes in a charged and discharged cell. In the example case the NE have slipped to the left (reduction of electrolyte) and the PE have lost active material. Even if the PE have lost active material it is still only partly utilised. The limiting electrode is in this case the NE, being fully delithiated during discharge.

Using this method, the ageing in a LiB can be studied by quantifying the electrode slippage and material loss at each electrode. In this way also the ageing of the non-limiting electrode is observable. The analysis requires slow current measurements of half cells with electrodes from a fresh cell and full cell measurements of the cell to be analysed and using the same current rate. The model then matches the two half cell potential curves through a optimisation process calculating the material loss and slippage in order to get a good agreement to the measured full cell ICA.

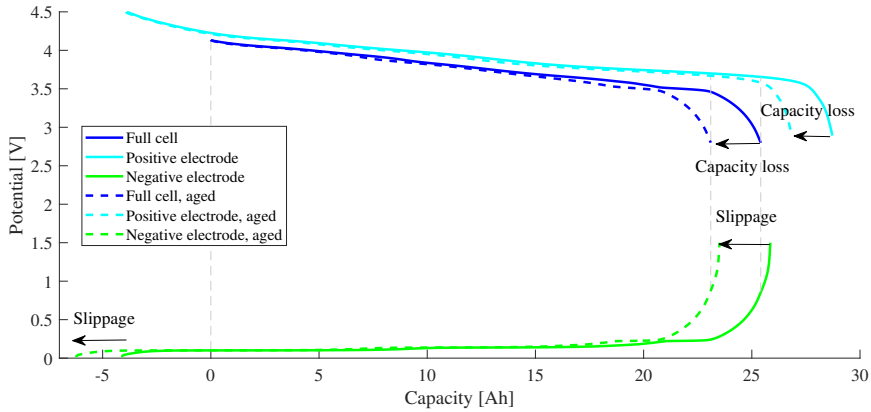

Figure 2.6: Schematic representation of the respective electrode potentials of a fresh cell and an aged cell, where the PE has lost capacity and the NE has slipped due to side reactions, leading to reduced cell capacity.

Post-Mortem Analysis

This is a destructive analysis method where the battery cell is opened and disassembled, so that the separate components can be evaluated by visual inspection and through selected material characterisation methods. The state of the cell, the disassembly and characterisation environments have to be well-defined to be able to perform a reliable comparison between aged cells.

For lab scale cells and cells with low capacities (mAh) a predetermined SOC level within the normal operating window is used when disassembling the cell. For commercial cells, with several Ah capacity, the cell has to be in the discharged state before the disassembly, commonly 0% SOC, for safety reasons. Discharging the cells to far however, may introduce unwanted material changes which do not occur when the cell is operated in its normal operating widow. The dissasembly is conducted in a glovebox with highly pure Argon atmosphere, with only ppm levels of H_2O and O_2, to avoid contamination or reactions [76].

The analysis of the different components varies, common methods include X-ray diffraction (XRD), Energy-dispersive X-ray spectroscopy (EDS), scanning electron microscopy (SEM), X-ray photoelectron spectroscopy (XPS), inductively coupled plasma-optical emission spectrometry (ICP-OES), and Gas chromatography–Mass spectrometry (GC-MS) to mention a few [77, 78].

SEM is used for surface morphology investigations, while XPS, with different excitation photon energies, is used to analyse the compositional changes

in the electrode surface layers at different depths. For electrochemical investigations it is common to use harvested electrode materials assembled in half cells or symmetric cells. This is done to distinguish which electrode is limiting the cell capacity and power, and undergoing most degradation [78]. GC-MS is used to investigate changes and composition in the electrolyte [77].

Chapter 3

Experimental Setup

In this chapter the test object specifications, together with some of the characterisation tests on half and full cells, are presented. The test procedure and equipment used for the lifetime testing, cycling and calendar ageing, are shortly described.

3.1 Test Object

The test object for the work of this thesis is a commercial 26 Ah (96 Wh) pouch cell (Figure 3.1a). The cell (232x164x8 mm, 0.55 kg) has an energy density of 170 Wh/kg or 330 Wh/l. It is made up of 13 stacked bicells, 7 NE/PE/NE and 6 PE/NE/PE, resulting in a total of 38 interconnected electrochemical cells. A simplified schematics of the stacked and folded cell construction is shown in Figure 3.1b.

The cell is designed for use in the voltage window 2.8-4.15 V, corresponding to 0 and 100% SOC respectively. The current needed to discharge the cell in 1 h is 26 A, 1C. The NE is surface treated natural graphite and the PE is a mixture of spinel LMO (30 wt%) and NMC (70 wt%). The separator is made of polypropylene and the electrolyte is composed of the solvents Ethylene Carbonate (EC)/Dimethyl Carbonate (DMC)/Ethyl Methyl Carbonate (EMC) and the salt $LiPF_6$.

3.1.1 Electrode Materials

For the characterisation of the cell, one commercial uncycled cell was opened and disassembled. Part of the electrode materials was harvested to build several lab scale pouch half cells vs lithium foil. Physical properties of the

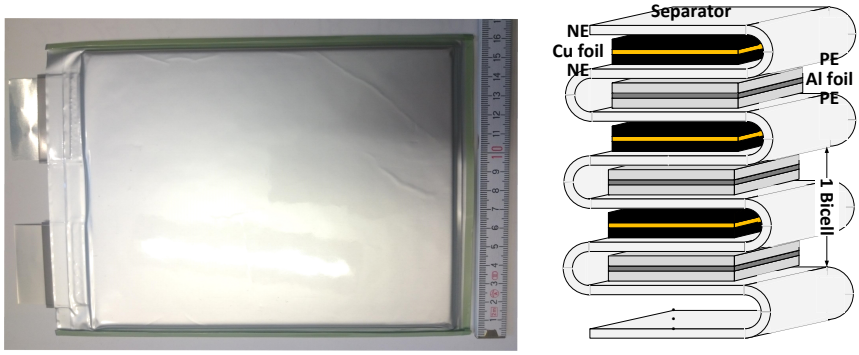

(a) (b)

Figure 3.1: (a) The test cell and (b) a simplified picture of its design. The internal structure of a single cell is composed of multiple electrodes stacked with the separator in a zigzag pattern. One bicell consists of three electrode sheets sandwiched with the configuration NE/PE/NE or PE/NE/PE.

electrodes were extracted by galvanostatic, SEM, EDS and XPS experiments. This was performed at the Ångström Laboratory at UU by Erik Björklund, who also built and performed all the measurements on the half cells. The results from the different measurements are shown in Table 3.1. The amount of additives in the electrodes were not measured. Based on the approximate amount of binder for the NE, that was given from the manufacturer, and XPS measurement the conductive additives in the NE could be calculated. For the PE no values for the binder or additives were given and only % values based on the intensity of the XPS measurement are presented.

Table 3.1: Measured properties for the studied cell.

	PE	NE
Thickness, L [μm]	74	64.5
Thickness current collector, L_{cc} [μm]	21	12
Particle size, D_{50} [μm]	10.9	14.7
Capacity [mAh/cm^2]	2.6	2.8
Density [g/cm^3]	2.93	1.60
Conductive carbon	18% of additives	0.46wt%
Binder	82% of additives	2wt%

Half Cell ICA

An ICA was conducted on the potential curves from the lab scale pouch half cells, cycled at a rate of C/28. The peaks in Figure 3.2 correspond to phase transitions in the respective electrode materials, also seen as plateaus in the potential curves (Figure 5.1).

The NE shows three clear peaks and two diffuse (Figure 3.2a). The Li^+ intercalation occurs step-wise, in a so called stage formation. Li^+ is intercalated between the graphite layers separated by a number of empty layers. The step index, s, identifies the number of layers between occupied layers. It is energetically favourable to completely fill one layer before a new layer starts to be filled.

The phase at the beginning of the lithiation (at high voltage) is known as stage V, $0 < x \leq 0.166$ Li^+ intercalated in LiC (Li_xC_6). Peak 5 represents the phase transition to stage IV. The small Peak 4 represents the change from stage IV to III ($0.166 < x \leq 0.22$). Peak 3 ($0.22 < x \leq 0.34$) represents the transition from stage III to II-L and Peak 2 from stage II-L to II, $0.34 < x \leq 0.5$. The difference between stage II L and II is due to different Li^+ packing densities. Finally Peak 1 is due to the transition to stage I ($0.5 < x \leq 1$) [15, 42, 79].

The ICA for the PE includes three distinct peaks, Figure 3.2b. Peak 1 is the contribution from NMC [80–82]. The hexagonal layered structure is not changed during charge and discharge but a phase transformation mechanism linked to changes in the electronic state (es) occurs (hybridisation of Co and O orbitals) [55].

Peak 2 and 3 is from lithiating LMO [42, 82]. The separation into two peaks, 4 and 4.1 V, corresponds to a two-stage phase transition of one cubic spinel structure to another, a redistribution of Li^+ in the material at $Li_{0.5}Mn_2O_4$. For higher Li^+ content the cubic lattice continuously expands resulting in an additional peak [83, 84].

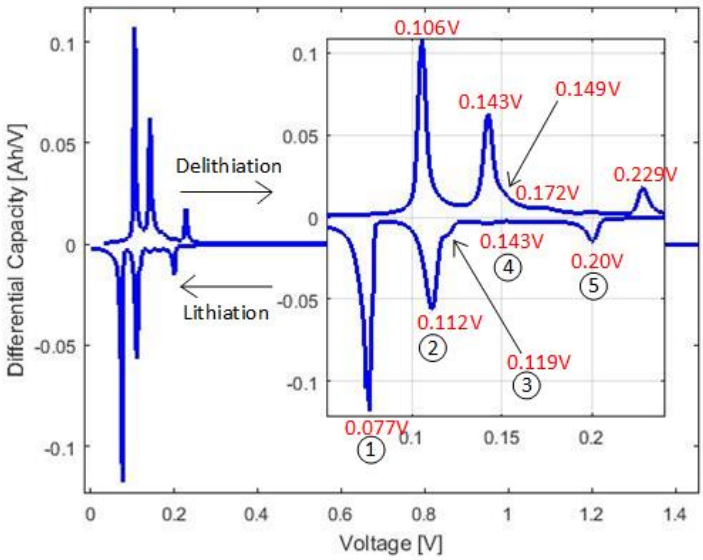

(a)

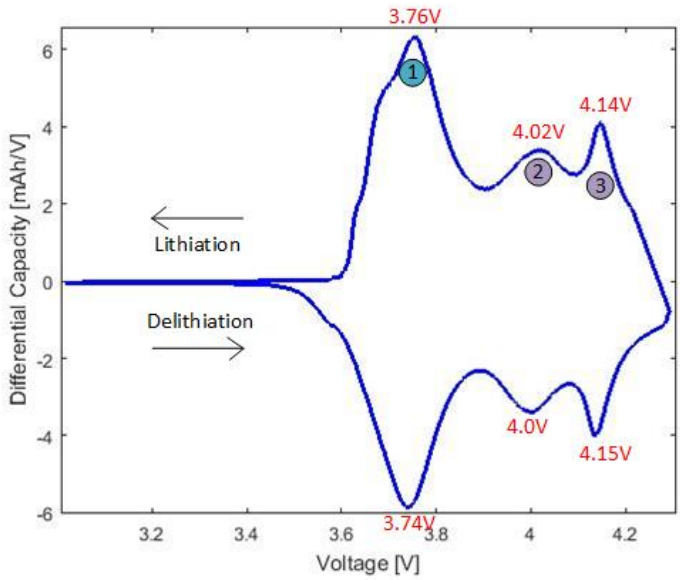

(b)

Figure 3.2: ICA from C/28 constant current charge and discharge from lab scale cells made from material harvested from a commercial battery cell. (a) for the mixed PE material, LMO and NMC, and (b) for natural graphite vs. Li-metal.

3.1.2 Full Cell Characterisation

OCV and Hysteresis

When measuring the OCV for a cell or material two different methods exist; creating a pseudo OCV curve from a slow charge and discharge cycle or the more accurate GITT measurement. In both methods the OCV is calculated as the average of the charge and discharge potential at the specific cell capacity. The GITT measurement was used to calculate the full cell OCV (Figure 3.3).

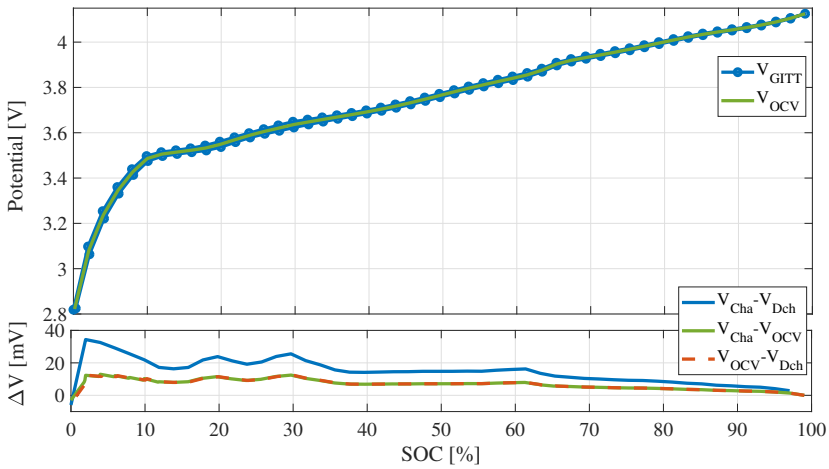

Figure 3.3: GITT result for the commercial cell and the potential difference at different SOC levels.

The results showed a clear offset between the OCV received from the charge pulses compared to the discharge pulses, indicating that the materials have a hysteresis effect. For several different LiBs there have been reports of a hysteresis between the charge and discharge OCV [85–88].

The cause for the hysteresis is reported to arise in a many particle system from that the particles reach different equilibrium states [85, 86, 88]. Charging will promote the higher equilibrium state and the discharging the lower equilibrium state, giving rise to a small but noticeable hysteresis. The hysteresis dependency with SOC and vs the OCV is shown in the lower section of Figure 3.3.

The hysteresis has not been accounted for in the model. This introduces an error that is as largest at low SOC and low C-rates where the hysteresis contribution, around 10 mV, is more notable. For the ageing model, the lowest current used is 1C and only a small error is expected.

Commercial Cell ICA

The full cell ICA is a combination of both electrode materials phase transitions. An ICA was performed for the commercial cell for a C/10 charge and discharge cycle (Figure 3.4). Each peak correspond to a phase transition for one or both of the electrodes, the numbers indicate the materials related to each peak.

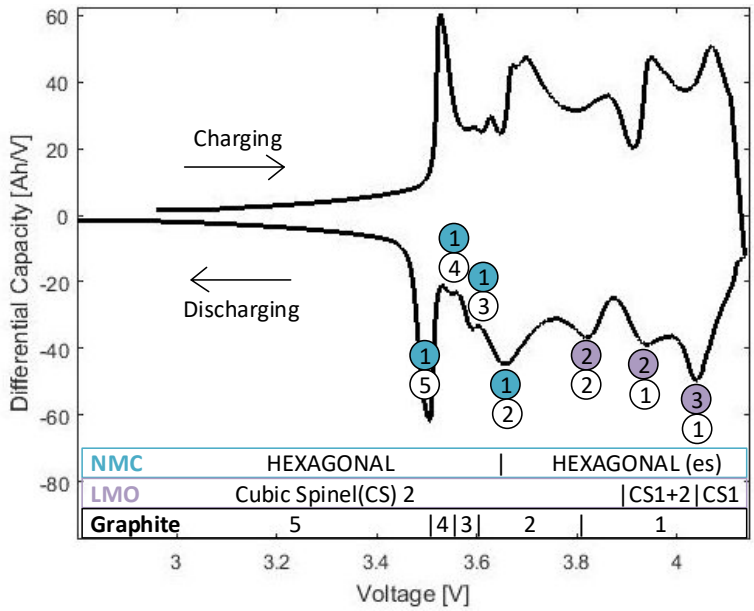

Figure 3.4: ICA for the fresh battery cell with the different materials stages indicated [42, 80, 83].

Cell Resistance

The resistance dependence on temperature and current was investigated by 10 s pulses and calculated using (2.1). Figure 3.5a shows the discharge resistance as a function of SOC measured at 26°C and 47°C. The resistance decreases with increased temperature, the 26°C case gives rise to a 30% resistance increase compared to the 47°C case.

The resistance dependence on the current drawn from the battery was investigated with currents from 0.5 A to 50 A, Figure 3.5b. As the current becomes lower, the resistance exponentially increases. This is manly related to the activation polarisation, since both the ohmic and concentration polarisations are low at low currents.

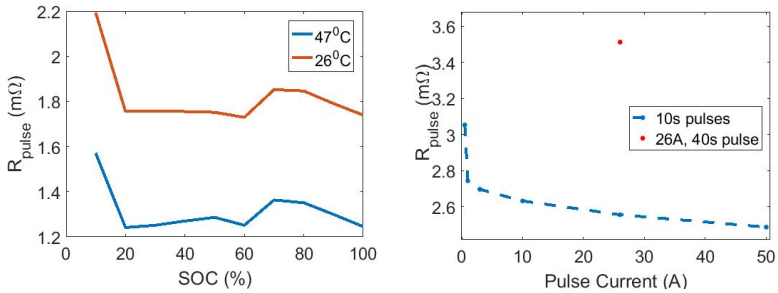

(a) (b)

Figure 3.5: Measured cell resistance dependence on current, SOC and temperature. (a) 10 s 5C pulse discharge resistance as a function of SOC and T. (b) 10 s pulse resistance at different current levels at 26°C, and the resistance for a 40 s pulse at 1C.

The resistance is also increasing with the length of the pulse (Figure 2.5). The red dot is a 26 A 40 s pulse measured in the RPT for the same cell performed before the tests with 10 s pulses. The longer time a current pulse is drawn from the cell, the higher the resistance will be, due to increase in the concentration polarisation.

3.2 Lifetime Tests

To study the ageing, calendar and cycling ageing tests were performed. Cycling tests were made for different C-rates and SOC intervals. The ageing was investigated at four different temperatures by cycling in climate chambers set to 25, 35, 40, and 45°C.

The lifetime tests were performed in conditions similar to those in a battery pack in a vehicle. The cell was placed in a specially designed holder, Figure 3.6, with limited space to expand. The thick aluminium plate also worked as a cooling system with forced airflow on one side.

The voltage was measured over the tabs via two bent copper plates pressed together with the tabs by two brass bricks, each held in place with two screws. The current cables were connected to the larger brass blocks (Figure 3.6).

A temperature sensor was placed between the tabs on the cell-body next to the gas-pocket, to track temperature and ensure safety at all times. The cell temperature rose during cycling and were a few degrees higher than the chamber temperature due to the heat produced by the cell.

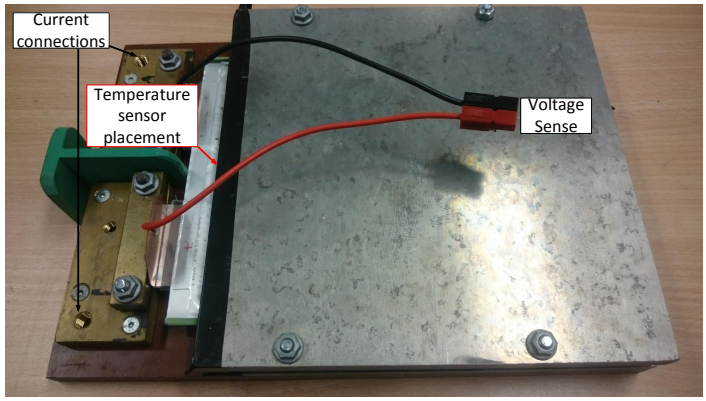

Figure 3.6: Test jig for imitating conditions in a cooled battery pack.

3.2.1 Test Equipment

All tests were performed in temperature controlled chambers, Vötsch VT3 7034, VT3 4060 and Climate Temperature System, T-40/350. The chamber temperatures were set to 25, 35, 40 or 45°C. The cell cycling equipment used in the project were the following: Maccor Series 4000, PEC SBT0550 and Digatron MCT 100-05-8.

3.2.2 Calendar Tests

The calendar ageing was performed by storing the cell at a specified temperature and SOC. Every 30^{th} day an RPT was performed at 25°C in a dedicated chamber to assess the cell capacity, resistance and self discharge. The cell was then returned to the climate chamber for storage and the process repeated. A total of 18 cells were calender aged under nine unique conditions (one replica per test) at 25, 35 or 45°C and at either 15, 75 or 90% SOC.

3.2.3 Lifetime Cycling Tests

When performing cycling ageing it is important to have a good control system to ensure that the cycles reflect the intended test. In addition it is also important to ensure safe test conditions. The cycling program should stop the testing before something goes wrong. Apart from health risks, months of testing and expensive equipment are at risk. Each test program therefore includes global limits for temperature, voltage and current so that the test is terminated and damages avoided in case of a malfunction.

3.2.4 Test Protocols and Load Cycles

The cycling ageing tests were performed for different load cycles, temperatures and DODs. The full test matrix can be seen in Table 3.2. The DOD used were 90%, 80%, 60% and 10%. At intervals ≥60%, and for three tests at 10% DOD, an upper voltage limit using constant voltage (CV) charging combined with Ah-counting was used to maintain the targeted SOC interval (Figure 3.7a). In the 10% SOC intervals, Ah-counting was used together with a control method developed within the project [89], briefly described in Section 3.2.5 (Figure 3.7c, 3.7d and 3.7e).

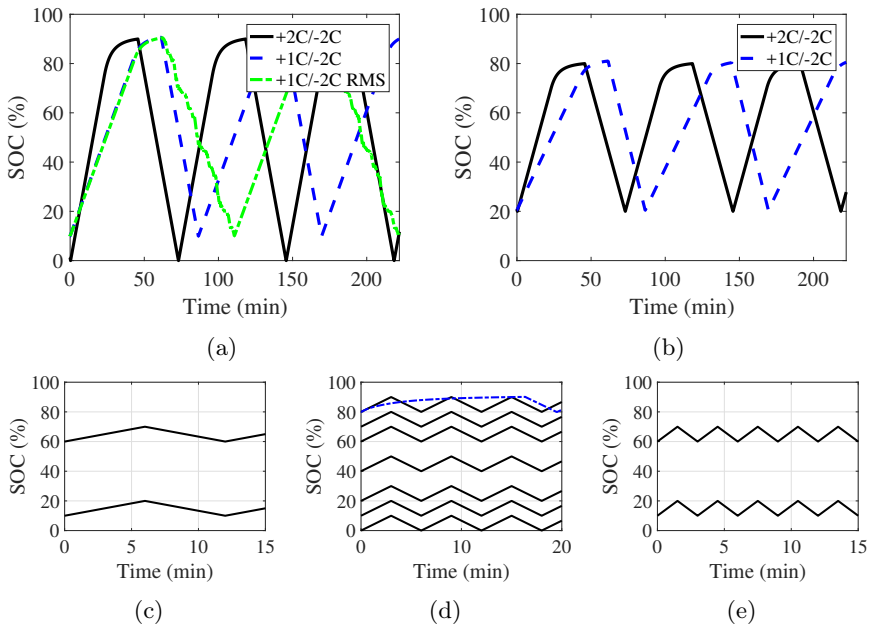

Figure 3.7: Load cycles used for the lifetime cycling at (a) > 60% DOD, 0-90% +2C/-2C black solid line, 10-90% +1C/-2C blue dashed line and green dashed dotted drive cycle with 1C charge current and 2C RMS discharge current, (b) 60% DOD (20-80% SOC), symmetric, +2C/-2C black solid line, and asymmetric, +1C/-2C blue dashed line, and 10% DOD for symmetric +XC/-XC in different SOC intervals in (c) 1C, (d) 2C with blue dashed line representing CC-CV at 80-90% SOC, and (e) 4C.

Table 3.2: The test matrix for the lifetime cycling and calendar ageing. Designation I and II indicates one or two tested cells and the superscripts refers to cells subjected to PM analysis.

Calendar ageing	T=25°C			T=35°C			T=45°C		
SOC[%]	15	75	90	15	75	90	15	75	90
	II	II	II	II	II	II	II	II	II

Symmetric	T=25°C			T=35°C			T=40-45°C		
cycles, SOC [%]	±1C	±2C	±4C	±1C	±2C	±4C	±1C	±2C	±4C
0-10		II			I			II	
10-20	I	I	I	I	I	II	I	I^{PM}I	II^{PM}
20-30		I						II	I
30-40									
40-50		I			I			I	
50-60									
60-70	I	I	II	I^{PM}	I	I^{PM}I	I	I^{PM}I	I
70-80		I						II	
80-90		I						I	
80-90 CC-CV@4.06V		I						I	
80-90 CC-CV@4.15V		I							
0-30					I				
0-90		I^{PM}			I			I^{PM}	

						T=40°C			
						±1C	±2C	±3C	±4C
20-80						I			
20-80							I		
20-80								I	
20-80			I						I

Asymmetric cycles									
+C-rate, SOC [%]						-1C	-2C	-3C	-4C
+1C, 10-90		I					I		
+1C -Hyzem, 10-90		I^{PM}					I		
+1C, 20-80							I		
+1C, 20-80								I	
+3C, 20-80						I			

Current levels from 1-4C were tested, where 4C (full charge of discharge in 15 min) constant current (CC) is considered to be very high for the tested cell. Tests were also performed to study the effects of a dynamic current load compared to a CC load. A so-called drive cycle, Hyzem Rural (Figure 3.8), with 2C Root Mean Square (RMS) current was included to be compared with the CC 2C cycle at 80% DOD, for this purpose.

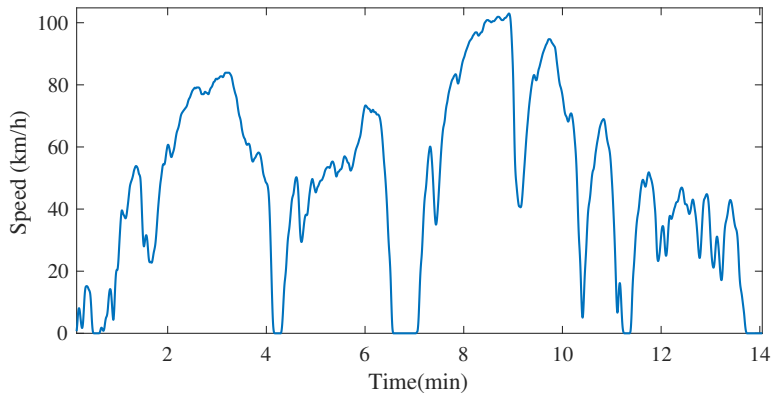

(a)

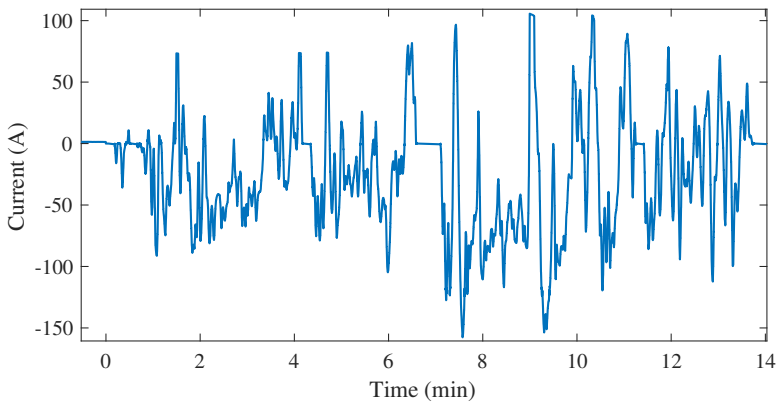

(b)

Figure 3.8: The drive cycle Hyzem Rural (a) vehicle speed and corresponding (b) current profile [90].

3.2.5 Control Method for 10% SOC Intervals

A control method to ensure the SOC interval during cycling in 10% DOD with CC was developed and presented in [89]. The method uses voltage peak (and minimum) values together with Ah-counting during each cycle.

The procedure first discharges the cell to the OCV value for the upper SOC level. In the initiation of the cycling, a control cycle was introduced with CC discharge and charge using Ah-counting, where the end voltage values were stored in two control variables. After each charge and discharge the end voltage value was compared to the voltage value from the control cycle according to

$$\Delta V = |V_{upper/lower,1} - V_{upper/lower,n}| < V_{limit}. \tag{3.1}$$

If ΔV is within a predetermined limit value, V_{limit}, the cycling proceeds. If not, a correction cycle of CC-CV is performed to the OCV value for the upper SOC level. The next coming cycle is then the new control cycle.

V_{limit} was adjusted with respect to C-rate, SOC and resistance to ensure a fault tolerance of max 1% SOC. In the low SOC levels, a higher value of V_{limit} was allowed due to the shape of the OCV and higher resistance, according to

$$10 \text{ mV} < V_{limit} < 100 \text{ mV}$$

As the resistance increased during ageing, the limit was adjusted accordingly. At 0% SOC, a constant voltage limit of 2.8 V was used [89].

3.3 Performance Tests

Capacity and current pulse tests were performed to track the capacity and resistance changes of the cell during the ageing process. The performance tests were always performed at the same temperature, 25°C. Initially these tests were performed approximately every 100 FCE, but less frequently after 800 FCE, approximately every 200-1000 FCE. The periodicity of these tests were adapted for each load profile.

3.3.1 RPT

The RPT used, Figure 3.9a, has an activation cycle before it measures the 1C discharge capacity. Next the discharge and charge resistances for two different current pulses, 5C for 10 s and 1C for 40 s in 10% steps over the entire SOC window, are conducted and the voltage response is measured. From these tests, the changes in capacity and resistance as a function of

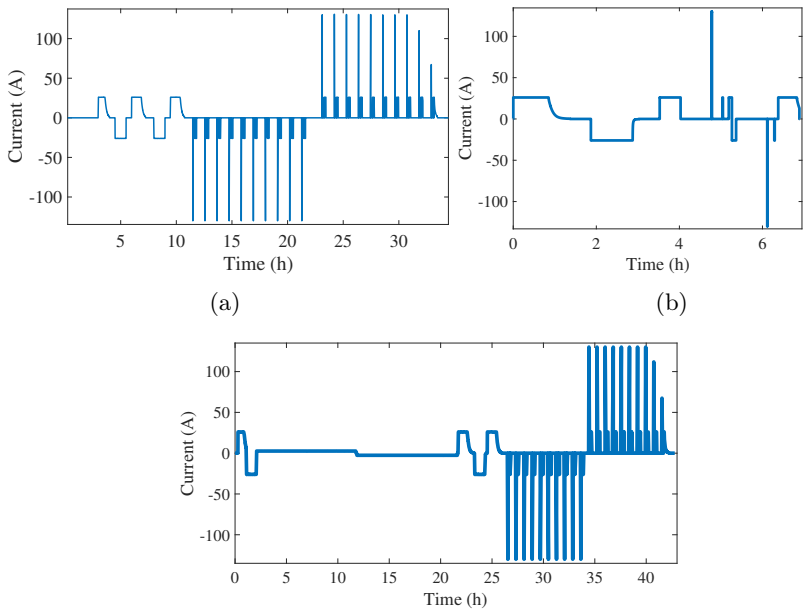

Figure 3.9: (a) RPT for the characterisation of the cell capacity and resistance, (b) Simple RPT for improved continuity in the cycling, and (c) extended RPT including an C/10 cycle.

number of cycles or test time can be studied, linking different load patterns to ageing.

For one cell the RPT was expanded, a C/10 charge and discharge cycle was added before the 1C capacity measure cycle, see Figure 3.9c. For this cell, additional ageing investigations were possible, for instance an ICA could be performed at each RPT.

3.3.2 Capacity Test

In periods and test regimes where the cell was expected to change performance rapidly over a number of cycles, a capacity test was conducted in between the scheduled RPT's. This was done in order to assure that the test proceeded in the targeted SOC interval. The capacity test was performed in 25°C and consisted of the two initial full cycles of the RPT.

3.3.3 Simplified RPT

A simplified RPT was developed for test regimes less detrimental to the cell. The simplified RPT, Figure 3.9b, consists of one full cycle measuring the capacity and two charge and discharge pulses of 10 s 2C and 40 s 1C at 50% SOC with the purpose of tracking the resistance. It was performed at the cycling temperature and incorporated in the cycling protocol. This improved the continuity of the cycling, save time, and introduced less handling of the cells. Using the simplified RPT also reduced the possible ageing contribution from the RPT.

3.3.4 Resistance Characterisation

The cell resistance is complex and highly depending on SOC, current, temperature, pulse duration and frequency. In ageing tests, several different resistance measuring methods can be used to map the ageing, in this project pulse resistance measurements were chosen. Two different pulses were used; 5C for 10 s and 1C for 40 s. The resistance was calculated as described in (2.1).

Chapter 4

Physics-Based Battery Model

In this chapter the physics-based model used in this thesis is presented. It is based on that of Newman and Tiedemann [12] and the continuation of their work by [13, 16, 18–20, 28, 31, 32, 61, 91, 92].

The model consists of a 1D cross-section of an electrochemical cell including the cc, active materials, and separator. For the transport of Li in the active material particles, an additional pseudo 1D is included. It is this additional pseudo-dimension that inspired the name P2D. The model is built in the COMSOL Multiphysics 5.4 Mathematics user interface and uses the Finite Element Method (FEM) numerical solver and Backward Differentiation Formulas (BDF) method to solve the coupled Partial Differential Equations (PDEs).

For a battery with a graphite NE, the main ageing mechanism is the growth of the SEI layer, due to reduction of the solvent on the surface of the graphite particles [6]. For the PE materials, LMO and NMC, Mn dissolution has proven to be the main contribution to capacity loss [4, 53, 54]. The dissolution of Mn-ions has an additional ageing contribution through diffusion to the graphite where the Mn^{2+} deposits in the SEI and causes a resistance increase [9, 10]. In the developed model, the SEI growth, effect of Mn dissolution, and the coupling of Mn^{2+} in the SEI, are simulated.

4.1 Battery Model

The performance battery model and the governing equations for each component in the electrochemical cell is described in the following sections. The

LiB used for this study is presented in Section 3.1 and the parameterisation of the key parameters for the model can be found in Chapter 5. Some of the most important parameters used in the model are given in Table 5.3, 5.4 and 5.5.

4.1.1 Mass Transport in the Electrolyte

In the simulated system the electrolyte is assumed to be a concentrated binary electrolyte, consisting of a lithium salt dissolved in one solvent species. Letting + and − denote the ionic species, Li^+ and PF_6^-, the Maxwell-Stefan equation for the binary electrolyte is used to account for the friction interaction between the species,

$$c_+ \frac{\partial \mu_+}{\partial x} = \sum_- \frac{RTc_+c_-}{c_T D_{+-}^{eff}} (\mathbf{v}_- - \mathbf{v}_+) \tag{4.1}$$

where c_T is the sum of the concentrations of all species, $\mathbf{v}$ is the ions velocity, T the temperature, and R the gas constant. The effective diffusion coefficient, D_{+-}^{eff}, is calculated from the Maxwell-Stefan diffusivity of the pure electrolyte

$$D_{+-}^{eff} = D_{+-}\epsilon_l^{\beta} \tag{4.2}$$

where ϵ_l is the electrolyte volume fraction and β the Bruggeman coefficient [92]. All the effective parameters used in the porous structures in this model use this correlation. From now on D will be used for the effective diffusion coefficient if nothing else is stated.

Mass transport of ionic species in the electrolyte takes place by diffusion, migration and convection. Diffusion is driven by the gradient of chemical potential, the concentration gradient. Migration is driven by the gradient of electric potential and convection by macroscopic streams in the fluid. The total molar flux of a species, N_T, passed over an arbitrary unit area, can be expressed as the sum of the flux contributions from migration (N_m), diffusion (N_d) and convection (N_c)

$$N_T = N_m + N_d + N_c \tag{4.3}$$

since they are considered independent of each other.

In the immediate vicinity of the electrode there is no convection due to friction forces at the material surface. In this area diffusion is the dominant transport mechanism and it is therefore known as the diffusion layer. At increased distance from the electrode there is no concentration gradient and therefore no diffusion, here convection becomes more important. Mass transport by migration takes place in both of these areas [93].

For the concentrated two component electrolyte, solvent and salt, the flux for the positive ion will be

$$N_+ = -\frac{z_+ F}{RT}\frac{c_T c_+}{c_-}D_+\nabla\phi + \frac{c_T c_+}{c_-}D_+\nabla \ln a_+ + c_+ v_- \tag{4.4}$$

where z_+ is the ionic charge of Li^+, F Faraday's constant, $c_{+/-}$ the concentration of Li^+/PF_6^-, ϕ is the potential, D_+ the diffusion coefficient for Li^+ and v_- the velocity of PF_6^-. a_+ is the relative activity ($\nabla\mu_+ = RT\nabla \ln a_+$) [93] and c_T, the total electrolyte concentration calculated from the salt concentration, $c_l = c_{+/-}$, and solvent concentration, c_{solv}, assuming electroneutrality gives

$$c_T = 2c_l + c_{solv} \tag{4.5}$$

The solvent concentration is calculated from the partial molar volume V_m of the salt and solvent

$$c_{solv} = \frac{1 - V_m^l}{V_m^{solv}} \tag{4.6}$$

To simulate the behaviour of an electrochemical system it is often necessary to include one or more of the conservation equations for; mass, energy and momentum. The conservation of mass of species i in a volume element with time t is formulated as

$$\frac{dc_i}{dt} = -\nabla \cdot N_T + \sum_{reactions} \nu_{i,reactions} = -\nabla \cdot N_T + R_{reac} \tag{4.7}$$

where ν_i is moles of species i produced or consumed by reactions [93].

Combining (4.4) and (4.7) while taking into account the porosity, the material balance for the salt becomes

$$\epsilon_l \frac{\partial c_l}{\partial t} = \nabla\left[(1 - c_l V_m^l)\left(\left(1 + \frac{\partial \ln f_\pm}{\partial \ln c_l}\right)\frac{c_T}{c_{solv}}\epsilon_l^\beta D_l \nabla c_l + \frac{i_l(1 - t_+)}{F}\right)\right] + R_{reac} \tag{4.8}$$

where the electrolyte current density is expressed by

$$i_l = \kappa_{l,eff}\left(-\nabla\phi_l + \frac{2RT}{c_l F}\left(1 + \frac{\partial \ln f_\pm}{\partial \ln c_l}\right)(1 - t_+)\nabla c_l\right) \tag{4.9}$$

where $f_\pm$ is the salt mean molar activity coefficient, t_+ is the transport number and, $\kappa_{l,eff}$ the electrolyte conductivity [91, 92].

4.1.2 Potential and Current Coupling

The potential in the cc and the porous electrode materials are calculated by Ohms law from the applied current density

$$i_s = -\sigma_s \nabla \phi_s \tag{4.10}$$

where σ is the conductivity. In the porous materials, as for the diffusion, the effective conductivity

$$\sigma^{eff} = \epsilon^{\beta_s}\sigma \tag{4.11}$$

is used to account for the longer transport distance in the porous structure. The copper cc, on the NE side, is connected to ground and the aluminium cc, on the PE side, is connected to the current feed:

$$\phi_s = 0, \quad x = 0 \tag{4.12}$$

$$-\mathbf{n} \cdot i_s = i_{applied}(t), \quad x = L_{neg,cc} + L_{neg} + L_{sep} + L_{pos} + L_{pos,cc} \tag{4.13}$$

To couple the active material and electrolyte, a balance over the volumetric current is used

$$\nabla \cdot i_l = i_{v,tot} = \sum_m i_{v,m}(+i_{v,dl} + i_{v,side}) \tag{4.14}$$

$$\nabla \cdot i_s = -i_{v,tot} \tag{4.15}$$

The volumetric current in each mesh node, $i_{v,m}$, is the sum of the Faradaic current density from the electrochemical reactions (i_F) and the side reaction taking place ($i_{F,side}$), and the charging of double layers on the surface of the active material particles (i_{dl}) forming the expression

$$i_{v,m} = S_a i_{loc} = S_a(i_F + i_{dl} + i_{F,side}) \tag{4.16}$$

where S_a is the active specific surface area of the electrode material and the description of each current can be found in the following sections. The particles are assumed to be spherical, giving the following expression for the active specific surface area

$$S_a = \frac{3\epsilon_s}{r_p} \tag{4.17}$$

where ϵ_s is the volume fraction of electrode material and r_p is the particle radius [13, 91].

4.1.3 Electrochemical Reactions

The electrochemical reactions are considered to be of intercalation and deintercalation type and occur on the surface of the active electrode particles. During the intercalation Li^+ enter into the material are reduced and during deintercalation they are oxidised back to Li^+, which exit the material. The reaction kinetics is assumed to follow the Butler-Volmer (B-V) equation

$$i_F = i_0\left(\exp\left(\frac{\alpha_a F\eta}{RT}\right) - \exp\left(\frac{-\alpha_c F\eta}{RT}\right)\right) \tag{4.18}$$

with a concentration dependent exchange current density

$$i_0 = F(k_c)^{\alpha_a}(k_a)^{\alpha_c}(c_{s,max} - c_s)^{\alpha_a}(c_s)^{\alpha_c}\left(\frac{c_l}{c_{l,ref}}\right)^{\alpha_a} \tag{4.19}$$

and

$$\eta = \phi_s - \phi_l - E_{eq}(c_s, T) - \Delta\phi_{s,film} \tag{4.20}$$

where η is the overpotential, E_{eq} the equilibrium potential of electrode material, α the transfer coefficient, k the reaction rate coefficient, and $\Delta\phi_{s,film}$ is the potential difference from the resistive film that always is formed on the graphite particles (SEI) and to a smaller extent on the PE particles (CEI) found as

$$\Delta\phi_{s,film} = i_{tot}R_{film} \tag{4.21}$$

where R_{film} is the film resistance [13].

4.1.4 Double Layer Capacitance

The double layer capacitance, $C_{dl,i}$, is assumed to arise between the electrolyte and all surfaces in the electrode components. The double layer is assumed to be charged by Li^+ and the current densities are calculated from

$$i_{dl,s} = C_{dl,s}\frac{\partial(\phi_s - \phi_l - \Delta\phi_{s,film})}{\partial t} \tag{4.22a}$$

$$i_{dl,add} = C_{dl,add}\frac{\partial(\phi_{add} - \phi_l)}{\partial t} \tag{4.22b}$$

$$i_{dl,cc} = C_{dl,cc}\frac{\partial(\phi_{cc} - \phi_l)}{\partial t} \tag{4.22c}$$

where (4.22a) is the contribution from the active material, (4.22b) from the conductive additives and (4.22c) from the ccs [91]. The double layer capacitance affects the results when simulating the dynamic behaviour. Due to uncertainties in the parameters for (4.22c) and (4.22b) only $i_{dl,s}$ is included in the model. The largest surface area is the active material surface area, hence it is common to neglect the contributions from conductive additives and cc, as they are assumed to be small.

4.1.5 Mass Transport in the Electrode Materials

The particles are assumed to be spherical and to account for the concentration in the active material a pseudo dimension is added to the model. The

transport of Li^+ in the particles is assumed to occur through diffusion, which is modelled by Fick's second law [92]

$$\frac{\partial c_s}{\partial t} = \frac{D_s}{r^2}\frac{\partial}{\partial r}\left(\frac{r^2 \partial c_s}{\partial r}\right) \tag{4.23}$$

with the boundary conditions

$$\frac{\partial c_s}{\partial r}|_{r=0} = 0 \tag{4.24}$$

$$-D_s \frac{\partial c_s}{\partial r}|_{r=r_p} = \sum_m \frac{i_{F,m}}{F} \tag{4.25}$$

4.2 Ageing Model

The first ageing mechanism included in the model is SEI growth at the NE resulting in loss of Li, reduced electrolyte volume and increased resistance. The second is solvent oxidation leading to Mn dissolution and loss of active material at the PE. Finally, the cross talk between the electrodes is included, where Mn^{2+} migrate to the NE and interact with the SEI layer and affect its properties.

4.2.1 Ageing Through SEI Growth

During the formation of the cell an SEI layer is formed at the graphite surface [5, 17, 94]. This inner SEI layer consists mainly of degradation products from the salt and additives and cell design efforts ensure that it will be passivating. In this work, since all testing have been performed on commercial cells, it is assumed that this inner SEI has already formed at the manufacturer and that this layer, $d_{0,SEI}$, is a few nm thick, in the electron tunnelling range of approximately 2-3.7 nm [61, 95]. After this initial formation further degradation of the salt is much slower and is in this work assumed to be negligible.

Many models account for an SEI reaction occurring on the electrode|electrolyte interface [19, 24, 28, 29]. However, that requires transport of the larger solvent molecules through the SEI layer to the reaction-site or that cracking of the SEI layer exposes fresh electrode surface, as considered in [28, 29]. Further, the composition of the SEI with less degraded solvent products in the outer layer indicates that the SEI layer is growing from the outside, the SEI|electrolyte interface, and not from the electrode|SEI interface [11]. Therefore, in this work the outer SEI is assigned to originate from decomposition reactions of the solvent at the SEI|electrolyte interface [20]. The

growth rate is considered to be limited by conduction and diffusion of electrons through the SEI [11, 20].

The solvent consists of EC, DMC, EMC, and an unknown number of additives. The concentrations of the different solvents and additives are unknown, therefore only decomposition reactions of EC are considered for the SEI growth in this model. Several different products and reaction schemes have been proposed over the years. Many reports have in common that the main products are considered to be dilithium ethylene dicarbonate ($(LiOCO_2CH_2)_2$) [94,96] and lithium carbonate (Li_2CO_3) [94,97]. The reactions considered are reduction of EC to $(LiOCO_2CH_2)_2$ and further decomposition [98], or electrochemical reduction [99] of $(LiOCO_2CH_2)_2$ according to [100]:

$$2\,(CH_2O)_2CO + 2\,e^- + 2\,Li^+ \rightarrow (LiOCO_2CH_2)_2 + C_2H_4 \tag{4.26a}$$

$$(LiOCO_2CH_2)_2 \rightarrow Li_2CO_3 + C_2H_4 + CO_2 + \frac{1}{2}\,O_2 \tag{4.26b}$$

$$(LiOCO_2CH_2)_2 + 2\,Li^+ + 2\,e^- \rightarrow 2\,Li_2CO_3 + C_2H_4 \tag{4.26c}$$

The end product of reactions (4.26b) and (4.26c) are containing Li_2CO_3, which in the model is considered to be the final product. The SEI is assumed to grow only during charging and the decomposition reaction is triggered by the overpotential

$$\eta_{SEI} = \phi_s - \phi_l - \Delta\phi_{s,SEI} - E_{eq,SEI} \tag{4.27}$$

where $E_{eq,SEI} = 0.4$ V vs Li/Li^+ [19]. The SEI growth increases the resistance in proportion to the thickness of the SEI layer, d_{SEI}:

$$R_{SEI} = \frac{d_{0,SEI}}{\kappa_{0,SEI}} + \frac{d_{SEI} + \Delta d_{SEI}}{\kappa_{SEI}} \tag{4.28}$$

where $\kappa_{0,SEI}$ is the ionic conductivity of the inner SEI layer and κ_{SEI} is the ionic conductivity of the outer SEI layer.

The thickness is determined by the accumulated amount of Li^+ lost due to side reactions taking place at the specific surface of the SEI

$$\Delta d_{SEI} = \frac{Q_{SEI} M_{SEI}}{2 S_{a,SEI} F \rho_{SEI}} \tag{4.29}$$

where M_{SEI} is the average molar mass of the products formed in the SEI (Li_2CO_3) and ρ_{SEI} the density of Li_2CO_3. The specific surface area of the SEI is calculated from

$$S_{a,SEI} = \frac{3(\epsilon_{s,neg} + \epsilon_{s,SEI})}{r_{p,neg} + d_{SEI}} \tag{4.30}$$

The calculation of $\epsilon_{s,SEI}$ is presented in section 4.2.1. Q_{SEI} (C/m^2) is the irreversible capacity loss to the side reactions directly proportional to the concentration of Li^+, c_{SEI}, bound in the SEI layer

$$Q_{SEI} = c_{SEI} F \tag{4.31}$$

The concentration accumulated in the SEI layer is calculated from

$$\frac{dc_{SEI}}{dt} = \frac{-i_{SEI} S_{a,neg}}{F} \tag{4.32}$$

where the current from the SEI reactions is assumed to follow the B-V kinetics with a concentration dependence

$$i_{F,SEI} = i_{0,SEI} \left(\frac{c_p}{c_{p,ref}} \exp\left(\frac{\alpha_a F \eta_{SEI}}{RT} \right) - \frac{c_+}{c_{+,ref}} \frac{c_l}{c_{l,ref}} \exp\left(\frac{-\alpha_c F \eta_{SEI}}{RT} \right) \right) \tag{4.33}$$

where the subscript p stands for the product produced in the side reaction. The equation is simplified to a cathodic Tafel approximation by assuming an irreversible (only cathodic) reaction, thus, dropping the first term of (4.33) gives [19]

$$i_{F,SEI} = -i_{0,SEI} \frac{c_+}{c_{+,ref}} \frac{c_l}{c_{l,ref}} \exp\left(\frac{-\alpha_c F \eta_{SEI}}{RT} \right) \tag{4.34}$$

The SEI exchange current density is estimated from the calendar ageing data, see section 5.2.1, and is assumed to follow the Arrhenius temperature dependence. For current rates at C/10 the SEI growth has proven to follow the $t^{1/2}$ relation [17,20,29]. As the lifetime test results in this thesis are conducted at higher C-rates and the results indicate a current relation for the SEI growth, a current relation was added to the exchange current density normalising the local current density over the local 1C current density

$$i_{0,SEI} = A_{0,SEI} \cdot \exp\left(\frac{-E_{a,SEI}}{RT} \right) \cdot \frac{i_{loc}}{i_{1C,loc,neg}} \tag{4.35}$$

where

$$i_{1C,loc,neg} = \frac{-i_{1C}}{S_{a,neg} L_{neg}} \tag{4.36}$$

Based on the thickness of the SEI layer from the PM analysis [78] the thickness should be in the range of 50 nm at EOL for a cell tested in a SOC interval higher than 50% SOC and less if tested in a SOC interval below that.

As the SEI layer supposedly grow from the interface of the SEI|Electrolyte, the side reactions are assumed to become limited by the electric conductivity and diffusion of electrons in the SEI [11, 20]. The conductivity of the SEI is considered to be negligible and therefore only diffusion of electrons in the

SEI is considered. A first order mass transport limiting current through a Nernst boundary layer was assumed [29],

$$i_{SEI} = \frac{i_{F,SEI}}{1 + \frac{i_{F,SEI}}{i_{lim}}} \tag{4.37}$$

The limiting current was related to the diffusion coefficient for the e^- through the SEI layer according to

$$i_{lim} = -\frac{c_l D_{e^- SEI} F}{d_{SEI}} \tag{4.38}$$

where c_l is the solvent bulk concentration, and $D_{e^- SEI}$ the diffusion coefficient for electrons in the SEI layer [20].

Porosity Change due to SEI Growth

With an increasing SEI layer the volume balance in the electrode needs to be adjusted. The amount of active material is kept constant while the increase in the SEI layer is reducing the volume fraction of the electrolyte in the porous structure. This is a rough estimation, since the SEI layer is likely to reduce the porosity of the active material and will not grow evenly on all surfaces. It may also isolate parts of the active material from the cc. These effects will be neglected. The electrolyte volume fraction is decreased according to

$$\epsilon_{l,neg} = 1 - \epsilon_{s,neg} - \epsilon_{add,neg} - \epsilon_{s,SEI} \tag{4.39}$$

where $\epsilon_{s,neg}$ and $\epsilon_{add,neg}$ are constants, and the SEI volume fraction is calculated from

$$\epsilon_{s,SEI} = V_{SEI}/V_{tot} = d_{SEI} S_{a,neg} \tag{4.40}$$

4.2.2 Mn Dissolution, Migration and Deposition

The positive material consists of a mixture of NMC and LMO, therefore, different possibilities for Mn dissolution exists. Research has shown that there are a few different processes that can lead to Mn dissolution; loss of oxygen from the electrode structure, Jahn-Teller distortions in LMO, and oxidation of the electrolyte leading to proton attack on the PE [4, 53–55].

Mn Dissolution

In LMO the main loss of active material has been seen when cycling above 4 V. A similar process has been reported for NMC. The process increased rapidly above 4.3 V [54] and is in this work assumed to be caused by TM

dissolution due to proton attack on LMO/NMC. The protons are produced by oxidation of the solvent on the conductive carbon in the PE. The solvents involved and the main reactions are not known, and accordingly the main product is therefore not known. The reaction is therefore assumed to be a general oxidation reaction according to

$$\mathrm{S} \rightarrow \mathrm{S}^{'} + \mathrm{e}^{-} + \mathrm{H}^{+} \tag{4.41}$$

where S is the solvent and S' the decomposed solvent. The reaction is assumed to be irreversible and follows the anodic Tafel equation

$$i_{S,ox} = S_{cond.carbon} i_{0,ox} \exp\left(\frac{\alpha_{a,ox} F \eta_{ox}}{RT}\right) \tag{4.42}$$

where $S_{cond.carbon}$ is the specific surface of conductive carbon, $\alpha_{a,ox}$ is the anodic charge transfer coefficient assumed to be 0.5, the overpotential is

$$\eta_{ox} = \phi_s - \phi_l - E_{eq,ox} \tag{4.43}$$

according to [32], and the exchange current density, assumed to follow the Arrhenius equation for the temperature dependence, is estimated from a calendar ageing test at 90% SOC (Section 5.2.1)

$$i_{0,ox} = A_{0,ox} \cdot \exp\left(\frac{-E_{a,ox}}{RT}\right) \tag{4.44}$$

The surface area of conductive carbon used in batteries varies with a factor 100 between different types, 13-1635 m^2/g [101]. The specific surface of conductive carbon, $S_{cond.carbon}$, is therefore difficult to know and has been assumed to be a fraction, $f_{cons.carbon}$, of the specific surface of the active material according to

$$S_{cond.carbon} = S_{a,pos,0} f_{cond.carbon} = S_{a,pos,0} \epsilon_{add,pos} \tag{4.45}$$

where the fraction is related to the volume fraction of the additives.

The oxidation process is fairly unknown and it is assumed that only a fraction of the oxidation current, f_{H^+}, will generate protons

$$i_{ox,H^+} = f_{H^+} i_{S,ox} \tag{4.46}$$

Dai et al. [31] assumed that water was produced in the reaction for the proton attack, however in this project it has not been possible to study the reaction schemes for the proton attack experimentally. A more generalised reaction, only accounting for the charge balance, is therefore assumed according to

$$\mathrm{S/S}^{'} + 2\mathrm{H}^{+} + 2\,\mathrm{LiMn_2O_4} \rightarrow 2\mathrm{Li}^{+} + 2\,\mathrm{e}^{-} + \mathrm{Mn}^{2+} + \frac{3}{2}\mathrm{Mn_2O_4} + \mathrm{S}^{''} \tag{4.47}$$

where $S^{''}$ is some generalised product containing hydrogen and other possible components such as oxygen.

Two protons are needed to dissolve one Mn^{2+} and the dissolution rate is concentration dependent and described by

$$i_{Mn} = f_{Mn,diss} k_{Mn,diss} F c_{H^+} \tag{4.48}$$

where $f_{Mn,diss}$ is a fraction coefficient to account for that only a part of the dissolved Mn^{2+} will be free in the electrolyte, and $k_{Mn,diss}$ is the rate constant. Some of the Mn^{2+} will form MnF_2 and other products [32]. The products are assumed to have poor solubility in the electrolyte and are therefore assumed to deposit on the available surfaces in the cell. The deposits on the PE surface have proven to be limited by the oxidation, "self cleaning" process, and only a small fraction will deposit and form an CEI. This film growth and resistance is assumed to be small and is neglected in this model.

The dissolution of Mn will lead to loss of active material. Cracking of NMC particles due to stress in intergranual interfaces is one mechanism for loss of capacity [67]. Here the amount of Mn dissolution will be proportional to the loss of active material. To account for particle cracking, structure distortion, as well as isolation of active material, the material loss is enhanced by a coefficient k_{iso} according to

$$\frac{\partial \epsilon_{matloss,pos}}{\partial t} = k_{iso} \frac{S_{a,pos} i_{Mn} V_{m,pos}}{F} \tag{4.49}$$

where $V_{m,pos}$ is the molar volume of the PE material [32].

4.2.3 Mn Deposition on the Negative Electrode

The mechanism behind Mn^{2+} deposition on the NE is still not fully understood. In previous work, deposition of metallic Li has been used [30–32]. However, the Mn found on the NE in the PM analysis had a valence of 2+. A metathesis reaction has been considered [38], as well as step reactions where Mn first is deposited in the metallic state and then re-oxidised to Mn^{2+} before being involved in a catalytic degradation of the electrolyte [68].

The commonly used reduction reaction, Mn^{2+} to metallic Mn, has two possible faults. Mn is quite electropositive and should therefore be hard to reduce at the NE, and the concentration is also very low further reducing the reduction potential. Therefore, a hypothesis is that the dissolved Mn^{2+} is deposited on the NE by a chemical reaction. The reaction is assumed to involve the negative ion, PF_6^-, to maintain the charge balance in the electrolyte. It is however likely that the solvent, S, and other products from the SEI or oxidation reactions participate in the reaction

$$Mn^{2+} + 2{PF_6}^- + S/S^{'}/S^{''} \rightarrow MnS^{'''} \tag{4.50}$$

and accordingly, the product $S^{'''}$ is defined.

The deposition rate of Mn^{2+} is assumed to be proportional to the concentration of Mn^{2+} in the electrolyte

$$\frac{dc_{Mn,dep}}{dt} = -k_{Mn,dep} c_{Mn^{2+}} S_{a,SEI} \tag{4.51}$$

where $k_{Mn,dep}$ is the deposition rate and $c_{Mn^{2+}}$ the concentration of Mn^{2+}.

Transport of H^+ and Mn^{2+}

The concentrations of H^+ and Mn^{2+} will be low and are not assumed to contribute to the current transported in the electrolyte. The Nernst-Planck equation for the transport of matter in electrochemical systems in diluted electrolyte can therefor be used

$$N_T = -z_i u_i F c_i \nabla\phi - D_i \nabla c_i + c_i \mathbf{v} \tag{4.52}$$

where z_i is the ionic charge of species i, u_i the ionic mobility, F Faradays constant, c_i the concentration, ϕ the potential, D_i the diffusion coefficient and $\mathbf{v}$ the fluid velocity. Using this the H^+ balance in the electrolyte for the PE is

$$\epsilon_{l,+} \frac{dc_{H^+}}{dt} = \nabla\cdot\left[\frac{D_{H^+,eff} F c_{H^+}}{RT}\nabla\phi_l + D_{H^+,eff}\nabla c_{H^+}\right] + \frac{1}{F}(i_{ox,H^+} - 2S_+ i_{Mn}) \tag{4.53}$$

where $D_{H^+,eff}$ is the effective diffusion of H^+ and c_{H^+} the H^+ concentration. For the separator and the NE the balance is

$$\epsilon_{l,sep/-} \frac{dc_{H^+}}{dt} = \nabla\cdot\left[\frac{D_{H^+,eff} F c_{H^+}}{RT}\nabla\phi_l + D_{H^+,eff}\nabla c_{H^+}\right] \tag{4.54}$$

The balance of Mn^{2+} in the three components is given by:

$$\epsilon_{l,+} \frac{dc_{Mn^{2+}}}{dt} = \nabla\cdot\left[\frac{2D_{Mn^{2+},eff} F c_{Mn^{2+}}}{RT}\nabla\phi_l + D_{Mn^{2+},eff}\nabla c_{Mn^{2+}}\right] + \frac{1}{F}(S_+ i_{Mn}) \tag{4.55}$$

$$\epsilon_{l,sep} \frac{dc_{Mn^{2+}}}{dt} = \nabla\cdot\left[\frac{2D_{Mn^{2+},eff} F c_{Mn^{2+}}}{RT}\nabla\phi_l + D_{Mn^{2+},eff}\nabla c_{Mn^{2+}}\right] \tag{4.56}$$

$$\epsilon_{l,-} \frac{dc_{Mn^{2+}}}{dt} = \nabla\cdot\left[\frac{2D_{Mn^{2+},eff} F c_{Mn^{2+}}}{RT}\nabla\phi_l + D_{Mn^{2+},eff}\nabla c_{Mn^{2+}}\right] + (S_{SEI} c_{Mn^{2+}}) \tag{4.57}$$

where $D_{Mn^{2+},eff}$ is the effective diffusion of Mn^{2+}.

Mn and SEI growth

The dissolved Mn^{2+} is transported through the electrolyte to the NE and interacts with the SEI. Gilbert et al. [54] showed that in an NMC/graphite cell each Mn^{2+} could bind up to 95 Li^{+}s in the SEI. Zhan et al. [38] showed that for an LMO/graphite system, the impedance increase is proportional to the concentration of Mn in the SEI.

The ionic conductivity in an electrolyte is closely related to the concentration

$$\kappa = F^2 \sum_i z_i^2 u_i c_i \tag{4.58}$$

where u_i the mobility of species i. As Li^{+} is smaller than Mn^{2+} and have a much higher mobility it is reasonable that depositing Mn^{2+} in the SEI will reduce the ionic conductivity. To account for this change in the model, the resistance data by Zhan et al. [38] (Figure 4.1) were fitted to an empirical expression

$$R_{SEI}(cyc) = 0.8 + \frac{5.44 \cdot 10^{-4} cyc}{0.01075 - 9.84 \cdot 10^{-7} c_{Mn,p.p.m}(cyc)^{1.5}} \tag{4.59}$$

This have to be considered as a rough estimation. A linear increase was assumed as there were no data available for the SEI thickness or the c_{Mn} increase with cycles.

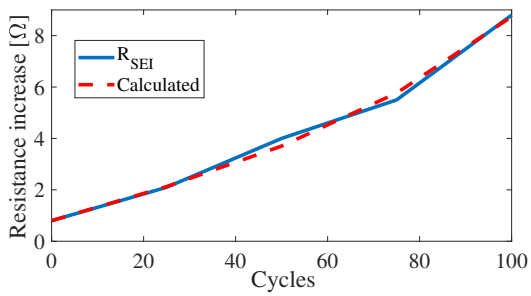

Figure 4.1: Resistance data measured by [38] vs calculated R_{SEI} according to (4.59).

The denominator in the fraction is used to describe the change in ionic conductivity

$$\kappa^*_{SEI} = \kappa_{SEI,0} - K c^{1.5}_{Mn,dep} \tag{4.60}$$

where κ^*_{SEI} replaces κ_{SEI} in (4.28), $\kappa_{SEI,0}$ is the initial ionic conductivity and K is the factor governing the speed of the change. In the model, K was

adjusted to the resistance values seen for the tested cell. At a certain concentration c_{Mn} the equation will go negative, therefore a minimum allowed value for the conductivity was set to $1{\cdot}10^{-6}$ S/m.

Chapter 5

Model Parameterisation and Validation

One of the major disadvantages with physics-based models is the large number of material and design parameters needed. Many can be readily measured, while others require sophisticated experiments, and some are not measurable at all. Together with uncertainties in the measured parameters and cross-parameter relations, the task of parameterising a model can be daunting. Physics-based models can, however, provide an invaluable insight to what is actually going on in a cell over its lifetime, which makes the task worthwhile to pursue. Over time, with improved analysis methods and insights into material properties, the models will become increasingly powerful.

5.1 Model Parameterisation

To parameterise this model a combination of half cell and full cell measurements has been used, as well as optimisation simulations towards pulse measurement data. A literature study of parameters which were not possible to measure in this project was performed to complete the parameter set.

5.1.1 Electrolyte Parameterisation

In this project there was no possibility to measure or analyse the electrolyte. Therefore, all parameters for the electrolyte had to be taken from the literature. The most important parameters for the electrolyte is the ionic conductivity and diffusion.

The electrolyte composition in commercial cells is highly complex, in addition to the solvents, the electrolyte also includes additives with various properties dedicated to form a stable SEI, flame-retardants for safety purposes, etc. The electrolyte composition is proprietary to the battery manufacturers and it is thus very difficult to get information about the composition. However, in this case the main components were given as EC, DMC and EMC with the salt $LiPF_6$.

Schmalstieg et al. [33] did an evaluation and parameterisation of the electrolyte in a commercial cell with the same main components as the electrolyte used in this thesis. The relation was derived for both the ionic conductivity and the ion diffusivity

$$\sqrt{\frac{\kappa_l(c_l,T)}{c_l}} = -5.384+0.03213\cdot T-0.00368\cdot c_l\cdot T+1.320\cdot\exp(-2.235\cdot c_l) \quad (5.1)$$

where κ_l is the ionic conductivity in mS/cm, c_l the salt concentration in mol/l and T the temperature in K. For highly dilute electrolytes the diffusion coefficient, D_l, is related to the conductivity according to the Einstein relationship [33],

$$D_l = \frac{\kappa_l(c_l,T)RT}{F^2z^2c_l} \quad (5.2)$$

For the concentrated electrolytes this is not valid, however here it is used as an estimate. The estimated value for D_l for the concentration range is in range to previously presented values [102]. The transport number, t_+, were set to 0.38 [102] and the thermodynamic enhancement factor, $\left(1+\frac{\partial \ln f_\pm}{\partial \ln c_l}\right)$, to 2 [91].

5.1.2 Electrode Parameterisation

The most important electrode parameters are the equilibrium potential, exchange current density, Li diffusion, and electrode capacity. To estimate the capacity of the electrode, the maximum Li concentration and the porosity are needed. The porosity, ϵ, for the 2PD type of models can be considered as a volume fraction, since each particle is assumed to be solid and the void between particles is what is referred to as the porosity. Hence, these models do not take into account the true particle porosity.

Maximum Li Concentration in Electrodes

The maximum Li concentration in the electrodes was calculated from the density over the molar mass using literature values. Graphite has a molar mass of 72.06 g/mol and a density of 2.24 g/cm^3 [103], this gives a maximum

Li concentration of 31085 mol/m^3. The small deviations in the density for graphite reported in the literature, translates to small deviations also for the maximum Li concentration.

For the mixed electrode, the maximum Li concentration was estimated based on the maximum Li concentration of the two materials and the material wt%. The values used for NMC are 96.46 g/mol and 4.77 g/cm^3 [104], and for LMO the used values are 180.82 g/mol and 4.28 g/cm^3 [105]. The maximum Li concentration for the mixed material was established in combination with the electrode potential curves presented in [33, 106]. At 3 V both LMO and NMC have a 1:1 Li:NMC/LMO relation. Based on this, the maximum Li concentration was estimated to

$$\begin{aligned} c_{s,max,pos} &= 0.3c_{s,maxLMO} + 0.7c_{s,maxNMC} \\ &= 0.3 \cdot 23670 + 0.7 \cdot 49451 = 41717 \text{ mol/m}^3 \end{aligned} \tag{5.3}$$

At 4.5 V the lithiation degree was estimated to be 0 for LMO and 0.32 for NMC [33] resulting in

$$\begin{aligned} c_{s,4.5V,pos} &= 0.3c_{s,maxLMO} \cdot 0 + 0.7c_{s,maxNMC} \cdot 0.32 \\ &= 0.3 \cdot 0 + 0.7 \cdot 0.32 \cdot 49451 = 11077 \text{ mol/m}^3 \end{aligned} \tag{5.4}$$

Equilibrium Potential

The NE and PE potentials were measured at UU in half cells using lithium metal as counter electrode. The pseudo equilibrium electrode potentials, Figure 5.1, were calculated as functions of the state of lithiation (SOL) from slow charge and discharge measurements, at C/20.

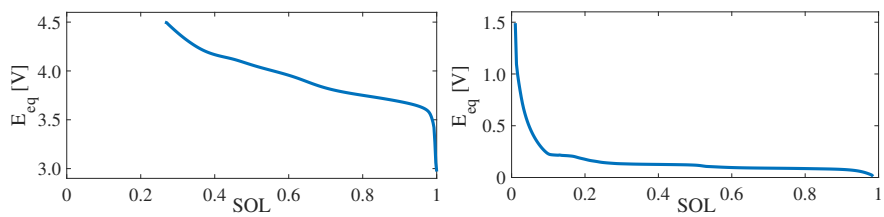

(a) (b)

Figure 5.1: Equilibrium potential curves calculated from measurements for the (a) PE and (b) NE as a function of the SOL.

The definition of SOL for each electrode material is, in this thesis, the Li concentration divided by the maximum Li concentration for the respective material, i.e. the equilibrium potential as a function of Li concentration. The highest possible SOL is therefore related to the maximum degree of lithiation.

For the mixed electrode material, the measured potential curve was assumed to go from 100% to 26.6% SOL. For the graphite it was assumed that it never reached full lithiation or delithiation and the equilibrium potential curve goes between 98.5 and 1% SOL.

Volume Fraction

The volume fraction of active material was estimated based on half cell measurements and then tuned with a measured ICA for the right ratio between the electrodes. A possible interval for the volume fraction of the active materials was calculated, the measured half cell capacity over the theoretical capacity was used to get the minimum volume fraction for the electrode. The highest possible volume fraction was calculated from the measured density of the electrode (including binder, conductive carbon and other additives) over the density of pure graphite and NMC/LMO, respectively,

$$0.54 < \epsilon_{s,neg} < 0.71 \tag{5.5}$$

$$0.43 < \epsilon_{s,pos} < 0.61 \tag{5.6}$$

The theoretical capacities for the materials used in this study, graphite, NMC, and LMO are 372 mAh/g, 280 mAh/g, and 148 mAh/g respectively.

Exchange Current Density

The exchange current density in this model is assumed to be concentration dependent (4.19), related to a rate constant, the Li^+ concentration in the electrolyte and the Li concentration at the electrode surface. The exchange current density can be calculated from EIS measurements via the charge transfer resistance [33]. It can also be calculated from dc polarisation measurements, Tafel measurements, from the slope of the linear part of the Tafel curve [107]. In this project, there has been no possibility to perform the latter measurements and accordingly literature values for the reaction rate constant had to serve as initial input. The values were estimated to be within the range $1{\cdot}10^{-11}$-$5{\cdot}10^{-10}$ [13, 32, 33, 37].

Solid Li Diffusion Coefficient

The diffusion coefficient is in most models set to a constant value and assumed not to be SOL dependent. This is a rather poor assumption, since measurement results suggest that it can vary greatly with the SOL in the electrode. A GITT test of the full cell was performed in an attempt to extract the diffusion coefficients of the two materials simultaneously, using a least square

(LS) optimisation of the pulse voltage to extract the values. However, this resulted in large fluctuations in the diffusion coefficients for both materials.

Accordingly, the diffusion coefficient of graphite had to be taken from literature [108] with some minor adjustments to the SOL and scaling to the diffusion length (Figure 5.2a). Levi et al. assumed that the diffusive length is equal to the thickness of the electrode and calculated the diffusion coefficient based on this. To instead base the diffusion coefficient on the time constant, the values in [108] are scaled in relation to the different diffusion lengths according to

$$D_{s,neg} = \frac{D_{measured}}{l^2} r_{p,neg}^2 \tag{5.7}$$

where l=8.8μm is the electrode thickness in [108] and $r_{p,neg}$ the particle radius used in this model.

The mixture of NMC and LMO in the PE caused some difficulties in finding literature values. For this reason the diffusion coefficient was extracted from the LS optimisation model using the pulse data from a fresh cell RPT. By using two different current levels for the pulses and only optimising for one parameter proved to give a better result. Due to the high uncertainty in the values, the results were compared to diffusion coefficients for LMO [109] and NMC [110] in the literature, after scaling according to (5.7) (Figure 5.2b). The optimised values turned out to be in the same range. The diffusion coefficient was slightly adjusted at the high SOL level to match the discharge curve, since the estimated diffusion during discharge above 90% SOL proved to be too slow.

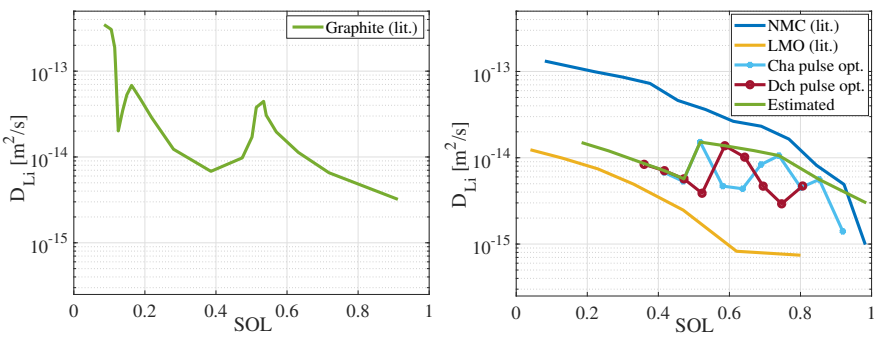

(a) (b)

Figure 5.2: Diffusion coefficients as a function of SOL for (a) graphite taken from [108] and (b) the result of the optimisation of the mixed PE and literature values for LMO [109] and NMC [110].

5.2 Ageing Parameters

The model parameterisation is based on the experimental test results. The reader is referred to Chapter 6 for a full disclosure of results and analyses pertinent to the ageing parameters.

5.2.1 Exchange Current Density for Side Reactions

The exchange current density for the SEI growth and its temperature dependence was estimated based on calendar ageing data at 15% SOC. At 15% SOC there should be a limited amount of dissolution of Mn from the PE. The exchange current was assumed to follow the Arrhenius equation

$$A = A_0 \exp\left(\frac{-E_a}{RT}\right) \tag{5.8}$$

where the activation energy, E_a, and the pre-exponential factor, A_0, were estimated from the natural logarithm of the change in capacity over initial capacity vs the inverse of temperature, similar to the process used in [35]. However, the results from the analysis did not show a clear trend (Figure 5.3a). This is most likely due to the slow degradation seen in the calendar data at 15% SOC (Figure 6.1).

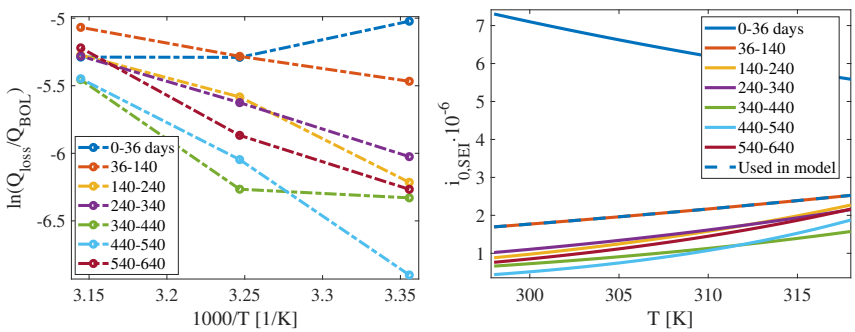

(a) (b)

Figure 5.3: (a) The logarithm of the normalised capacity loss vs. the inverse temperature for calendar data at 15% SOC for different storage times. (b) The exchange current density with the estimated values of E_a and A_0 as a function of temperature.

Table 5.1 shows the parameter values from the curve fitting and the model parameter values. The model values were chosen from the curve fit early in the ageing process, 34-140 days, since the SEI growth is assumed to slow

down as the thickness of the layer increases. The resulting exchange current densities can be seen in Figure 5.3b.

Table 5.1: Activation energies and pre-exponential factors obtained from the calendar ageing for the cells tested at 15% SOC and the values used in the model.

Days stored	$E_{a,SEI}$ [kJ/mol]	$A_{0,SEI}$[1/h]
0-34	10.57	$1.0252 \cdot 10^{-7}$
34-140	-15.7	$9.5833 \cdot 10^{-4}$
140-240	-37.23	2.9651
240-340	-29.34	0.1419
340-440	-34.12	0.6338
440-540	-57.29	$4.8359 \cdot 10^{3}$
540-640	-41.12	12.3106
Model values	-15.7	$9.5833 \cdot 10^{-4}$

To estimate the exchange current density for the oxidation on the conductive carbon in the PE, the same procedure was followed using the calendar data at 90% SOC (Table 5.2, Figure 5.4). The model values were calculated from the average of the three most similar results, so that the resulting exchange current density approximately was the mean of all exchange current densities (excluding 0-34 days data).

Table 5.2: Activation energies and pre-exponential factors obtained from the calendar ageing for the cells tested at 90% SOC. The model values were calculated from the average of the grey values.

Days stored	$E_{a,ox}$ [kJ/mol]	$A_{0,ox}$[1/h]
0-34	-18.18	0.0276
34-106	-39.95	33
106-208	-42.78	83
208-306	-46.77	479
306-408	-47.77	503
408-508	-49.11	1110
508-606	-46.82	388
Model value	-47.12	457

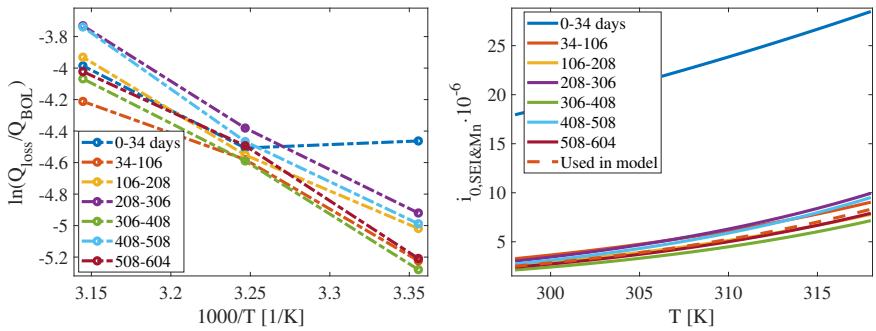

(a) (b)

Figure 5.4: (a) The logarithm of the normalised capacity loss vs. the inverse temperature for calendar data at 90% SOC for different storage times. (b) The exchange current density with the estimated values of E_a and A_0 as a function of temperature.

5.2.2 Loss of PE Material

The enhancement factor for the loss of PE material was estimated by using the results from the ESMLE presented in Section 6.4.2 (Figure 6.13). The amplitude was estimated based on the results from cell #9 (+2C/-2C, 60-70% SOC), where the PE material loss was estimated to be around 8%. The results from cell #21 (+1C/-1C 10-20% SOC), #22 (+2C/-2C 10-20% SOC), and #23 (+4C/-4C 10-20% SOC) tested at 35°C show that there is a C-rate dependence to the material loss in the PE, a normalisation over the C-rate was therefore introduced to account for this

$$k_{iso} = 1250 \cdot \frac{i_{loc}}{i_{1C,loc,pos}} \tag{5.9}$$

where

$$i_{1C,loc,pos} = \frac{-i_{1C}}{S_{pos} L_{pos}} \tag{5.10}$$

5.2.3 SEI Ionic Conductivity

The inner SEI layer ionic conductivity was estimated to be $3{\cdot}10^{-5}$ S/m. The change in the ionic conductivity due to increase of Mn in the SEI was estimated based on the resistance increase for cell #18 (+1C/-2C, 10-90% SOC). However, matching the resistance increase for cell #18 resulted in too high resistance for simulations of cell #9, thus a compromise had to be made. For the change in ionic conductivity K =$3{\cdot}10^{-5}$ was used.

5.3 Model Parameters

The complete set of parameters used in the electrochemical model is given in Tables 5.3, 5.4 and 5.5. For a detailed description of each parameter see Chapter 4 and List of Symbols. The parameters collected from literature are recognised by the source. Parameters measured, estimated, assumed or calculated are noted by *m*, *e*, *a* and *c*. Measurements performed at Uppsala University are denoted UU.

Table 5.3: Parameters for the cc and porous electrodes used in the simulations. For descriptions of the parameters see Chapter 4.

Parameter	PE	NE	Source
L_s [μm]	74	64.5	*m* UU
L_{cc} [μm]	20/2	10/2	*m* UU
$\mathrm{SOC}_{init} = 0$	0.922	0.0291	*e*
$c_{s,max}$ [mol/m^3]	41717	31085	*c* from [44] & *m* UU
ϵ_s	0.507	0.585	*e* from *m* UU
ϵ_{add}	15% of ϵ_s	8.5% of ϵ_s	*a*
ϵ_l	0.417	0.379	*c*
r_p [μm]	10.9/2	14.7/2	*m* UU
$D_s(SOL)$ [m^2/s]	$3{\cdot}10^{-15}$-$1.5{\cdot}10^{-14}$	$3.2{\cdot}10^{-15}$-$3.5{\cdot}10^{-13}$	*e* & [111]
σ_s [S/m]	100	100	COMSOL
σ_{cc} [S/m]	$3.546{\cdot}10^7$	$5.998{\cdot}10^7$	COMSOL
β_s	1.5	1.5	[112]
β_l	2.98	2.6	[91]
$\alpha_{a/c}$	0.5	0.5	[19]
$k_{a/c}$ [m/s]	$2{\cdot}10^{-10}$	$1{\cdot}10^{-10}$	*a*
R_{film} [$\mu\Omega$m^2]	0.1	0.1+R_{SEI}	*a*

Table 5.4: Cell and electrolyte parameters used in the simulations.

Parameter	Value	Source
A_{cell} [m^2]	1.085	m
T [°C]	25	
Q_0 [Ah]	26	m
i_{1C} [A/m^2]	23.96 A/m^2	c
C_{dl} [F/m^2]	0.2	COMSOL
L_{sep} [μm]	26.5	Manufacturer
c_l [mol/m^3]	1000	Manufacturer
$D_l(c_l, T)$ [m^2/s]	1-4·10^{-8}	[33]
$\kappa_l(c_l, T)$ [S/m]	0.05-1.5	[33]
$\epsilon_{l,sep}$	0.39	a
$\beta_{l,sep}$	3.15	[91]
$\left(1 + \frac{\partial \ln f_{\pm}}{\partial \ln c_l}\right)$	2	[91]
t_+	0.38	[102]
$V_{m,salt}$ [m^3/mol]	59·10^{-6}	[91]
$V_{m,solv}$ [m^3/mol]	88·10^{-6}	[91]

Table 5.5: Model parameters used for the SEI layer growth and manganese dissolution.

Parameter	Value	Source
$E_{eq,SEI}$ [V]	0.4	[19]
$E_{eq,ox}$ [V]	4.05	a
$i_{0,SEI}(T)$ [A/m^2]	1.7·10^{-6}-2.5·10^{-6}	e
$i_{0,S,ox}$ [A/m^2]	2.5·10^{-6}-8.3·10^{-6}	e
$\kappa_{0,SEI}$ [S/m]	3·10^{-5}	a
$\kappa_{SEI}(c_{Mn,dep})$ [S/m]	3·10^{-5}-1·10^{-6}	a
K	3·10^{-5}	a
ρ_{SEI} [kg/m^3]	2100	[19]
M_{SEI} [kg/mol]	0.073	[19]
$d_{0,SEI}$ [nm]	3	a [61, 95]
$D_{e^-,SEI}$ [m^2/s]	1·10^{-19}	a [20]
D_{H^+} [m^2/s)	10·10^{-11}	[32]
$D_{Mn^{2+}}$ [m^2/s]	5·10^{-11}	[32]
$k_{Mn,dissolution}$ [m/s]	5·10^{-7}	a
$k_{Mn,dep}$ [m/s]	8·10^{-11}	a
k_{iso}	1250·($i_{loc}/i_{1C,loc,pos}$)	a
$f_{Mn,dissolution}$	0.4	a
f_{H^+}	0.5	a
$\alpha_{a,Ox/c,SEI}$	0.5	[32]
$V_{m,pos}$ [m^3/mol]	8.3·10^{-5}	c

5.4 Model Validation

5.4.1 Performance Validation

The parameterised dynamic battery model was compared with experimental data to visualise the difference in ICA and charge/discharge curves with C/10 and 1C (Figure 5.5). At C/10 (Figure 5.5a and 5.5b) the model can recreate the the potential curve fairly well, however there are some differences between the model and measurement especially during charging. This it thought to be a result of lumping the two PE materials into one and not accounting for the hysteresis. The discrepancy seen in the charge peaks, a shift toward lower voltages, is assumed to be due to the hysteresis. The fact that the peak at 3.95V is lower than the expected could be a result of lumping the two PE materials into one. The discharge peaks show much better agreements overall.

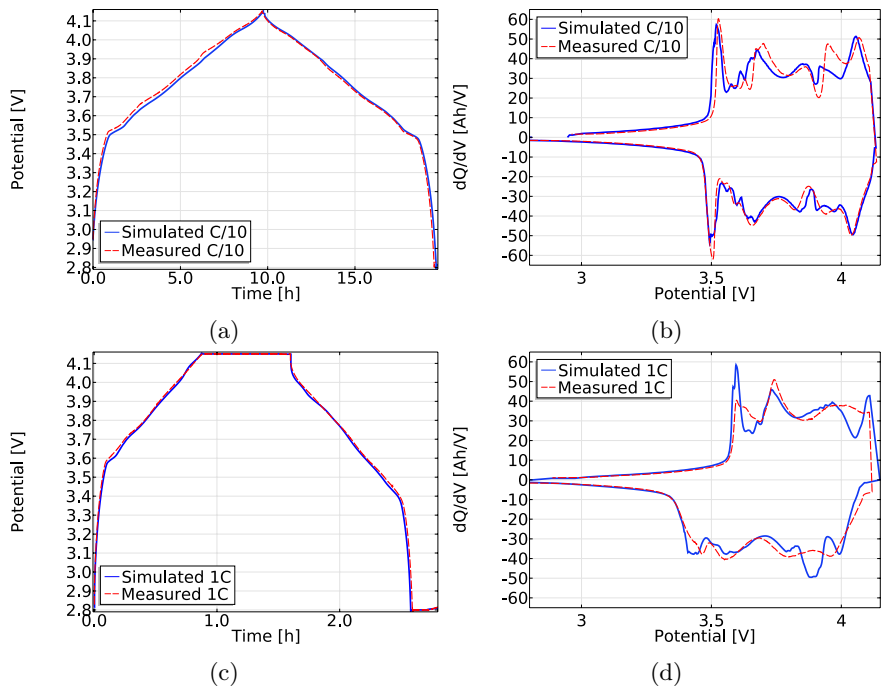

Figure 5.5: Charge/discharge cycle of a fresh cell at 25°C with (a) C/10 and (c) 1C and the ICA from the respective cycle at (b) C/10 and (d) 1C in comparison to simulated results.

For the 1C simulation (Figure 5.5c and 5.5d) an additional error is introduced by the diffusion coefficients. As previously mentioned, the method used for the optimisation of the diffusion coefficient needs to be further developed. The uncertainty in the PE diffusion coefficient is rather high and using literature values for the NE is not optimal. This is seen in the ICA as a rather poor agreement with the measurement data. The large peak in the NE diffusion coefficient at 50% SOL (Figure 5.2a) introduces a large additional peak at 3.9V for the discharge.

The voltage response for charge and discharge pulses with 1C and 5C at 90%, 50% and 10% SOC were simulated. The model can capture the discharge pulse response well, however at 10% SOC, the model has some difficulties (Figure 5.6). For the charge pulses, the discrepancies in the voltage response is slightly larger at 50% SOC and best at 90% SOC.

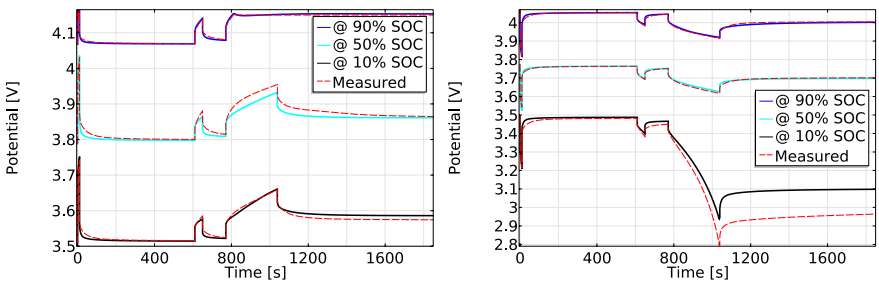

Figure 5.6: Simulated voltage response at different SOC levels for (a) charge and (b) discharge pules, compared to measured voltage response of a fresh cell tested at 25°C.

5.4.2 Ageing Validation

The ageing parameters were tuned based on the ageing trajectory in the test performed at 25°C with +2C/-2C in 60-70% SOC (cell #9) and the results from the ESMLE. In the ESMLE the PE material loss was found to be 8% over 88000 test cycles (7500 FCE). The results from the simulation (Figure 5.7) where the PE material loss and the resistance increase are in line with the calculated and measured values. The capacity degradation curve can however not be fully captured. Initially the degradation is in good agreement, although the larger capacity degradation followed by the very moderate ageing is not.

The SEI thickness is almost 4 times larger than the thickness seen in the PM results, but there is a possibility that the outer part of the SEI was rinsed away in the preparation process of the sample for the PM analysis and therefore is thicker than the measured value. Other reasons could be that using the density of the lithium carbonate for the SEI might not be a good approximation, or that the SEI is partially dissolved, broken down or reversible. Even with this large SEI growth the loss of electrolyte volume fraction in the NE is small, not likely to contribute notably to the resistance increase.

When simulating the degradation with +1C/-2C in 10-90% SOC cycles (cell #18) the initial capacity retention is in good agreement, but again the last part of the ageing trajectory cannot be fully captured (Figure 5.8). The resistance increase is much lower than measured and this is likely the reason for the discrepancy in the capacity retention. Increasing the SEI resistance further in the model would result in too high resistance for the 60-70% simulation case. The PE material loss is 13%, no slippage analysis was performed for this test cell, however this seems to be in a reasonable range when compared to cell #52 (+1C/-2C in 10-90% SOC at 45°C) that had 17.6% PE material loss.

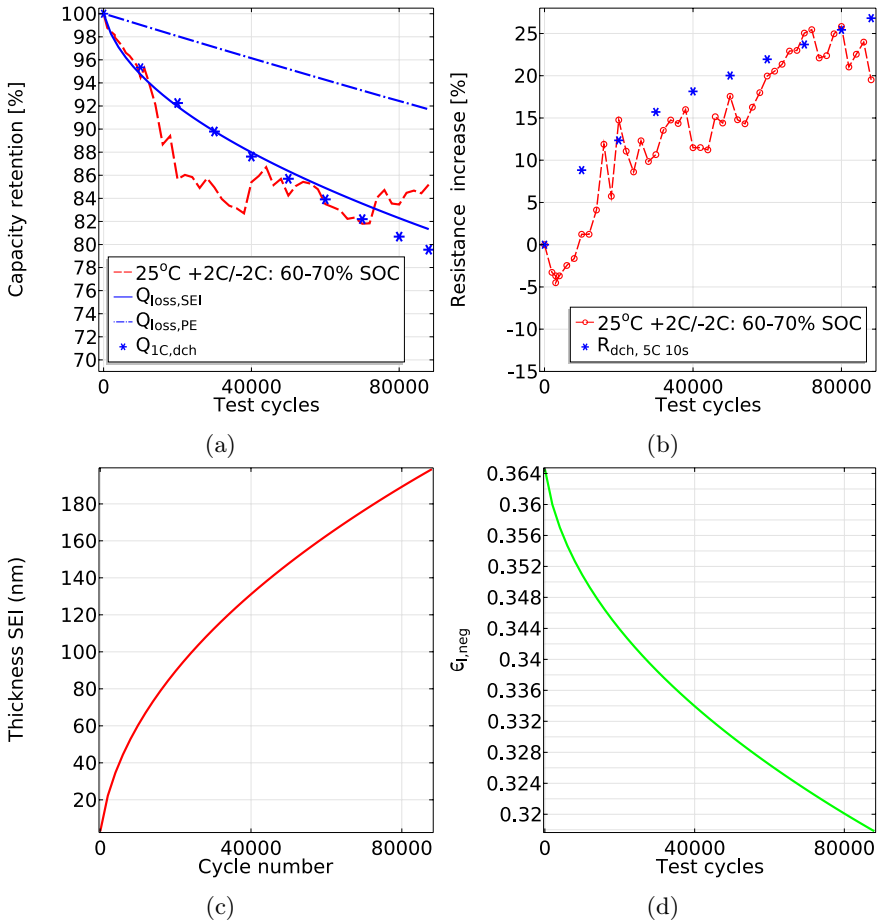

Figure 5.7: Simulated +2C/-2C 60-70% SOC cycles compared to measurement data (red - - and -o-) tested at 25°C (a) 1C discharge capacity and (b) 5C 10s discharge pulse resistance, (c) the resulting SEI thickness and (d) loss of electrolyte volume.

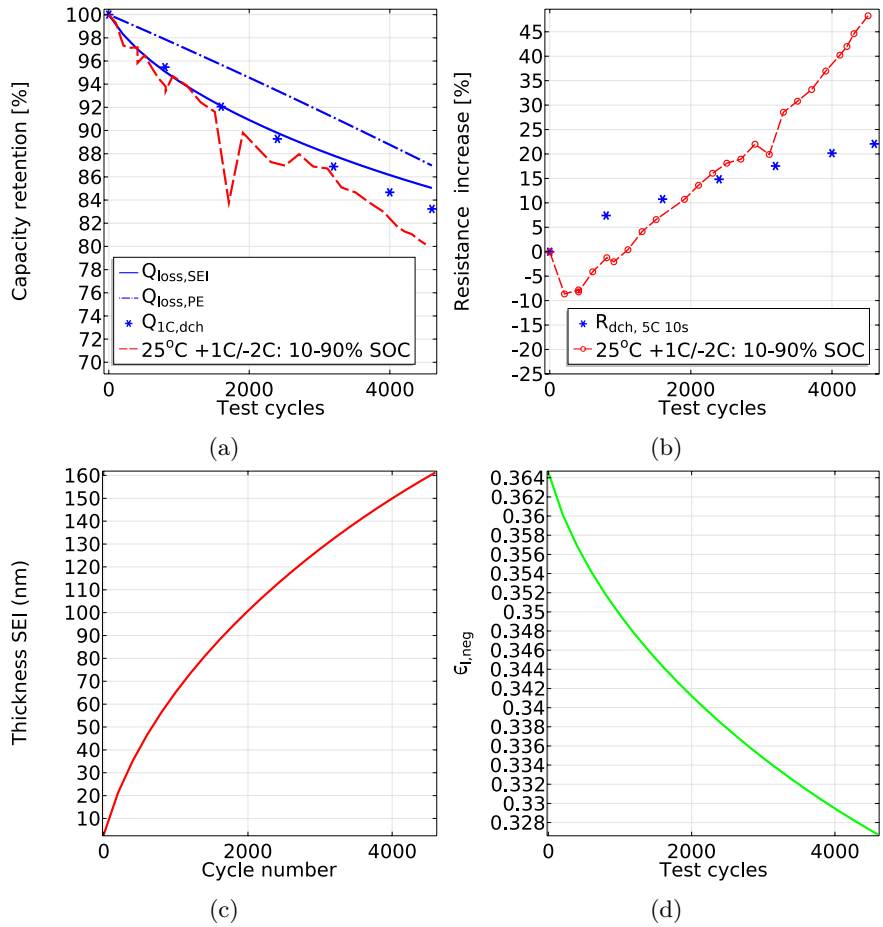

Figure 5.8: Simulated +1C/-2C 10-90% SOC cycles compared to measurement data (red - - and -o-) tested at 25°C (a) 1C discharge capacity and (b) 5C 10s discharge pulse resistance, (c) the resulting SEI thickness and (d) loss of electrolyte volume.

Chapter 6

Results and Discussion

In this chapter the combined results from the lifetime, calendar and cycling, tests are presented. A summary of all the test results and selected data to display the effect of temperature, C-rate, DOD and SOC is included. This is followed by the use of the lifetime test results in the empirical model and the model results of how drive and charge behaviour influences the battery lifetime in a vehicle.

The key results from a supporting PM analysis is included. In combination with ICA, as well as the developed ESMLE model, it gives some indications on the processes occurring in the tested cells. The combined results from the lifetime tests and ageing analysis are then compared to the P2D ageing model, where the contribution from each ageing mechanism is made visible.

6.1 Calendar Ageing

The calendar testing was performed over two years in three temperatures and at three SOC levels. The results (Figure 6.1) are in line with previous published literature [22, 25], where higher temperature and higher SOC increases the ageing. At low SOC, 15%, the temperature effects are moderate and there is only a slight difference between the three temperatures. As the SOC is increased, the temperature contribution is more pronounced. Interesting to note is that 75% SOC is more detrimental compared to 90% SOC at 35 and 45° C. However, in 25°C there is no difference. Previous studies have presented similar results [113, 114]. Keil et al. [113] showed that NMC cells at 100% SOC followed by 80% SOC had the fastest degradation and a local minimum at 95% SOC. The cause for this is not known, however Keil

et al. [113] showed that the calendar ageing could be linked to the different phases in the graphite. They could show that a higher lithiation degree in graphite and above the phase transition at 50% lithiation (peak 2 in Figure 3.2a) increased the ageing.

The resistance increase is very small in 25 and 35°C with large fluctuations, only in 45°C a clear effect can be seen. The resistance increase mirrors the capacity loss, higher temperature and higher SOC results in higher resistance.

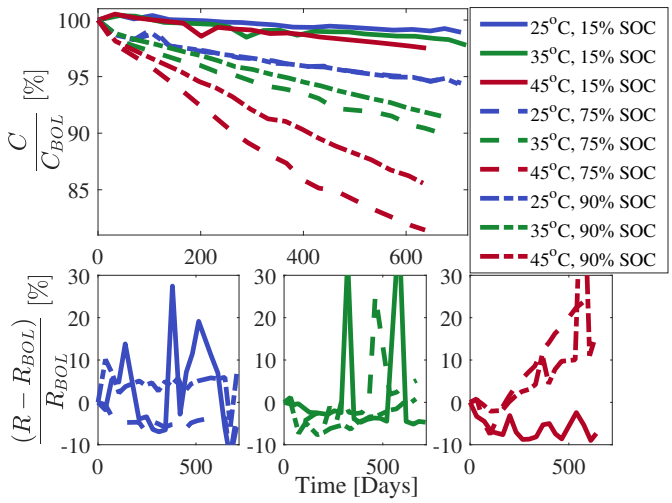

Figure 6.1: Remaining capacity and resistance increase from calendar tests at 25, 35 and 45°C and at 15, 75 and 90% SOC. The results at 25°C at 75% SOC is overlapped by those at 90% SOC.

6.2 Cycling Ageing

The cycling ageing tests were conducted during 4 years and the test matrix was designed to study the ageing dependence on temperature, C-rate, DOD and SOC. The overall results and the labeling of the cells are visualised in Figure 6.2. Each bar represents a cell tested according to the bar description, and the y-axis shows the number of FCEs. The bar colour indicates the remaining capacity of the cell, where the green colour shows the number of FCE with a capacity larger than 95%, yellow a capacity between 95-90%, orange a capacity between 90-85%, red a capacity between 85-80%, and black a capacity <80%. The temperature is indicated by the colour of the outer line of the bar; blue for 25°C, green for 35°C, and red for 40-45°C. The

cells tested with a CV step during charging is indicated by CV. The CV was performed at the corresponding voltage level of the upper SOC level, except in the cases marked with *, where a CV step at 4.15 V (100% SOC) were used.

The established knowledge for ageing in LiBs is that the upper and lower SOC levels are more detrimental for the cell. However, in this work the tested cells have shown a remarkable durability at low SOC and even at 0-10% SOC.

There is a large variation in how many cycles each cell has been tested, due to a limited number of channels where the tests had to be started in batches; when one cell reached the EOL criterion, 80% remaining capacity, it was stopped and a new cell started. The cells started in the first batch and tested in less detrimental test regimes could therefore reach an impressive number of FCEs. It can also be seen that a number of cells were stopped before reaching the EOL criteria, due to for example time limitations, or faulty equipment.

In order to manage the large test matrix, with the available test channels, the number of duplicates had to be limited. The duplicates showed good agreement with one another, except for cells #43 and 44, and #46 and 47. This is thought to be due to a move of the test equipment, where cells #44 and 47 had a longer pause in the testing, while cells #43 and 46 did not.

As some of the cells were tested more than 2 years, pauses in the testing were inevitable. The test equipment was calibrated on a regular basis, and there were also a number of unscheduled stops. Every time a test had to be paused, an RPT was made, before and after the test being resumed. The cells did often recover or lose capacity during these pauses, reflected in the capacity degradation curves as a vertical drop or gain.

The tests in small DODs showed large fluctuations in the measured capacity during the ageing. The reason for this has not been established. It was first thought to be a problem with the accuracy in the current control during the CV charge step. However, after observing the same behaviour in all cells tested in 10% DOD, regardless of test equipment used, the accuracy in the current control was considered not to be the main cause of these fluctuations. A hypothesis is that the fluctuations are linked to processes such as temporary blocking of active material or other reversible processes.

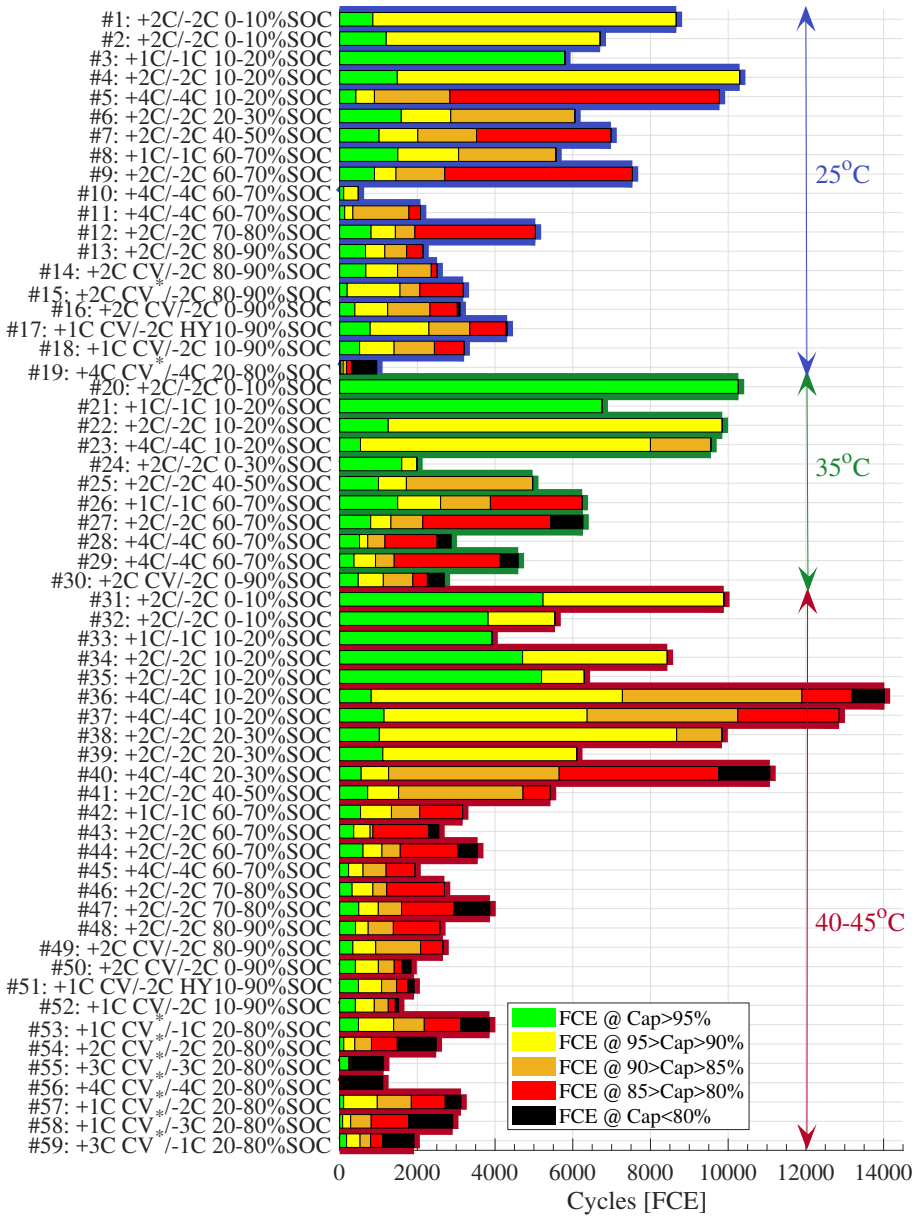

Figure 6.2: Cycling ageing for all cells tested at 25, 35 and 40-45°C. The green bars show the number of FCE with a capacity larger than 95%, yellow a capacity between 95-90%, orange a capacity between 90-85%, red a capacity between 85-80%, and black a capacity <80%. The CV step was performed at the corresponding voltage level of the upper SOC level except in the cases marked with *, where a CV step at 4.15 V (100% SOC) were used.

6.2.1 Effect of Temperature

The expected temperature dependence, i.e increased ageing at higher temperatures, was seen for large DODs (Figure 6.3). However, this was not always the case for small DODs. Four different SOC levels with 10% DODs were tested at all three temperatures, and for 25 and 45°C two additional SOC levels were tested.

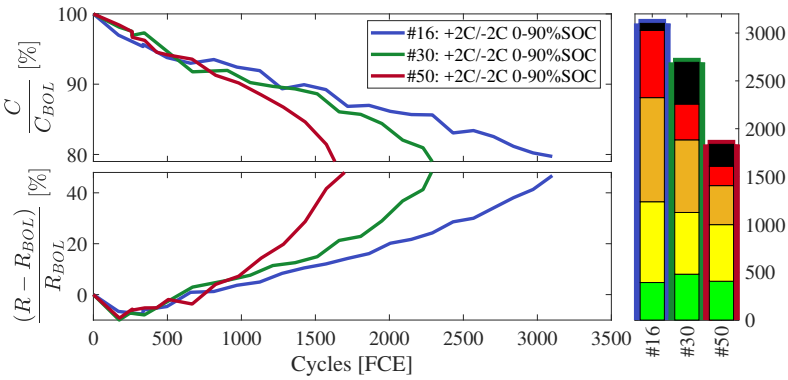

Figure 6.3: Cycling ageing with +2C/-2C in 90% DOD at 25, 35 and 45°C.

For the 10% DOD tested in a SOC level lower than 50% SOC, the expected increased capacity degradation at higher temperatures could not be seen (Figure 6.4). Instead, the cells tested at 25°C showed slightly more degradation compared to the two higher temperatures. The 35°C cells had the best performance closely followed by the cells tested in 45°C.

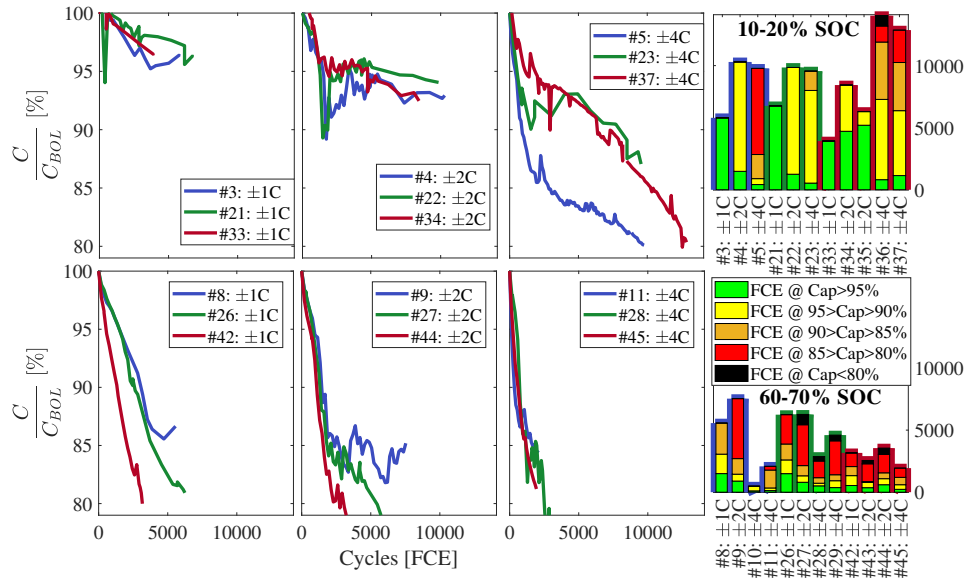

Figure 6.4: Cycling ageing in 10% DOD at 10-20% (top) and 60-70% (bottom) with +1C/-1C (left), +2C/-2C (middle), and +4C/-4C (right) at 25, 35 and 45°C.

6.2.2 Effect of C-rate

The expected C-rate dependency, increased ageing for higher C-rate, was observed (Figure 6.5). With a large DOD, the ageing in the cell tested with +1C/-2C was only slightly faster compared to the cell tested with +1C/-1C, while the cell tested with +1C/-3C showed a rapid increase in ageing. Clearly showing a nonlinear relation in ageing with C-rate. The reason for the larger increase in ageing between 2C and 3C is considered to be that CC with 3C is resulting in larger concentration gradients in the electrodes leading to larger stress in the active material. The higher C-rate could also give a slight increase in temperature.

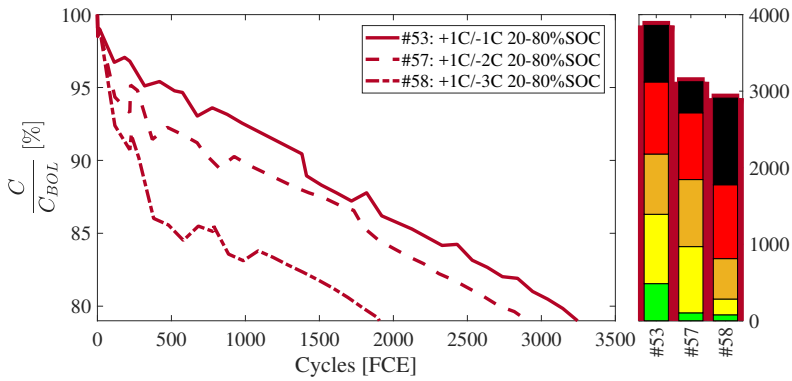

Figure 6.5: Cycling ageing for different discharge rates, +1C/-XC in 60% DOD at 40°C.

For the small DODs, the same trend could be observed (Figure 6.4), however, the difference in 1C and 2C were even smaller. Surprisingly, 4C was not as detrimental as expected in the 10-20% interval. Interestingly, the cell tested at 25°C showed faster ageing compared to the cells tested at 35 and 45°C. This was again thought to be due to larger material stress, since at 25°C the resistance is higher and the kinetics slower compared to the higher temperatures. A similar trend, although not as clear, could be seen for the cells tested in 60-70% SOC. Where the increased ageing with temperature is only seen at 1C and 2C, and the difference reduces with increased C-rate.

6.2.3 Effect of DOD

An important observation was that the ageing trend looks differently for the large DODs and the 10% DODs. For large DODs, the cells initially lose capacity fast during the first hundred cycles, then the degradation pace slows down to a linear trend, before finally accelerating again (Figure 6.3).

The 10% DODs have the same initial fast degradation step followed by a linear degradation, but which is much slower for the lower SOC levels and has approximately the same speed for the higher SOC levels (Figure 6.6). However, instead of going into the accelerated "final" ageing step, the ageing levels out at a distinct level that seems to be related to SOC, C-rate and temperature.

The reason for the different degradation trends is unknown. A speculation is that the 90% DOD results in a larger expansion in the graphite compared to the 10% DODs. The larger expansion causes the SEI to crack and expose fresh graphite for the SEI reactions that eventually consumes all the additives leading to a more unstable SEI to form, which accelerates the degradation.

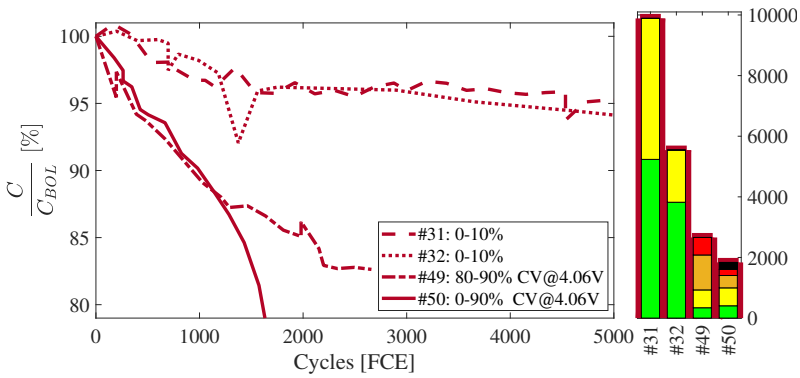

Figure 6.6: Cycling ageing with +2C/-2C in 10% DOD at 0-10% and 80-90% SOC compared to 0-90% SOC at 45°C.

6.2.4 Effect of SOC Level

A further interesting observations from the 10% DODs study is the clear difference between cells tested at higher SOC levels, which have a faster degradation compared to cells tested below 40% SOC (Figure 6.7). Three distinct ageing groups could be seen in the trends for the cells tested at 45°C (Figure 6.8) and only two for the cells tested at 25 °C (Figure 6.10a). This indicates that there is one or several ageing mechanisms that have an accelerated process for higher SOC levels and higher temperatures.

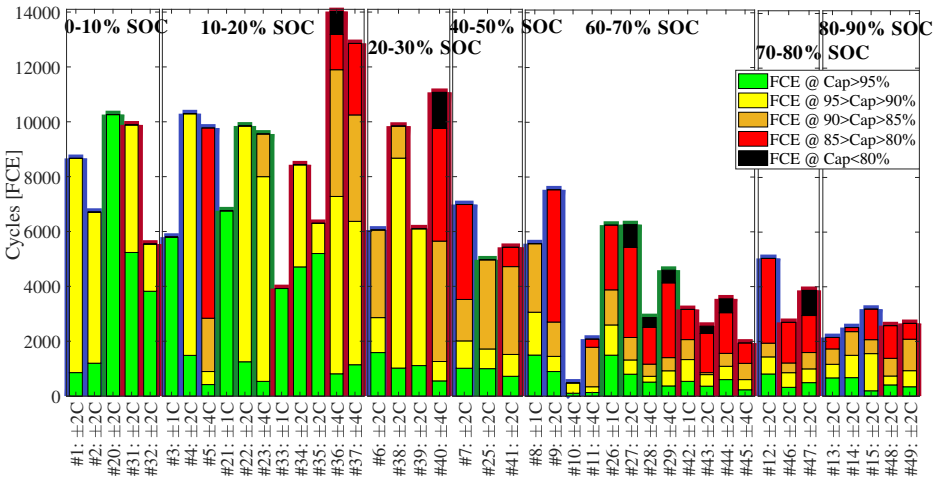

Figure 6.7: Cycling ageing in 10% DODs at different SOC levels and different C-rates at 25, 35 and 45°C.

The ageing at 25°C is similar and moderate with increased SOC level, for all cells above 40% SOC, indicating that this is the approximate start level for an accelerated ageing. At 45°C the separation between the 40-50% SOC results and the ones above 60% SOC shows that there is a clear temperature dependency related to this ageing mechanism.

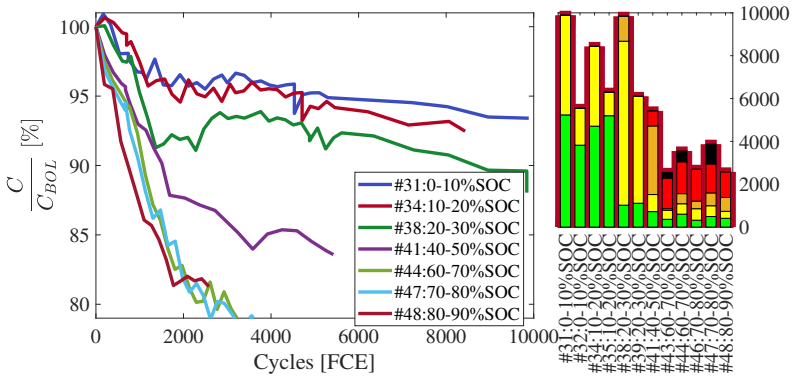

Figure 6.8: Cycling ageing in 10% DODs at different SOC levels with +2C/-2C at 45°C where three distinct ageing groups can be observed.

6.2.5 Constant vs Dynamic Current

Tests were performed to compare the synthetic constant current (CC) cycles with a more realistic dynamic drive cycle. The Hyzem drive cycle (Figure 3.8) was chosen for this purpose and the RMS current was scaled to 2C.

It seems that at least the tested dynamic current is less detrimental for the cell compared to a CC (Figure 6.9). The test with 1C charge and CC 2C discharge ages faster compared to the cells tested with the Hyzem drive cycle with a 2C RMS current. Even if the current for shorter duration's are higher than 2C, the cell seems to be less stressed compared to the 2C CC operation. Needed to be noted is that the Hyzem drive cycle also includes short pauses and the drive cycle therefore takes longer time than the CC cycle. Although not fully understood, this is a potentially encouraging result for a vehicle application.

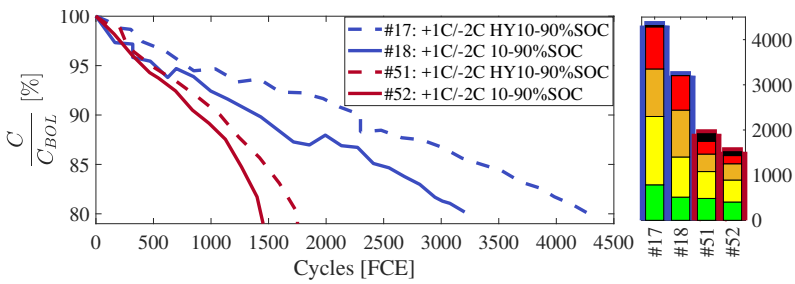

Figure 6.9: Cycling ageing in 10-90% SOC at 25 and 45°C with 1C charge and discharge with 2C CC or Hyzem drive cycle with a 2C RMS current.

6.3 Empirical Ageing Model

An empirical ageing model was developed based on the tests conducted in the 10% intervals. A short description of the model will follow here, a more detailed description and results from the empirical model can be found in [115].

The model is based on the CC charge and discharge test in the 10% DOD tests at 25 and 35°C. The capacity retention is described with a two exponential function derived for each 10% interval according to

$$\text{Cap}(\text{SOC}, \text{FCE}, T, \text{C-rate}) = a \cdot \exp(b \cdot \text{FCE}) + c \cdot \exp(d \cdot \text{FCE}) \tag{6.1}$$

where a is function of SOC (6.2), $c = 26 - a$, b is a function of both SOC and C-rate (6.3), and d is a look-up table including SOC, C-rate and temperature (Table 6.1).

$$a(\text{SOC}) = 6.2\frac{\text{SOC}}{90} + 0.093 \tag{6.2}$$

$$\begin{aligned} b(\text{SOC}, \text{C-rate}) = &\left(0.98\left(\frac{\text{C-rate}}{2}\right)^{3.3} + 0.0174\left(\frac{\text{SOC}}{20}\right)\right) \cdot \\ &\left(\frac{-0.6045}{\text{SOC}^{2.4}} - 5.512 \cdot 10^{-4}\right) \cdot \left(\frac{\text{SOC}}{20}\right)^{(0.05\text{C-rate}^3 - 0.35\text{C-rate}^2 + 1)} \end{aligned} \tag{6.3}$$

Table 6.1: Look-up table for SOC and temperature dependency for parameter d. A linear extrapolation was used for the SOC values when there were no experimental data.

SOC interval [%]	**0-10**	**10-20**	**20-30**	**30-40**	**40-50**	**50-60**	**60-70**	**70-80**	**80-90**
$d(25°C, 2C) =$	[-6.620	-3.210	-2.410	-3.700	-5.000	-2.550	-0.100	-0.010	-0.001]$\cdot 10^{-6}$
$d(35°C, 2C) =$	[-3.042	-1.000	-0.400	-4.730	-9.000	-7.67	-6.331	-7.000	-0.7]$\cdot 10^{-6}$

For the d parameter a linear extrapolation was used for the SOC values where there were no experimental data (30-40% and 50-60% SOC). The following relations were used to account for the C-rate dependence for d,

$$\begin{aligned} d(\text{C-rate} \leq 1, \text{SOC} < 50) =& d(2C, \text{SOC}) + (\text{C-rate} - 1)\,(d(2C, \text{10-20}) - d(1C, \text{10-20})) \\ d(\text{C-rate} \leq 1, \text{SOC} \geq 50) =& d(2C, \text{SOC}) + (\text{C-rate} - 1)\,(d(2C, \text{60-70}) - d(1C, \text{60-70})) \\ d(\text{C-rate} \leq 2, \text{SOC} < 50) =& d(2C, \text{SOC}) + (2 - \text{C-rate})\,(d(2C, \text{10-20}) - d(1C, \text{10-20})) \\ d(\text{C-rate} \leq 2, \text{SOC} \geq 50) =& d(2C, \text{SOC}) + (2 - \text{C-rate})\,(d(2C, \text{60-70}) - d(1C, \text{60-70})) \\ d(\text{C-rate} > 2, \text{SOC} < 50) =& d(2C, \text{SOC}) + \frac{\text{C-rate} - 2}{2}\,(d(2C, \text{10-20}) - d(4C, \text{10-20})) \\ d(\text{C-rate} > 2, \text{SOC} \geq 50) =& d(2C, \text{SOC}) + \frac{\text{C-rate} - 2}{2}\,(d(2C, \text{60-70}) - d(4C, \text{60-70})) \end{aligned} \tag{6.4}$$

For the calendar ageing, (6.1) was fitted to results from storage tests at 15%, (6.5), and 90% SOC, (6.6), at 25°C. The model compared to the test data at 25°C and 35°C for different SOC levels, C-rates, and the calendar ageing are visualised in Figure 6.10.

$$\begin{aligned}\text{Cap}_{cal}(15\%, \text{Days}, 25°C) = {} & 0.0743 \cdot \exp(-9.545 \cdot 10^{-3} \cdot \text{Days}) \\ & + (26 - 0.0743) \cdot \exp(-1.9 \cdot 10^{-5} \cdot \text{Days}) \end{aligned} \quad (6.5)$$

$$\begin{aligned}\text{Cap}_{cal}(90\%, \text{Days}, 25°C) = {} & 0.29 \cdot \exp(-0.0417 \cdot \text{Days}) \\ & + (25.843 - 0.29) \cdot \exp(-6.153 \cdot 10^{-5} \cdot \text{Days}) \end{aligned} \quad (6.6)$$

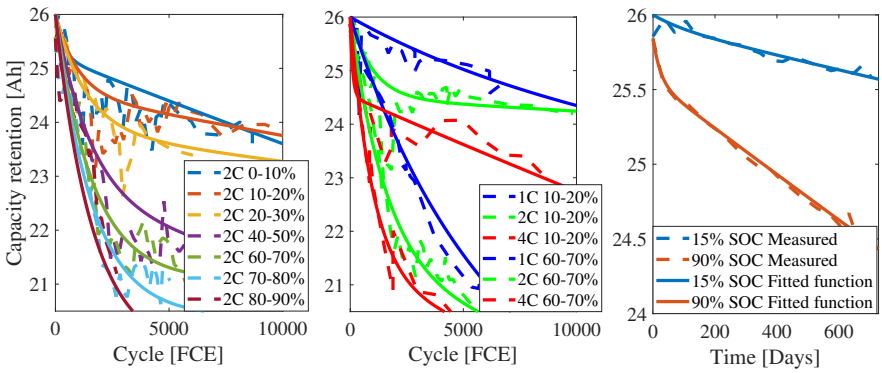

(a) (b) (c)

Figure 6.10: Parameterised ageing functions together with input data for (a) 2C data at 25°C, (b) different C-rates at 35°C, and (c) calendar ageing at 25°C at 15% and 90% SOC.

For DOD larger then 10% the contribution for each interval was added to estimate the contribution for the targeted DOD. Test data at 35°C in a 30% DOD, 0-30% SOC, was used to verify the model (Figure 6.11).

A case study for cycling ageing was performed and the model showed that there is a large potential in prolonging the battery lifetime by avoiding high SOC levels. By using a small DOD at a low SOC levels the cycle-life could be substantially prolonged, up to 130% for one of the test cases.

Also cases were studied where calendar ageing was included, at high and low SOC, 90% and 15%, respectively. The capacity losses were weighed together according to the number of FCEs driven per day and the time for calendar ageing per day according to

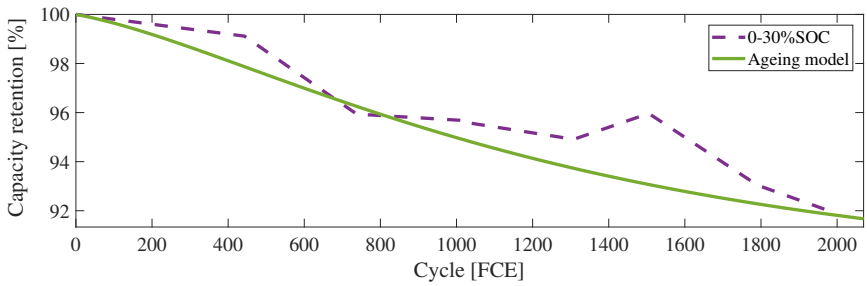

Figure 6.11: Capacity degradation in 0-30% SOC with 2C charge and discharge for the ageing function together with experimental data at 35°C.

$$\text{Cap(Cyc,Cal)=Cap(FCE/day)} + w_{t,cal} \cdot \text{Cap}_{cal}(\text{SOC}, \text{Days}, 25°C) \quad (6.7)$$

The results were as expected, i.e. the calendar ageing is a large contributor to the ageing for a personal vehicle that is spending most of its time parked, 96.5% of its time [116]. In [115] an example is shown that by adapting a charging strategy, i.e. planning the charging to avoid high SOC, the contribution from calendar ageing could be reduced from 61% to 35% for vehicle 1, prolonging the lifetime from 6 to 11 years.

6.4 Ageing Analysis

6.4.1 Post Mortem Analysis

A selected number of cells were opened to perform PM analysis. In table 3.2 the selected cells are marked with PM. The PM analyses were conducted by Erik Björklund at UU and this section is only presenting the most significant results used as guidance in the development of the P2D ageing model. The detailed PM analysis can be found in [117, 118]. The cells were discharged to 0% SOC, 2.8V, before they were disassembled in an argon filled glovebox.

To study the impact of SOC, PM analysis were conducted on two cells, cycled in different SOC intervals, +2C/-2C 10-20% SOC and 60-70% SOC at 45° C, and compared to a fresh cell presented in [78]. The cycled NEs had higher resistances compared to the uncycled NE, where the NE from the cell cycled at 60-70% SOC had the highest resistance. The SEI layer of the cycled cells, compared to the uncycled, were thicker and between 20 and 50 nm. For both cycled cells, Mn could be found in the SEI, however, the amount of Mn was much higher for the cell cycled at 60-70% SOC. The PE suffered from

loss of active material, especially the NMC particles. Again the ageing was more severe at the higher SOC level.

The observation that the Mn dissolution has a slower rate at low SOC levels was confirmed when studying a cell cycled in 10-20% SOC with +4C/-4C until 80% capacity retention. Only small amounts of Mn was found in the SEI, even though the cell had a similar end capacity as for the cell tested in 60-70% SOC.

An investigation of the temperature effect was conducted on cells tested in 0-90% SOC with +2C/-2C at 25°C and at 45°C. The higher temperature lead to an increased salt degradation and more products related to this, phosphorus and fluorine containing SEI species, could be found on the NE. Further, an investigation of two cells tested with different C-rates, 1C and 4C, in 60-70% SOC at 35°C showed that the higher C-rate also caused more salt degradation. It could also be seen that more carbonate formation occurred on the NE at a higher C-rate [117].

6.4.2 Electrode Slippage and Material Loss

For the cells not included in the PM analysis, a non-invasive method was used, ESMLE. The model developed by Björklund [117], shortly introduced in Section 2.2.2, was used to calculate the electrode slippage and material loss. For these cells, a charge and discharge cycle with C/10 was conducted after the ageing cycling was finished. For one cell, #52 (+1C/-2C 10-90% SOC at 45°C), the C/10 cycle was performed at every RPT.

The result for cell #52 can be seen in Figure 6.12. The electrode slippage was 10x larger for the NE than for the PE. The continuous shifting to the left of the NE potential curve indicates that there are reduction side reactions. A likely cause is the continuous decomposition of solvent and other electrolyte components resulting in SEI growth on the NE. As the PE has a much smaller slippage it is difficult to draw any clear conclusions. The slippage of the PE could also be an artefact as a result of the material loss and was not included in the analysis.

For the NE, the model calculated only a small material loss, in good agreement with the results from the PM analysis [78]. The large material loss seen in the PM analysis was also seen in the calculated results for the PE.

For 16 additional cells it was possible to conduct this analysis at the end of the testing (Figure 6.13). The cells had reached different capacity retention at the time for the analysis, and this has to be kept in mind, making the analysis more complex. However, all cells tested below 30% SOC had a capacity over 90%, except cell #23 (+4C/-4C 10-20% SOC at 35°C) and #38 (+2C/-2C 20-30% SOC at 45°C). Looking at cell #2, #20 and #31 (+2C/-2C 0-10%

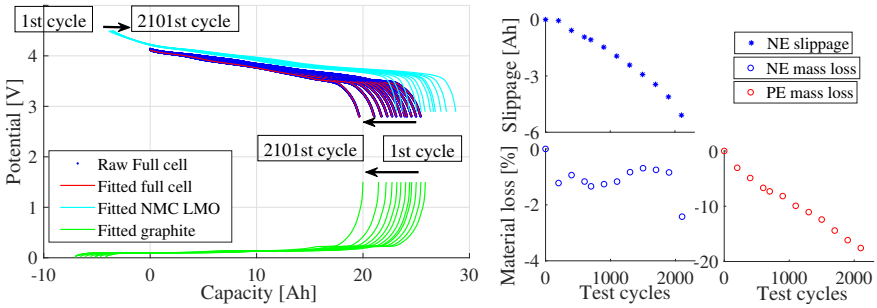

(a) (b)

Figure 6.12: (a) Calculated potential curves from half cell electrode potentials, for cell #52 (+1C/-2C 10-90% SOC at 45°C) from C/10 cycles throughout the test-period. (b) The calculated slippage and material loss for each electrode.

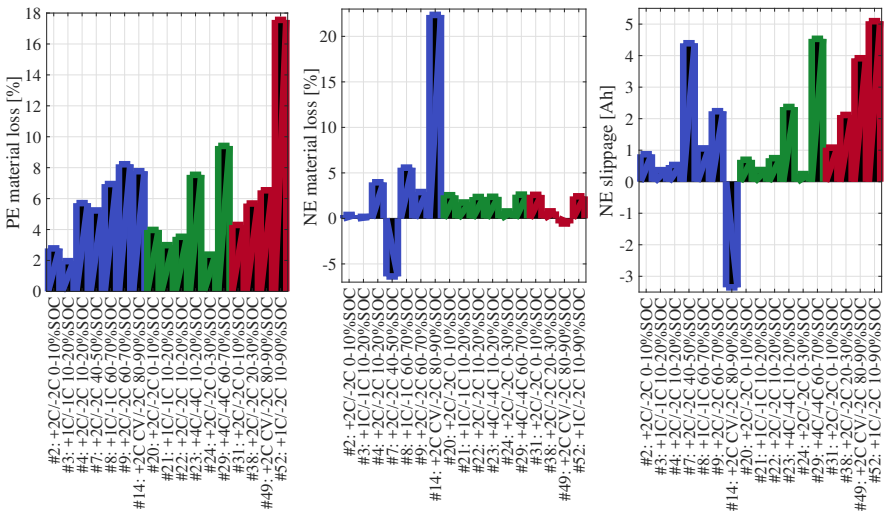

(a) (b) (c)

Figure 6.13: Calculated material loss in the (a) PE and (b) NE for 17 of the tested cells and (c) the slippage of the NE.

SOC at 25, 35 and 45°C) the PE material loss is increasing with increasing temperature. The same trend can be seen for an increasing SOC, where the cells tested in 25°C at higher SOC experience larger loss of active material. Increasing C-rate also seems to generate a larger loss of PE material, and

increasing slippage of the NE. The material loss of the NE is modest for all cells, except for cell #14 (+2C/-2C 80-90% SOC at 25°C) which shows inconclusive results.

6.4.3 Incremental Capacity Analysis

ICA is the basis of the ESMLE, studying the ICA further more information that is not included in the ESMLE can be extracted. If the cell only suffer from increased resistance, the ICA should look the same as for the fresh cell though shifted to the right for the charge and left for the discharge. If both electrodes experience the same amount of material loss the ICA should look the same though with a reduced peak amplitude. If only one electrode experiences material loss the peaks related to that material will loose amplitude, but the balance between the electrodes will also be shifted and the peak positions will shift. If there is side reactions the electrodes slips in relation to one another resulting in shifting of the peaks. The the change of peak positions can also reduce peak amplitude. Any change in the electrode balance will bee seen in the ICA.

For cell #52 (+1C/-2C 10-90% SOC at 45°C), that had C/10 measurements throughout the test period, an ICA analysis was made (Figure 6.14). The contribution from the cell polarisation and the increase with number of cycles is easiest seen at the initiation of the charge and discharge where the voltage drops as the current load is applied. As can be seen for cell #52 there is more than polarisation increase taking place. Recall Figure 3.4 and the different materials phase transitions. In support of the ESMLE, the cell experience large slippage of the electrodes. Initially the discharge peaks related to phase transitions for graphite are all below 3.82 V (Peaks 1(5) to 2(2) in Figure 3.4), at the last measured ICA the 2(2) is close to 3.9 V. This shows a large slippage where side reactions and loss of cyclable Li^+ seem to be the dominating ageing mechanism. Furthermore, the peaks below 3.7 V are losing more amplitude than the peaks above 3.7 V indicating loss of active material. With the large slippage of the electrodes it is though difficult to establish if there is material loss. However, the ESMLE support this assumption and as these peaks are related to the NMC this indicates that the largest material loss is due to NMC. This is also in good correlation to previous research showing that the NMC material experience material loss that has been linked to particle cracking and surface changes [54, 67].

ICA was made for three of the cells tested with 2C in 10% DOD in 25°C at different SOC levels (Figure 6.15a). In the previous section it could be seen that cell #4 (+2C/-2C 10-20% SOC at 25°C) had a rather high loss of material, but maintains a high cell capacity of 92.9%. As the active material loss is similar in both electrodes, 5.7 and 4%, and only has a minor slippage

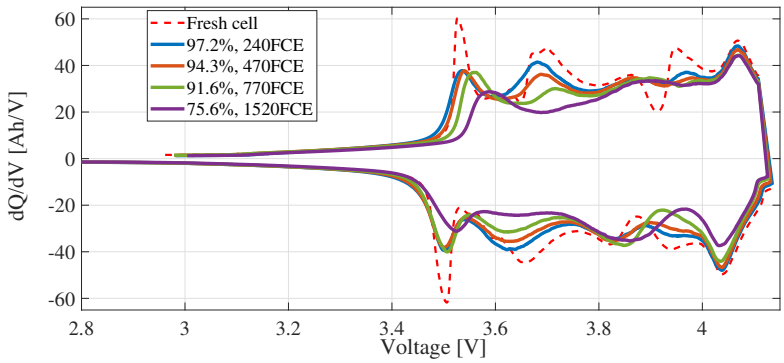

Figure 6.14: ICA for cell #52 (+1C/-2C 10-90% SOC at 45°C) through out the test-period.

of the NE, the electrodes balance is maintained. However, for cell #9 (+2C/-2C 60-70% SOC at 25°C) there is an 8.2% loss of PE material and only a minor loss of NE material, with a 4x larger slippage of the NE, the remaining capacity is 85.2%. As the slippage of the electrodes is a consequence of side-reactions trapping Li^+, this proves that Li-loss is the largest cause for the capacity loss in the cells. Interesting to note is that the slippage in cell #9 is less than for cell #7 (+2C/-2C 40-50% SOC at 25°C), this can also be seen in the ICA where the peak initially around 3.5 V (Peak 1 5 in Figure 3.4) has shifted more for cell #7. The end capacities are similar, where cell #9 seems to have suffered slightly higher loss of PE while cell #7 has experienced more reduction reactions.

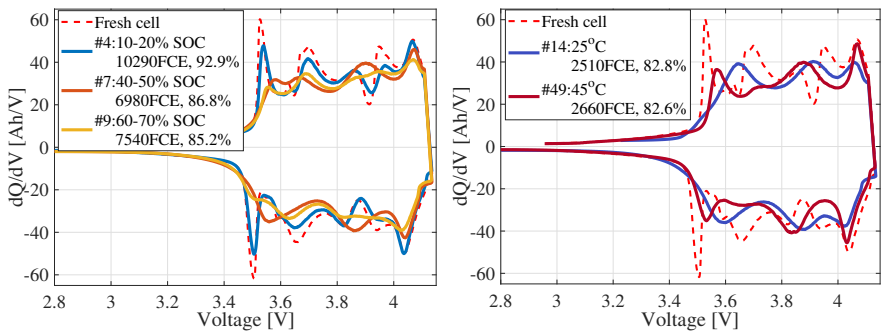

(a) (b)

Figure 6.15: ICA from C/10 cycles for cells tested with 2C (a) at 25°C in different 10% DODs and (b) at 25°C and 45°C in 80-90% SOC with CV at 90% SOC (4.06V).

Cells #14 (+2C/-2C 80-90% SOC at 25°C) and #49 (+2C/-2C 80-90% SOC at 45°C) reached almost the same end capacity (Figure 6.15b). However, the ICA shows clear differences. For cell #14 the ESMLE were inconclusive, the model made a poor fit to the measured ICA, which is understandable since the ICA shows large shifts and immersion of peaks. The large shift in the peak initially around 3.5 V indicates side reaction and the lower amplitude in the peaks at higher voltages indicates material loss. To fully answer what ageing cell #14 has experienced, further investigations are needed. For cell #49 the loss seems to be linked to side reactions but also loss of NMC material, the last peak related to LMO have maintained the amplitude. The large changes in the other peaks are likely due to the large slippage in the NE.

For the cells tested at 35°C in 10-20% SOC at different C-rates, the ESMLE showed that the PE material loss and the NE slippage increased with increasing C-rate (Figure 6.16a). The difference between 1C and 2C is moderate, although the test run with 4C showed a larger increase in PE material loss and NE slippage. This can also be seen in the ICA where the NE peaks have shifted toward higher potentials and the amplitude of most peaks have been reduced. As the LMO peak at 4.1 V maintain the amplitude again, it seems to be that NMC suffers most of the material loss. The loss of NE material is minor and in the same range for the three cells indicating that it is the NMC that is sensitive to the increased C-rate.

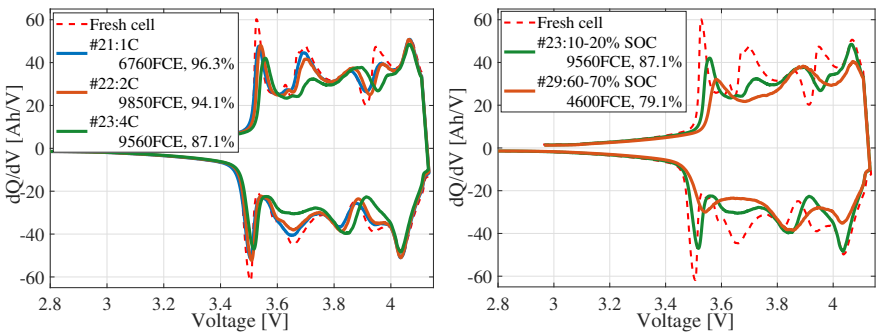

(a) (b)

Figure 6.16: ICA from C/10 cycles for four cells tested at 35°C (a) with different C-rates in 10-20% SOC and (b) with 4C in two different 10% DODs.

Running 4C at higher SOC, cell #29 (+4C/-4C 60-70% SOC at 35°C), seems to further amplify the ageing, with 2% larger PE material loss and almost twice the NE slippage in the ESMLE. This is also seen in the ICA where the peaks have been further shifted and the amplitude loss is more severe, even though the cell has only been tested for less then half the number of FCEs as that of cell #23 (+4C/-4C 10-20% SOC at 35°C) (Figure 6.16b).

6.5 Physics-Based Simulation Results

The ageing in this model is a result of the SEI layer growth, Mn dissolution, transport and deposition on the NE, and the Mn effect on the SEI properties. The growth of the SEI results in three different ageing contributions, consumption of cyclable Li^+, increased film resistance on the NE, and decreased volume fraction of electrolyte in the NE. The Mn dissolution results in loss of active PE material and increased resistance in the SEI due to reduced ionic conductivity in the SEI layer. The total resistance in the model is calculated from

$$R_{tot} = \frac{E_{cell} - \left(\int_L \frac{E_{eq,pos}(SOL_{pos,AV})}{L_{pos}} - \int_L \frac{E_{eq,neg}(SOL_{neg,AV})}{L_{neg}} \right)}{I_{cell}} \tag{6.8}$$

where E_{cell} is the cell potential during load with the current I_{cell}, and E_{eq} is the equilibrium potential for the average lithiation degree, SOL_{AV}, of the electrodes. The discharge resistance at 50% SOC has been used for the comparisons in the following sections.

6.5.1 The Time Factor Influence on Ageing

To reduce the required number of simulated cycles a time factor, t_{factor}, was introduced in the model. The time factor linearly extrapolate the ageing from one cycle to the next n cycles. The time factor is included in the side reaction currents, (4.37) and (4.42), to ensure that the slippage of the electrodes is accounted for. The impact of this time factor was investigated as well as how large it could be without introducing errors.

A test case of a +1C/-1C cycle in 0-100% SOC was used to ensure that the time factor would not effect the ageing (Figure 6.17). The results show that if the time factor is small enough, the error is negligible. At values higher than 100 a small error is introduced and the model underestimates the ageing. The error is increasing with higher values.

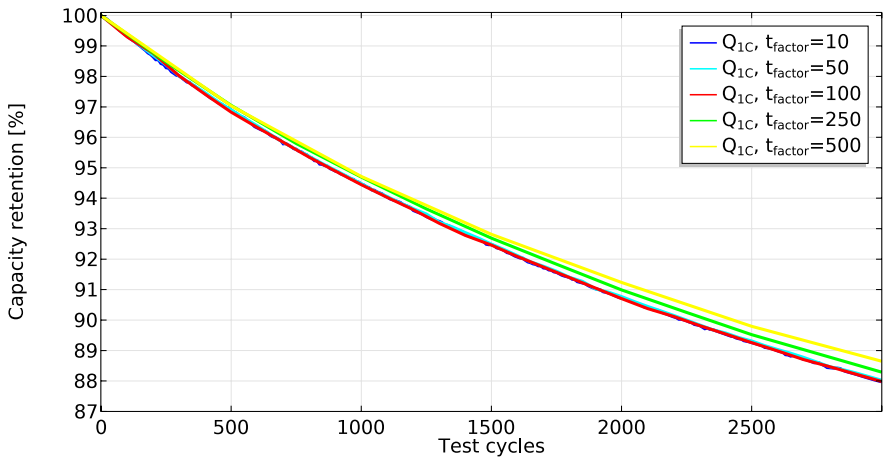

Figure 6.17: Impact of the time factor in the ageing model.

6.5.2 Consequences of SEI Build up

For this study the ageing was simulated for an example case using a CC-CV cycle with +1C/-1C at 25°C. For the example case the ageing parameters were enhanced slightly or significantly so that the contribution from the different mechanisms could be seen more clearly.

The SEI growth is the largest contributor to the ageing in the cell during normal use and consequentially also in the model. In this section the result of the SEI growth is visualised. The SEI growth results in a capacity loss due to trapped Li^+, but also an increase in the resistance that also can limit the capacity. Two cases are simulated, SEI growth with or without loss of electrolyte volume.

The capacity retention as result of the SEI growth, $Q_{loss,SEI}$, is the same in both cases (Figure 6.18). The SEI growth in the model resulting in loss of electrolyte volume in the NE, contributes to a resistance increase in the model, however, small enough to only give a minor decrease in the usable 1C capacity, $Q_{1C,dch}$, for this set of parameters (Figure 6.19). The loss of capacity is in both cases related to the loss of Li^+.

An additional case was included, SEI growth with loss of electrolyte volume, although now assuming a more resistive SEI. The SEI growth is slightly higher due to the larger overpotential at the NE as a result of the more resistive film. As the ageing progresses the resistance becomes higher and after 1200 cycles, where the curves intersects, becomes limiting for the capacity.

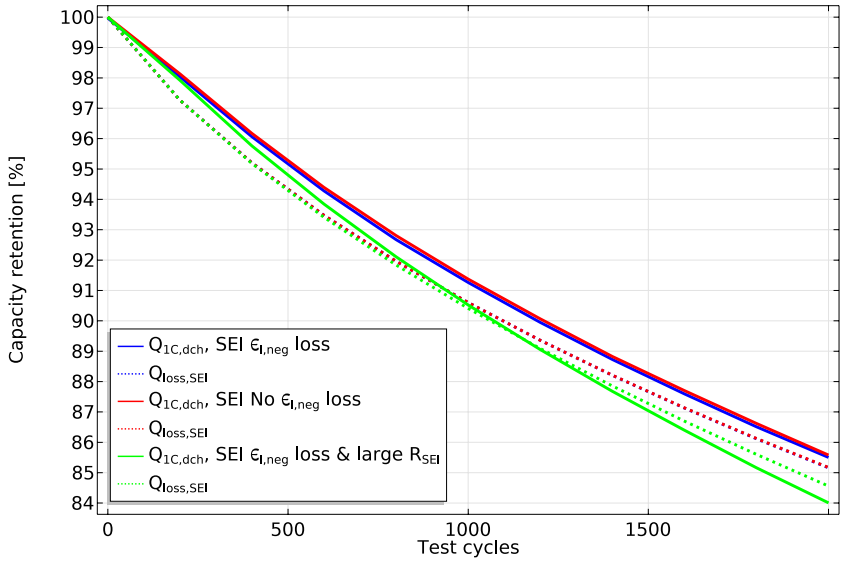

Figure 6.18: Simulated capacity retention for SEI growth with and without loss of electrolyte volume for simulated cycles with +1C/-1C in 0-100% SOC at 25°C.

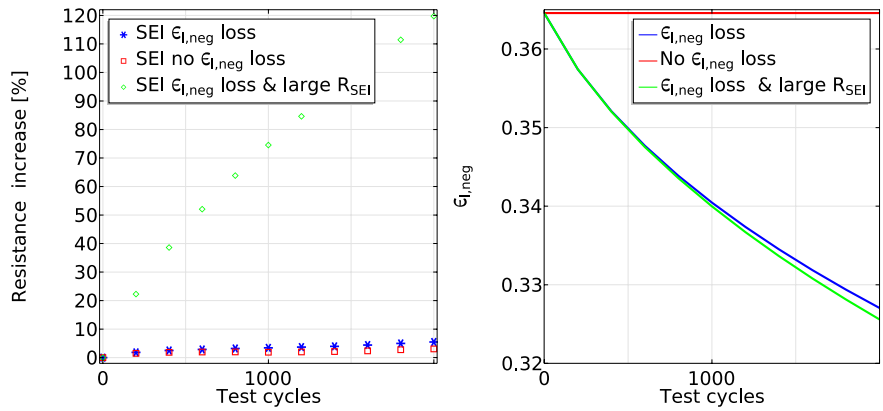

(a) (b)

Figure 6.19: Simulated ageing when only including SEI growth with and without loss of electrolyte volume for the +1C/-1C cycling in 0-100% SOC at 25°C. (a) The resulting cell discharge resistance increase at 50% SOC and (b) the change of volume fraction electrolyte in the NE for the three simulated cases.

6.5.3 Consequences of Mn Dissolution and Deposition on the NE

The oxidation on the conductive carbon at the PE results in loss of PE material and the deposition of Mn^{2+} in the SEI causes the ionic conductivity to decrease in the SEI, increasing the resistivity in the SEI. Test cases were simulated including both material loss ($\epsilon_{s,pos}$), and Mn deposition, only $\epsilon_{s,pos}$ loss, and only Mn deposition.

The main contributor for capacity loss is the $\epsilon_{s,pos}$ loss (Figure 6.20). A negligible difference in capacity can be seen in the red and green curves as a result of Mn deposition. The overall resistance increase is very small in all three cases, the Mn deposition in the SEI for this thin SEI only gives a minor increase (Figure 6.21a). The main resistance increase is thought to originate from the material loss that results in a shifted balance between the electrodes where less of the NE is utilised (Figure 6.21b). In this case the diffusion coefficient for the NE is slightly reduced at 50% SOC for the battery cell after 2000 cycles compared to the initial cycle.

When only including the Mn deposition the oxidation causes the electrodes to slip in relation to each other (Figure 6.21b). The NE slips toward lower voltages (higher SOL) and the PE toward higher voltage (lower SOL). With only a negligible resistance increase, this results in a minor capacity increase.

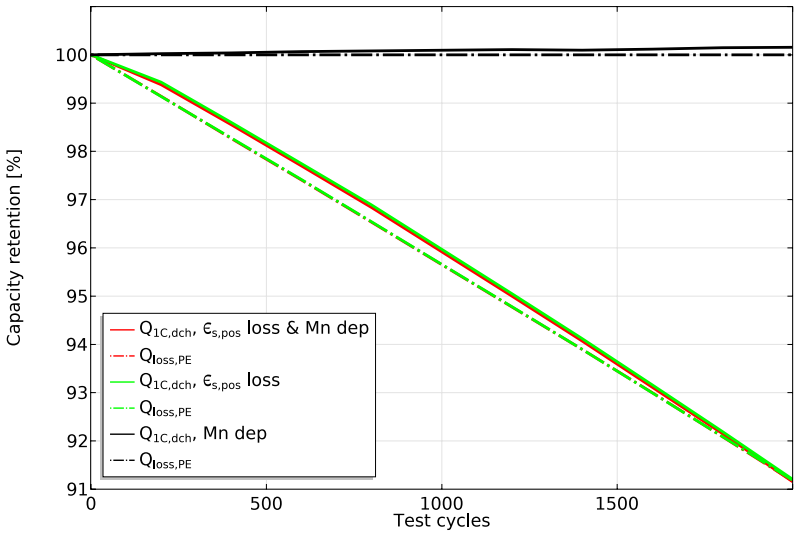

Figure 6.20: Simulated capacity retention for a cell with +1C/-1C in 0-100% SOC at 25°C when including oxidation at the PE causing loss of PE material and deposition of Mn^{2+} on the NE. Two cases only including deposition and only loss of PE material are also included.

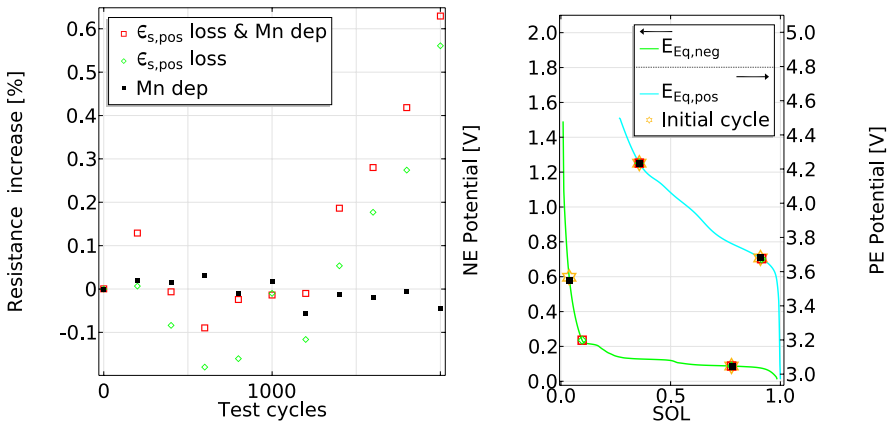

(a) (b)

Figure 6.21: Simulated ageing when only including Mn dissolution with and without loss of PE material and deposition on the NE for the +1C/-1C cycling in 0-100% SOC at 25°C. (a) The resulting cell discharge resistance increase at 50% SOC and (b) the SOL in the electrodes at beginning of the discharge and at the end of the discharge.

6.5.4 Contribution of Ageing Mechanisms

The different contributions when including both SEI growth and Mn dissolution were studied. Three cases including the different contributions from the Mn dissolution is compared to the SEI growth including loss of $\epsilon_{l,neg}$ (Figure 6.22). In all the tested case both electrodes slips toward higher voltages, where the slippage is largest for the SEI growth including loss of $\epsilon_{l,neg}$ (Figure 6.23b). Only including the Mn deposition results in a smaller capacity loss due to the oxidation causing the PE to slip in the same direction as the NE slips as a result of the SEI growth. The Mn depositions in the SEI gives a slight increased resistance in the SEI (Figure 6.23a). Including the loss of PE material increases the capacity loss and the cell experiences a larger resistance increase. A larger part of the PE is utilised compared to previous two cases and a slightly smaller part of the NE is utilised. Again including the Mn deposition in the SEI increases the resistance slightly, however, not enough to make an impact in the resulting capacity and the red curves are overlapping the green.

Two cases with even more enhanced PE material loss and change in ion conductivity in the SEI were simulated (Figure 6.24). The SEI growth is the same in all three cases, and initially limiting the capacity for the two enhanced cases. In the case with large PE material loss, the positive electrode becomes limiting for the capacity after 800 cycles. For the enhanced change in resistivity in the SEI, (4.28) and (4.60), an abrupt change in capacity can be seen as the film resistance becomes limiting at 1400 cycles. The resistance in both cases is of the same order (Figure 6.25a), but the combination with large PE material loss results in a larger overall capacity loss. The larger resistance increase will likely result in larger capacity loss as the ageing progresses.

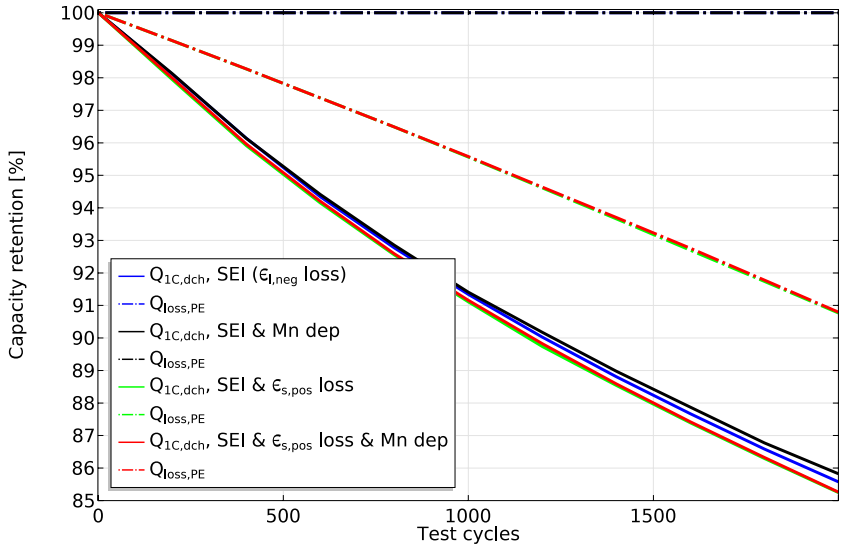

Figure 6.22: Simulated capacity retention for +1C/-1C 0-100% SOC at 25°C including both SEI growth with loss of $\epsilon_{l,neg}$ and the different contributions from the Mn dissolution.

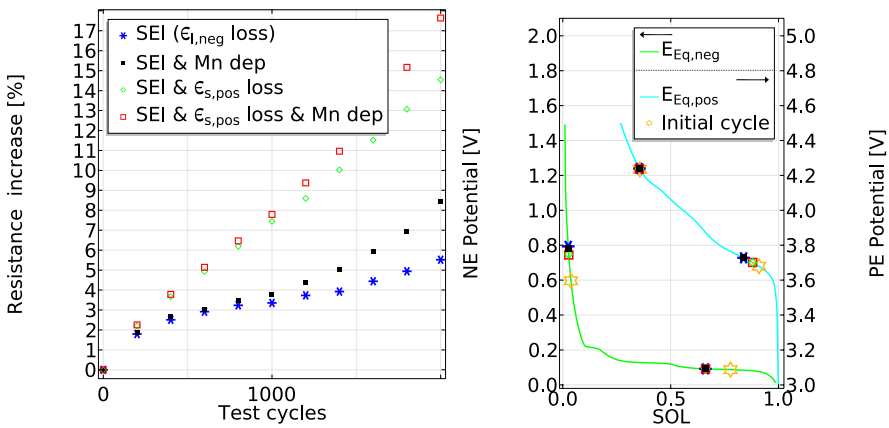

(a) (b)

Figure 6.23: Simulated ageing when including both SEI growth with loss of $\epsilon_{l,neg}$ and the different contributions from the Mn dissolution for the +1C/-1C cycling in 0-100% SOC at 25°C. (a) The resulting cell discharge resistance increase at 50% SOC and (b) the SOL in the electrodes at beginning of discharge and end of discharge.

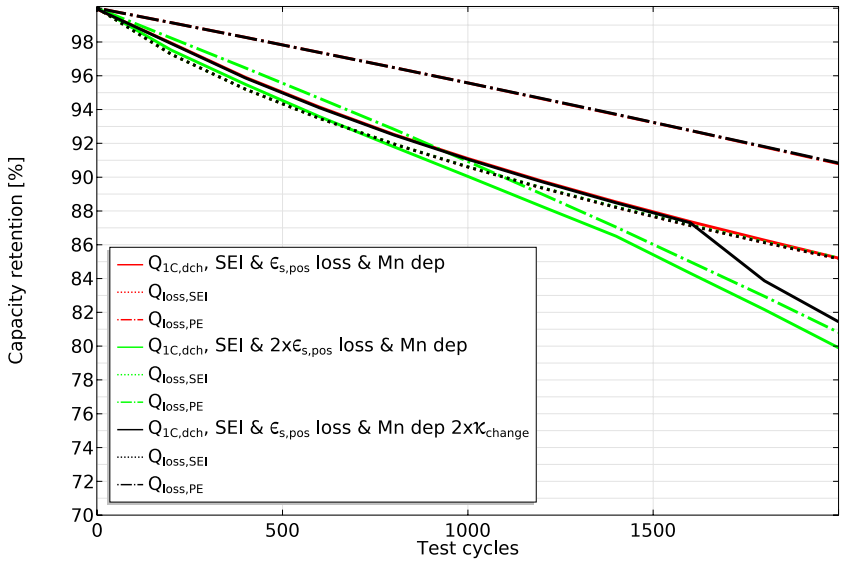

Figure 6.24: Simulated capacity retention for +1C/-1C 0-100% SOC at 25°C enhancing the contribution from the different ageing mechanisms.

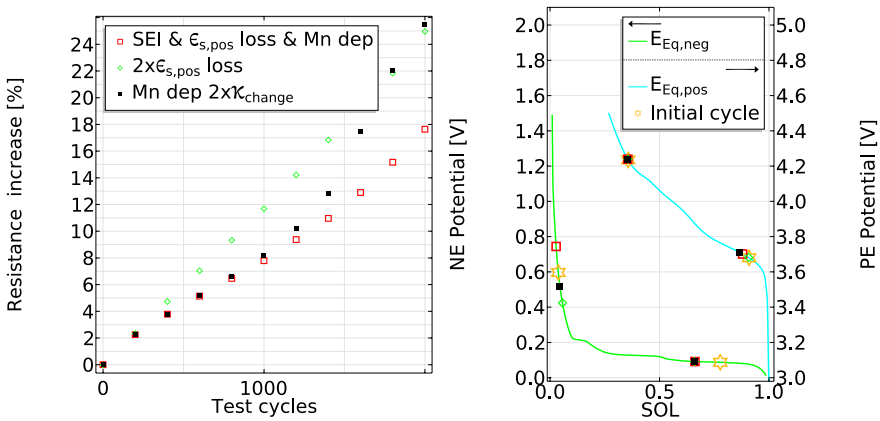

(a) (b)

Figure 6.25: Simulated ageing when enhancing the contribution from the different ageing mechanisms for the +1C/-1C cycling in 0-100% SOC at 25°C. (a) The resulting cell discharge resistance increase at 50% SOC and (b) the SOL in the electrodes at beginning of discharge and end of discharge.

6.6 Simulation of Ageing in Small DOD

The measurement results using a 10% DOD at 25°C were compared with simulations. Both the effects of SOC placement and C-rate were investigated. The measured capacities are recognised by the dashed lines and the measured resistances by dashed lines with circles.

6.6.1 Simulation at Different SOC

For the simulations at different SOC placements, four different levels with +2C/-2C were used, 10-20, 40-50, 60-70 and 70-80% SOC (Figure 6.26). As noted in Section 5.4.2 the complete capacity degradation curve could not be recreated in the model, however, the SEI growth seems to be the main reason for the distinct separation between the capacity degradation curves at the low and high SOC levels. The increase in loss of recyclable Li due to SEI growth difference are minor among the three higher SOC intervals simulated, but notably smaller for the lowest SOC interval. The measured resistance increase is captured by the simulations, where the SEI growth leads to a higher film resistance on the NE particles.

The model cannot fully capture the PE material loss. According to the ESMLE the PE material loss should be around 5.7% for the 10-20% case (cell #4), and 5.2% for the 40-50% case (cell #7). For the 70-80% case (cell #12) no slippage analysis was possible, although the data for cell #14, 80-90% SOC, and cell #9, 60-70% SOC, indicates that it should be in the range of 8%. Conclusions that can be drawn from comparing the P2D simulations to the ESMLE and PM analysis is that all PE material loss does not come from the Mn dissolution. The PE material loss is in the range of 5% in the low SOC interval cycled with 2C, but both the PM analysis and simulation show negligible Mn dissolution at these low SOC levels. This implies that at least one important ageing mechanism is unaccounted for in this ageing model.

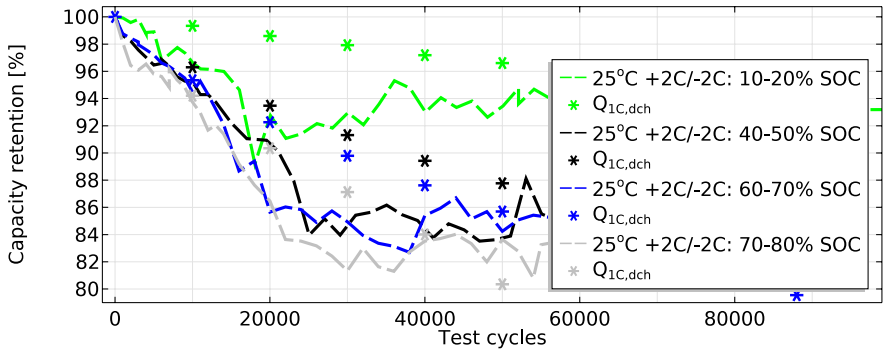

(a)

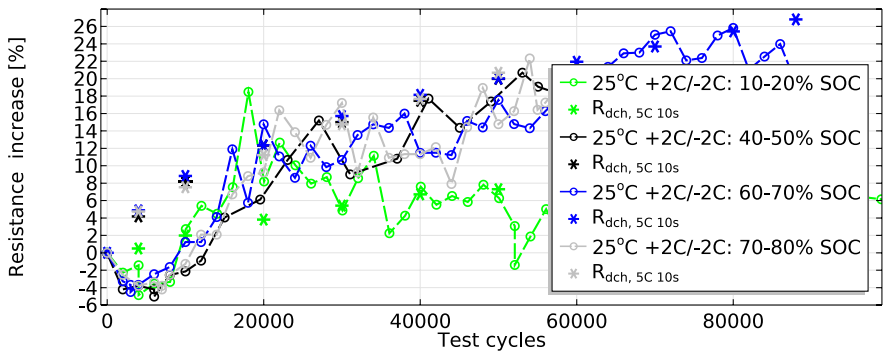

(b)

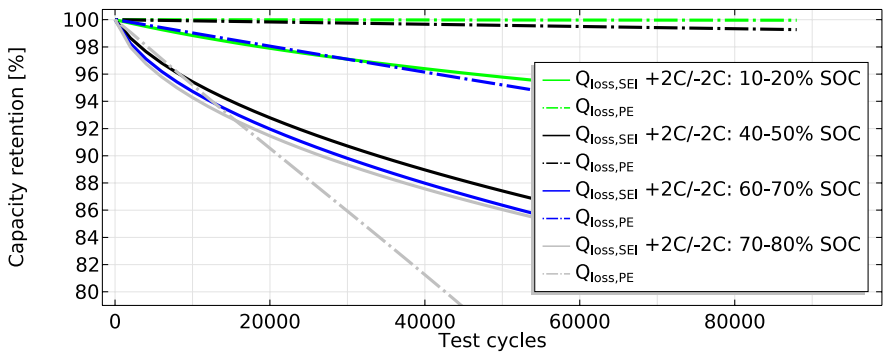

(c)

Figure 6.26: Measured and simulated ageing for different SOC intervals when using 10% DOD with +2C/-2C cycling at 25°C. (a) The resulting 1C cell discharge capacity (- - measured and * simulated), and (b) 5C 10s pulse resistance increase at 50% SOC (-o- measured and * simulated), and (c) The contribution from loss of cyclable Li^+ and PE material.

6.6.2 Simulations at Different C-rates

The simulations of different C-rates were performed at 10-20% and 60-70% SOC. The simulations for at low SOC results in too low capacity degradation (Figure 6.27). Low PE material loss can be one of the reasons. The results from the ESMLE for cells #3 (+1C/-1C 10-20% SOC) and #4 (+2C/-2C 10-20% SOC) at 25°C and cells #21 (+1C/-1C 10-20% SOC), #22 (+2C/-2C 10-20% SOC), and #23 (+4C/-4C 10-20% SOC) at 35°C show that the PE material loss and NE slippage is C-rate dependent. The trend with increased ageing for increased C-rates is though captured for both the SEI growth and PE material loss, even though at a too low rate of PE material loss.

The resistance increase for the 1C and 2C case is in the right range and mainly a result of the SEI growth. For the measured 4C case (cell #5, +4C/-4C 10-20% SOC at 25°C) there is no resistance increase. It was not possible to conduct the ESMLE for Cell #5, however, cell #23 tested at 35°C was, and it showed large PE material loss. The large PE material loss has through the ICA analysis been established to be in the NMC particles, this shows even more clearly that the hypothesis for all the loss of PE being related to the Mn dissolution has to be revised.

For the simulations in 60-70% SOC the results were unexpected (Figure 6.28). The measured results show the same trend as for the low SOC but accelerated, however, the simulations give a completely reversed trend where 1C is more detrimental compared to 2C and 4C. The PE material loss follows the expected trend, thus the main reason for the unexpected overall trend must be the SEI growth. At this potential the limiting current for the SEI growth is reached and the time each cycle takes is significantly different. The 1C cycle takes 2 and 4 times longer to complete the charge than the 2C and 4C cycles, consequently resulting in more SEI growth. This is also mirrored in the resistance increase, where the 1C case has too high resistance.

For both 4C cases the resistance increase is negligible, even so the ESMLE shows large slippage indicating more SEI growth. One hypothesis is that the high C-rate causes an unstable SEI to be formed that cracks or breaks down during cycling, providing a pristine graphite surface for renewed SEI reactions. Cracking or breakdown of the SEI is not included in the model and could be one reason the models fail to fully capture the trends seen in the experimental data.

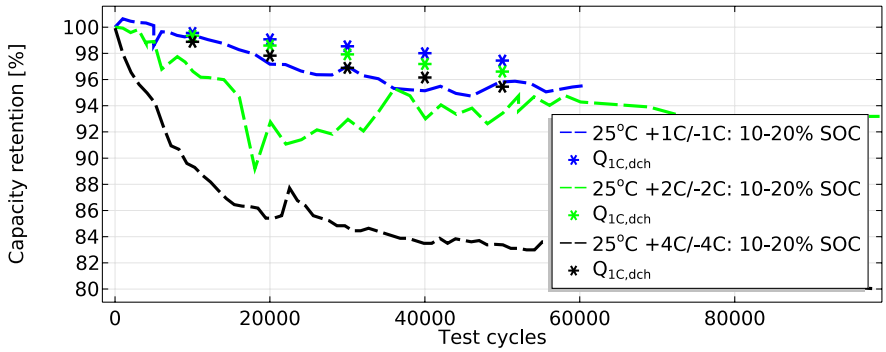

(a)

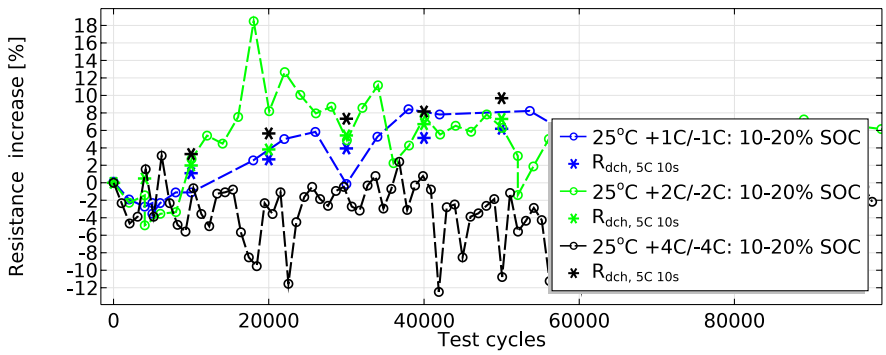

(b)

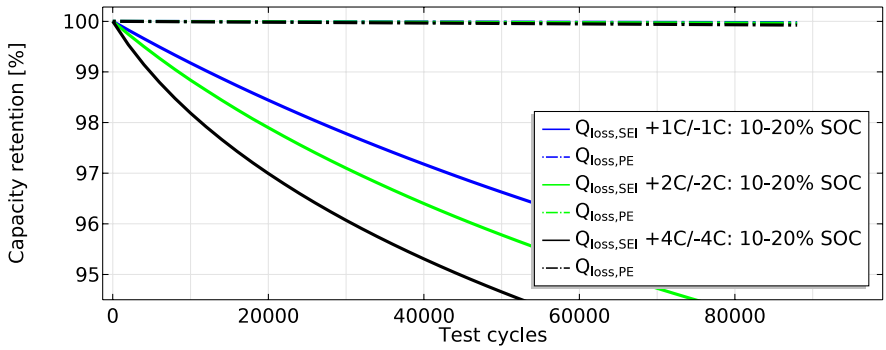

(c)

Figure 6.27: Simulated ageing for different C-rates when using 10-20% SOC cycling at 25°C. (a) The resulting 1C cell discharge capacity (- - measured and * simulated), (b) 5C 10s pulse resistance increase at 50% SOC (-o- measured and * simulated) compared to measured data, and (c) The contribution from loss of cyclable Li and PE material.

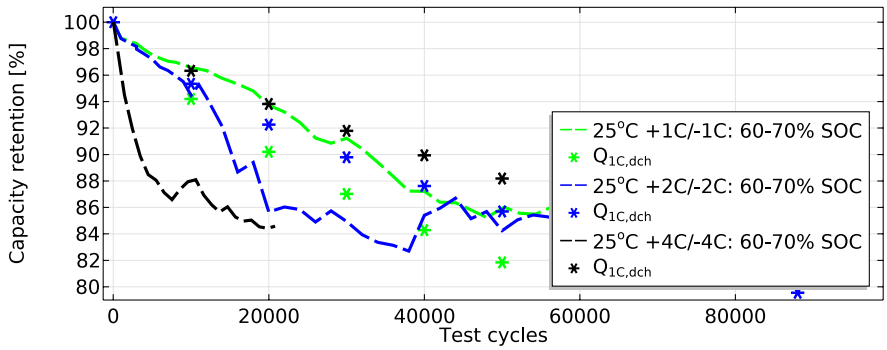

(a)

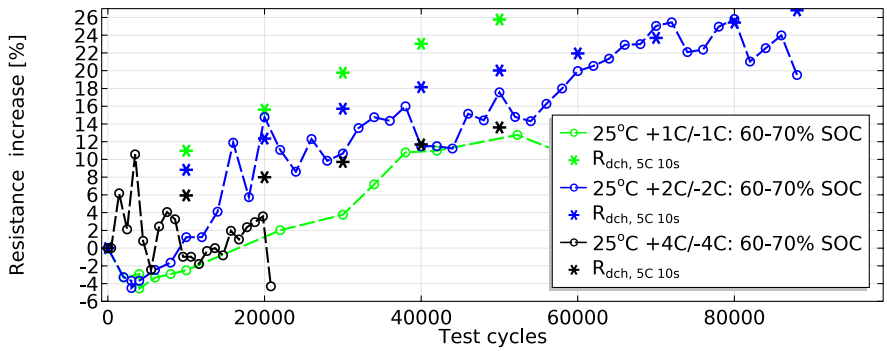

(b)

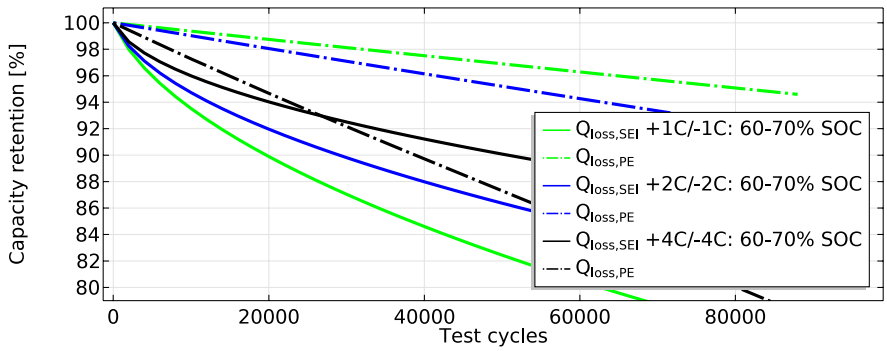

(c)

Figure 6.28: Simulated ageing for different C-rates when using 60-70% SOC cycling at 25°C. (a) The resulting 1C cell discharge capacity (- - measured and * simulated) and (b) 5C 10s pulse resistance increase at 50% SOC (-o- measured and * simulated) compared to measured data. (c) the contribution from loss of cyclable Li and PE material loss.

Chapter 7

Conclusions

In this thesis, the results from an extensive test matrix for commercial cells is presented together with an empirical ageing model and a physics-based ageing model. The results from the lifetime cycling tests showed the expected temperature dependence for 90% DOD, that higher temperature degrades the battery faster, while a different and interesting observation was made for the tests performed in 10% DOD. The temperature dependence had little effect within SOC intervals lower than 50%. The expected temperature dependence could first be observed above 50% SOC and only at temperatures above 40°C.

The study also confirms that operating at high SOC levels lead to more rapid ageing; only moderate ageing could be observed in the low 10% SOC intervals, while more rapid ageing was noted for SOC intervals higher than 40% SOC. For cycling above 60% SOC, there are no large differences in the capacity retention with respect to the specific SOC interval. Test results also showed that the Hyzem Rural drive cycle is less detrimental compared to the CC cycle with the same RMS current.

Using the derived empirical model, a study was conducted regarding how various driving strategies for an EV could affect the cycle life of the battery. The results showed that by driving the vehicle at lower SOC levels, when possible, improved the lifetime of the battery substantially. For a personal vehicle, that is spending most of its time parked, the model showed that the largest part of the ageing comes from the calendar ageing (parking). It was also demonstrated that the calendar ageing contribution could be much reduced by avoiding high SOC by planning the charging in proximity to the driving and not charging more than needed.

Parameterising a P2D model is a difficult task, and even more difficult when attempting to extract parameters from a commercial cell. Complete reverse engineering is of course not possible, however, it is possible to extract

a sufficient number of parameters from material analysis of the different cell components, after disassembling a cell, for obtaining a useful model. By introducing possible side reactions, the ageing processes can be simulated and can give possible explanations to phenomena seen in the measurements. An example is model prediction of the SEI growth, where the simulated growth rate become more severe in the higher SOC intervals compared to the lower ones, which explains the test results for the 10% DODs. The specific parameterisation in this case used calendar ageing data from the measurement.

The contributions of the different ageing mechanisms were investigated in a few cases where the parameters linked to the investigated mechanisms were slightly enhanced. In the case of SEI growth, the loss of electrolyte volume in the NE made only a small resistance contribution, not enough to notably affect the usable capacity. The capacity loss is thus mainly determined by the loss of Li^+. In the simulated case of a significantly increased resistance in the SEI it became limiting for the capacity when the resistance increase reached 80%.

In the case of Mn dissolution, the oxidation on the PE results in a small capacity increase due to the electrode slippage. When including loss of active material this becomes limiting for the capacity. As the SEI layer growth in this case is not included, the resistance increase from deposition of Mn^{2+} in the SEI is very small. However, when including the SEI growth and a large change in resistance, as a function of deposited Mn^{2+}, the film resistance can become limiting for the capacity and for the power.

The ageing analysis of the selected tested cells showed that SEI growth seems to be the dominating ageing mechanism leading to loss of cyclable Li^+ and increased cell resistance. The PM analysis showed that the increased cell resistance is mainly due to increased resistance in the NE. The cell tested at high SOC also had a thicker SEI layer compared to the cell tested at low SOC. This trend could accurately be captured by the P2D model, where the SEI growth and cell resistance increased with increasing SOC. However, the trend with increasing ageing with C-rate could only be captured by the model at the low SOC level and not at the high. The main reason for this is assumed to be that when simulating ageing in the higher SOC level the limiting current for the SEI reaction is reached, thus the conclusion is that the normalisation of the SEI current used in the model is not sufficient to account for the C-rate dependence for the SEI growth.

Another discrepancy is the low PE material loss in the simulated cases at low SOC levels. The ageing analysis showed that the cells tested in low SOC intervals had a very small amount of Mn in the SEI, but experienced increased loss of PE material with increasing C-rate. Further, the PE material loss was established to be from the NMC material. The Mn dissolution from LMO

is likely to start above 4.0 V, for NMC first at 4.3 V, a voltage level that is not reached in the investigated cell. As the model demonstrates, the Mn dissolution cannot account for the PE material loss at low SOC levels, hence an additional ageing mechanism is required. Therefore, the loss of NMC material is more probable to be linked to cracked particles due to material stress from concentration gradients and this should be accounted for in the model.

The cross-talk of the electrodes, where Mn^{2+} is deposited in the SEI at the NE and give rise to a resistance increase, cannot fully account for the total cell resistance increase for the simulated case of 80% DOD. Here, the accelerated ageing trend could not be captured by the model. Increasing the change in the ionic conductivity (increasing the SEI resistance) leads to a too high resistance increase for the 10% DOD case. As the PE material loss were in a reasonable range it is assumed that the SEI growth should be larger. The large DOD causes the graphite to expand and contract more compared to the 10% DOD, this could lead to cracking of the SEI and thus more SEI growth.

To summarise the key findings, the LiB is a highly complex system. Understanding how different type of usage causes different ageing mechanisms to occur and how to limit them in various application can improve the LiB lifetime. That high SOC, temperature and C-rate are increasing the ageing is well established, here it has been shown that in some conditions this can be circumvented. At low SOC the increase in ageing with increased temperature is moderate, a slightly increased temperature can instead be beneficial, especially when the C-rate is high. In the low SOC levels the LiB seem to be less affected by the higher C-rates, as compared to the same conditions at high SOC levels. The LiB benefits from being used in a small DOD placed at low SOC levels. Refraining from fully charging the LiB will improve the lifetime.

Chapter 8

Future Work

Conducting lifetime tests are time consuming and costly, further development of test methods for accelerated ageing tests and RPT, with lowest possible ageing impact, is therefore required. In this thesis the ageing at different SOC levels has been investigated, but is far from complete. Calendar ageing in more than three intervals is required to fully map the ageing at different SOC levels and to explain the increased ageing at 75% SOC compared to 90% SOC.

What RPT used in the lifetime testing and with what frequency is a topic that has been under discussion for as long as lifetime testing has been conducted. To design an RPT test so that as much information as possible can be extracted from the test, while the test itself should be as short as possible and influence the cell as little as possible, is challenging. Using slow charge and discharge cycles in the RPT test open possibilities in tracking of the slippage of the electrodes with ageing, however it is time consuming.

In the tests conducted in 10% DODs, large fluctuations in the capacity could be seen. Further investigation to find the reason for the fluctuations would be interesting. The capacity degradation curve also showed a different behaviour compared to large DODs, going into a more moderate ageing trend where the large DOD entered an accelerated ageing trend. In most applications it is not viable to only use 10% of the capacity, why an improved understanding for what causes the accelerated ageing in large DODs and especially how to detect and avoid it would be highly valuable.

The hysteresis in the cell is not yet fully understood, although some hypotheses have been brought forward, it has not been accounted for in the model. To be able to incorporate this in the model, such knowledge is needed.

When it comes to P2D models, robust and accessible methods for parameter extraction is a topic that requires further attention. Depending on

what the model is built to predict or estimate, some parameters will hold higher importance. Deeper investigations of the sensitivity of the different parameters will help in determining what parameters to focus on.

In this thesis, the temperature dependence parameterisation of the model was only initiated. To verify and capture the full temperature behaviour further parameterisation would be a valuable task.

Calculating the diffusion coefficients from EIS or GITT measurements has been done previously. In this thesis an LS optimisation to the pulse voltage from RPT tests was used to estimate the diffusion coefficient for the PE. However, attempting to optimise for both active materials simultaneously led to poor results. By accounting also for the change in the equilibrium potential curve will likely improve the results. This type of optimisation against full cell data may be a powerful tool in parameterising P2D models.

The time factor was in this model placed in the equations for the side reaction currents. If these currents are large this could lead to increased polarisation in the cell. For the parameter set used in this thesis the error is small, to make the model applicable to cells with large side reaction currents a better placement for this factor should be investigated.

In this model the two PE materials LMO and NMC have been simulated as one single material. Simulations of LMO and NMC as separate electrode materials, with the possibility of using different properties for the two materials, will give further insights into the discrepancies of the model compared to measurement data. Further, simulating the materials separately will also enable contributions of different ageing mechanisms for the different materials. Overall results show that it is the NMC that experience the main PE material loss. NMC particles are known to be more prone to crack compared to LMO and, therefore, separating the contribution from cracked particles from the Mn dissolution is needed.

The extraction of ageing parameters for the ageing models is definitely a topic that requires more attention. For instance, from what type of ageing tests should parameters be extracted? For the Mn dissolution there are still several alternative processes proposed, which requires further studies to establish what process is dominating for the studied cell. The fact that Mn ends up on the NE researchers in the field agree on, although the issue of how it deposits on the NE is fairly unclear. Understanding this process better is vital for prolonging the lifetime of cells containing materials with Mn and other TM. Deeper understanding how the TM influence the SEI is even more important as the development is going towards higher voltage cells, increasing the risk of TM dissolution.

References

[1] European Commission, "A European Strategy for low-emission mobility," 2016.

[2] C. McFadden, "A brief history and evolution of electric cars," *Interesting Engineering*, 2018.

[3] K. T. T. Nagaura, "Progress in batteries and solar cells," *JECS Press Inc.*, vol. 9, p. 209, 1990.

[4] D. H. Jang and S. M. Oh, "Electrolyte effects on spinel dissolution and cathodic capacity losses in 4V $Li/Li_xMn_2O_4$ rechargeable cells," *Journal of The Electrochemical Society*, vol. 144, no. 10, pp. 3342–3348, 1997.

[5] D. Aurbach, M. D. Levi, E. Levi, and A. Schechter, "Failure and Stabilization Mechanisms of Graphite Electrodes," *Journal of Physical Chemistr B*, vol. 101, p. 2195, 1997.

[6] J. Vetter, P. Novák, M. Wagner, C. Veit, K.-C. Möller, J. Besenhard, M. Winter, M. Wohlfahrt-Mehrens, C. Vogler, and A. Hammouche, "Ageing mechanisms in lithium-ion batteries," *Journal of Power Sources*, vol. 147, no. 1–2, pp. 269 – 281, 2005.

[7] A. M. Andersson and K. Edström, "Chemical composition and morphology of the elevated temperature sei on graphite," *Journal of The Electrochemical Society*, vol. 148, no. 10, pp. A1100–A1109, 2001.

[8] K. Edström, M. Herstedt, and D. P. Abraham, "A new look at the solid electrolyte interphase on graphite anodes in li-ion batteries," *Journal of Power Sources*, vol. 153, no. 2, pp. 380 – 384, 2006. Selected papers presented at the 2004 Meeting of the International Battery Association.

[9] R. Petibon, C. P. Aiken, N. N. Sinha, J. C. Burns, H. Ye, C. M. VanElzen, G. Jain, S. Trussler, and J. R. Dahn, "Study of electrolyte additives using electrochemical impedance spectroscopy on symmetric

cells," *Journal of The Electrochemical Society*, vol. 160, no. 1, pp. A117–A124, 2013.

[10] D. J. Xiong, R. Petibon, M. Nie, L. Ma, J. Xia, and J. R. Dahn, "Interactions between positive and negative electrodes in li-ion cells operated at high temperature and high voltage," *Journal of The Electrochemical Society*, vol. 163, no. 3, pp. A546–A551, 2016.

[11] E. Peled and S. Menkin, "Review—SEI: Past, present and future," *Journal of The Electrochemical Society*, vol. 164, no. 7, pp. A1703–A1719, 2017.

[12] J. Newman and W. Tiedemann, "Porous-electrode theory with battery applications," *AIChE Journal*, vol. 21, no. 1, pp. 25–41, 1975.

[13] M. Doyle, T. F. Fuller, and J. Newman, "Modeling of Galvanostatic Charge and Discharge of the Lithium/Polymer/Insertion Cell," *Journal of The Electrochemical Society*, vol. 140, no. 6, pp. 1526–1533, 1993.

[14] M. Doyle, J. Newman, A. S. Gozdz, C. N. Schmutz, and J. Tarascon, "Comparison of modeling predictions with experimental data from plastic lithium ion cells," *Journal of The Electrochemical Society*, vol. 143, no. 6, pp. 1890–1903, 1996.

[15] M. D. Levi and D. Aurbach, "Simultaneous Measurements and Modeling of the Electrochemical Impedance and the Cyclic Voltammetric Characteristics of Graphite Electrodes Doped with Lithium," *The Journal of Physical Chemistry B*, vol. 101, no. 23, pp. 4630–4640, 1997.

[16] M. Meyer, L. Komsiyska, B. Lenz, and C. Agert, "Study of the local SOC distribution in a lithium-ion battery by physical and electrochemical modeling and simulation," *Applied Mathematical Modelling*, vol. 37, no. 4, pp. 2016 – 2027, 2013.

[17] E. Peled, "The electrochemical behavior of alkali and alkaline earth metals in nonaqueous battery systems—the solid electrolyte interphase model," *Journal of The Electrochemical Society*, vol. 126, no. 12, pp. 2047–2051, 1979.

[18] R. Darling and J. Newman, "Modeling Side Reactions in Composite $\mathrm{Li}_y\mathrm{Mn}_2\mathrm{O}_4$ Electrodes," *Journal of The Electrochemical Society*, vol. 145, no. 3, pp. 990–998, 1998.

[19] P. Ramadass, B. Haran, P. M. Gomadam, R. White, and B. N. Popov, "Development of First Principles Capacity Fade Model for Li-Ion Cells," *Journal of The Electrochemical Society*, vol. 151, no. 2, pp. A196–A203, 2004.

[20] A. M. Colclasure, K. A. Smith, and R. J. Kee, "Modeling detailed chemistry and transport for solid-electrolyte-interface (SEI) films in Li–ion batteries," *Electrochimica Acta*, vol. 58, pp. 33 – 43, 2011.

[21] J. Groot, "State-of-Health Estimation of Li-ion Batteries: Cycle Life Test Methods," 2012. Licentiate thesis.

[22] J. Schmalstieg, S. Käbitz, M. Ecker, and D. U. Sauer, "From accelerated aging tests to a lifetime prediction model: Analyzing lithium-ion batteries," in *2013 World Electric Vehicle Symposium and Exhibition (EVS27)*, pp. 1–12, Nov 2013.

[23] E. Thomas, H. Case, D. Doughty, R. Jungst, G. Nagasubramanian, and E. Roth, "Accelerated power degradation of Li-ion cells ," *Journal of Power Sources*, vol. 124, no. 1, pp. 254 – 260, 2003.

[24] P. Ramadass, B. Haran, R. White, and B. N. Popov, "Mathematical modeling of the capacity fade of Li-ion cells ," *Journal of Power Sources*, vol. 123, no. 2, pp. 230 – 240, 2003.

[25] R. B. Wright, C. G. Motloch, J. R. Belt, J. P. Christophersen, C. D. Ho, R. A. Richardson, I. Bloom, S. A. Jones, V. S. Battaglia, G. L. Henriksen, T. Unkelhaeuser, D. Ingersoll, H. L. Case, S. A. Rogers, and R. A. Sutula, "Calendar-and cycle-life studies of advanced technology development program generation 1 lithium-ion batteries," *Journal of power sources*, vol. 110, pp. 445–470, 08/2002 2002.

[26] J. Groot, *State-of-Health Estimation of Li-ion Batteries: Ageing Models*. PhD thesis, Chalmers University of Technology, 2014.

[27] T. F. Fuller, M. Doyle, and J. Newman, "Simulation and optimization of the dual lithium ion insertion cell," *Journal of The Electrochemical Society*, vol. 141, no. 1, pp. 1–10, 1994.

[28] G. Ning, R. White, and B. Popov, "A generalized cycle life model of rechargeable Li-ion batteries," *Electrochimica Acta*, vol. 51, pp. 2012–2022, 2006.

[29] H. Ekström and G. Lindbergh, "A Model for Predicting Capacity Fade due to SEI Formation in a Commercial Graphite/$LiFePO_4$ Cell," *Journal of The Electrochemical Society*, vol. 162, no. 6, pp. A1003–A1007, 2015.

[30] Y. K. Lee, J. Park, and W. Lu, "A comprehensive experimental and modeling study on dissolution in li-ion batteries," *Journal of The Electrochemical Society*, vol. 166, no. 8, pp. A1340–A1354, 2019.

[31] Y. Dai, L. Cai, and R. E. White, "Capacity fade model for spinel limn2o4 electrode," *Journal of The Electrochemical Society*, vol. 160, no. 1, pp. A182–A190, 2013.

[32] X. Lin, J. Park, L. Liu, Y. Lee, A. M. Sastry, and W. Lu, "A comprehensive capacity fade model and analysis for li-ion batteries," *Journal of The Electrochemical Society*, vol. 160, no. 10, pp. A1701–A1710, 2013.

[33] J. Schmalstieg, C. Rahe, M. Ecker, and D. U. Sauer, "Full Cell Parameterization of a High-Power Lithium-Ion Battery for a Physico-Chemical Model: Part I. Physical and Electrochemical Parameters," *Journal of The Electrochemical Society*, vol. 165, no. 16, pp. A3799–A3810, 2018.

[34] J. Schmalstieg and D. U. Sauer, "Full Cell Parameterization of a High-Power Lithium-Ion Battery for a Physico-Chemical Model: Part II. Thermal Parameters and Validation," *Journal of The Electrochemical Society*, vol. 165, no. 16, pp. A3811–A3819, 2018.

[35] M. Ecker, N. Nieto, S. Käbitz, J. Schmalstieg, H. Blanke, A. Warnecke, and D. U. Sauer, "Calendar and cycle life study of Li(NiMnCo)O_2-based 18650 lithium-ion batteries," *Journal of Power Sources*, vol. 248, pp. 839 – 851, 2014.

[36] R. Spotnitz, "Simulation of capacity fade in lithium-ion batteries," *Journal of Power Sources*, vol. 113, no. 1, pp. 72 – 80, 2003.

[37] V. Srinivasan and J. Newman, "Design and optimization of a natural graphite/iron phosphate lithium-ion cell," *Journal of The Electrochemical Society*, vol. 151, no. 10, pp. A1530–A1538, 2004.

[38] C. Zhan, J. Lu, A. Jeremy Kropf, T. Wu, A. N. Jansen, Y.-K. Sun, X. Qiu, and K. Amine, "Mn(ii) deposition on anodes and its effects on capacity fade in spinel lithium manganate-carbon systems," *Nature Communications*, vol. 4, p. 2437, Sep 2013. Article.

[39] A. M. Tarascon, J.-M., "Issues and challenges facing rechargeable lithium batteries," *Nature*, vol. 414, p. 359, 2001.

[40] T. Placke, R. Kloepsch, S. Dühnen, and M. Winter, "Lithium ion, lithium metal, and alternative rechargeable battery technologies: the odyssey for high energy density," *Journal of Solid State Electrochemistry*, vol. 21, pp. 1939–1964, Jul 2017.

[41] H. D. Abruña, Y. Kiya, and J. C. Henderson, "Batteries and electrochemical capacitors," *Physics Today*, vol. 61, no. 12, pp. 43–47, 2008.

[42] M. Winter, J. O. Besenhard, M. E. Spahr, and P. Novák, "Insertion Electrode Materials for Rechargeable Lithium Batteries," *Advanced Materials*, vol. 10, no. 10, pp. 725–763, 1998.

[43] B. Simon, S. Flandrois, K. Guerin, A. Fevrier-Bouvier, I. Teulat, and P. Biensan, "On the choice of graphite for lithium ion batteries," *Journal of Power Sources*, vol. 81-82, pp. 312 – 316, 1999.

[44] N. Nitta, F. Wu, J. T. Lee, and G. Yushin, "Li-ion battery materials: present and future," *Materials Today*, vol. 18, no. 5, pp. 252 – 264, 2015.

[45] T. Nordh, *A Quest for the Unseen Surface Layer Formation on $Li_4Ti_5O_12$ Li-Ion Battery Anodes.* PhD thesis, Uppsala University, 2017.

[46] J. B. Goodenough and Y. Kim, "Challenges for rechargeable li batteries," *Chemistry of Materials*, vol. 22, no. 3, pp. 587–603, 2010.

[47] C. M. J. Alain Mauger, Haiming Xie, "Composite anodes for lithium-ion batteries: status and trends," *AIMS Materials Science*, vol. 3, no. matersci-03-01054, p. 1054, 2016.

[48] K. Xu, "Nonaqueous liquid electrolytes for lithium-based rechargeable batteries," *Chemical Reviews*, vol. 104, no. 10, pp. 4303–4418, 2004.

[49] J. R. Croy, A. Abouimrane, and Z. Zhang, "Next-generation lithium-ion batteries: The promise of near-term advancements," *MRS Bulletin*, vol. 39, no. 5, p. 407–415, 2014.

[50] K. C. Högström, *The Complex Nature of the Electrode/Electrolyte Interfaces in Li-ion Batteries.* PhD thesis, Uppsala University, 2014.

[51] M. Klett, *Electrochemical Studies of Aging in Lithium-Ion Batteries.* PhD thesis, Royal Institute of Technology, 2014.

[52] G. K. Prasad and C. D. Rahn, "Model based identification of aging parameters in lithium ion batteries," *Journal of Power Sources*, vol. 232, pp. 79 – 85, 2013.

[53] D. H. Jang, Y. J. Shin, and S. M. Oh, "Dissolution of Spinel Oxides and Capacity Losses in 4V Li/Lix Mn_2O_4 Cells," *Journal of The Electrochemical Society*, vol. 143, no. 7, pp. 2204–2211, 1996.

[54] J. A. Gilbert, I. A. Shkrob, and D. P. Abraham, "Transition metal dissolution, ion migration, electrocatalytic reduction and capacity loss in lithium-ion full cells," *Journal of The Electrochemical Society*, vol. 164, no. 2, pp. A389–A399, 2017.

[55] I. Buchberger, S. Seidlmayer, A. Pokharel, M. Piana, J. Hattendorff, P. Kudejova, R. Gilles, and H. A. Gasteiger, "Aging Analysis of Graphite/$LiNi_{1/3}Mn_{1/3}Co_{1/3}O_2$ Cells Using XRD, PGAA, and AC Impedance," *Journal of The Electrochemical Society*, vol. 162, no. 14, pp. A2737–A2746, 2015.

[56] V. Agubra and J. Fergus, "Lithium ion battery anode aging mechanisms," *Materials*, vol. 6, no. 4, pp. 1310–1325, 2013.

[57] S. J. An, J. Li, C. Daniel, D. Mohanty, S. Nagpure, and D. L. W. III, "The state of understanding of the lithium-ion-battery graphite solid electrolyte interphase (SEI) and its relationship to formation cycling," *Carbon*, vol. 105, pp. 52 – 76, 2016.

[58] A. Zaban and D. Aurbach, "Impedance spectroscopy of lithium and nickel electrodes in propylene carbonate solutions of different lithium salts a comparative study," *Journal of Power Sources*, vol. 54, no. 2, pp. 289 – 295, 1995. Proceedings of the Seventh International Meeting on Lithium Batteries.

[59] E. Peled, D. Golodnitsky, and G. Ardel, "Advanced model for solid electrolyte interphase electrodes in liquid and polymer electrolytes," *Journal of The Electrochemical Society*, vol. 144, no. 8, pp. L208–L210, 1997.

[60] Y. Ein-Eli, "A new perspective on the formation and structure of the solid electrolyte interface at the graphite anode of li-ion cells," *Electrochemical and Solid-State Letters*, vol. 2, no. 5, pp. 212–214, 1999.

[61] C. H. Lee, J. A. Dura, A. LeBar, and S. C. DeCaluwe, "Direct, operando observation of the bilayer solid electrolyte interphase structure: Electrolyte reduction on a non-intercalating electrode," *Journal of Power Sources*, vol. 412, pp. 725 – 735, 2019.

[62] O. C. Harris and M. H. Tang, "Molecular probes reveal chemical selectivity of the solid–electrolyte interphase," *The Journal of Physical Chemistry C*, vol. 122, no. 36, pp. 20632–20641, 2018.

[63] M. Tang, S. Lu, and J. Newman, "Experimental and theoretical investigation of solid-electrolyte-interphase formation mechanisms on glassy carbon," *Journal of The Electrochemical Society*, vol. 159, no. 11, pp. A1775–A1785, 2012.

[64] J. Christensen and J. Newman, "A mathematical model for the lithium-ion negative electrode solid electrolyte interphase," *Journal of The Electrochemical Society*, vol. 151, no. 11, pp. A1977–A1988, 2004.

[65] F. Single, A. Latz, and B. Horstmann, "Identifying the mechanism of continued growth of the solid–electrolyte interphase," *ChemSusChem*, vol. 11, no. 12, pp. 1950–1955, 2018.

[66] A. Bhandari and J. Bhattacharya, "Review—manganese dissolution from spinel cathode: Few unanswered questions," *Journal of The Electrochemical Society*, vol. 164, no. 2, pp. A106–A127, 2017.

[67] R. Xu, H. Sun, L. S. de Vasconcelos, and K. Zhao, "Mechanical and Structural Degradation of $LiNi_xMn_yCo_zO_2$ Cathode in Li-Ion Batteries: An Experimental Study," *Journal of The Electrochemical Society*, vol. 164, no. 13, pp. A3333–A3341, 2017.

[68] S. Solchenbach, G. Hong, A. T. S. Freiberg, R. Jung, and H. A. Gasteiger, "Electrolyte and sei decomposition reactions of transition metal ions investigated by on-line electrochemical mass spectrometry," *Journal of The Electrochemical Society*, vol. 165, no. 14, pp. A3304–A3312, 2018.

[69] L. Yang, M. Takahashi, and B. Wang, "A study on capacity fading of lithium-ion battery with manganese spinel positive electrode during cycling," *Electrochimica Acta*, vol. 51, no. 16, pp. 3228–3234, 2006.

[70] S. R. Gowda, K. G. Gallagher, J. R. Croy, M. Bettge, M. M. Thackeray, and M. Balasubramanian, "Oxidation state of cross-over manganese species on the graphite electrode of lithium-ion cells," *Phys. Chem. Chem. Phys.*, vol. 16, pp. 6898–6902, 2014.

[71] A. D. Robertson, S. H. Lu, and W. F. Howard, "M^{3+}-Modified $LiMn_2O_4$ Spinel Intercalation Cathodes: II. Electrochemical Stabilization by Cr^3," *Journal of The Electrochemical Society*, vol. 144, no. 10, pp. 3505–3512, 1997.

[72] T. Nordh, R. Younesi, M. Hahlin, R. F. Duarte, C. Tengstedt, D. Brandell, and K. Edström, "Manganese in the sei layer of li4ti5o12 studied by combined nexafs and haxpes techniques," *The Journal of Physical Chemistry C*, vol. 120, no. 6, pp. 3206–3213, 2016.

[73] T. Joshi, K. Eom, G. Yushin, and T. F. Fuller, "Effects of dissolved transition metals on the electrochemical performance and sei growth in lithium-ion batteries," *Journal of The Electrochemical Society*, vol. 161, no. 12, pp. A1915–A1921, 2014.

[74] M. Dubarry, B. Y. Liaw, M.-S. Chen, S.-S. Chyan, K.-C. Han, W.-T. Sie, and S.-H. Wu, "Identifying battery aging mechanisms in large format Li ion cells," *Journal of Power Sources*, vol. 196, no. 7, pp. 3420 – 3425, 2011.

[75] H. Berg, *Batteries for Electric Vehicles, Materials and Electrochemistry*. Cambridge University Press, 2015.

[76] T. Waldmann, A. Iturrondobeitia, M. Kasper, N. Ghanbari, F. Aguesse, E. Bekaert, L. Daniel, S. Genies, I. J. Gordon, M. W. Löble, E. De Vito, and M. Wohlfahrt-Mehrens, "Review—post-mortem analysis of aged lithium-ion batteries: Disassembly methodology and physico-chemical analysis techniques," *Journal of The Electrochemical Society*, vol. 163, no. 10, pp. A2149–A2164, 2016.

[77] B. Stiaszny, J. C. Ziegler, E. E. Krauß, J. P. Schmidt, and E. Ivers-Tiffée, "Electrochemical characterization and post-mortem analysis of aged $LiMn_2O_4$–$Li(Ni_0.5Mn_0.3Co_0.2)O_2$/graphite lithium ion batteries. Part I: Cycle aging," *Journal of Power Sources*, vol. 251, pp. 439 – 450, 2014.

[78] E. Björklund, E. Wikner, R. Younesi, D. Brandell, and K. Edström, "Influence of state-of-charge in commercial $LiNi_{0.33}Mn_{0.33}Co_{0.33}O_2$/$LiMn_2O_4$-graphite cells analyzed by synchrotron-based photoelectron spectroscopy," *Journal of Energy Storage*, vol. 15, pp. 172 – 180, 2018.

[79] T. Ohzuku, Y. Iwakoshi, and K. Sawai, "Formation of Lithium-Graphite Intercalation Compounds in Nonaqueous Electrolytes and Their Application as a Negative Electrode for a Lithium Ion (Shuttlecock) Cell," *Journal of The Electrochemical Society*, vol. 140, no. 9, pp. 2490–2498, 1993.

[80] M. Dubarry, C. Truchot, B. Y. Liaw, K. Gering, S. Sazhin, D. Jamison, and C. Michelbacher, "Evaluation of commercial lithium-ion cells based on composite positive electrode for plug-in hybrid electric vehicle applications. Part II. Degradation mechanism under 2 C cycle aging," *Journal of Power Sources*, vol. 196, pp. 10336–10343, 2011.

[81] S.-h. Wu and P.-H. Lee, "Nonlinear Cycling Aging of a Commercial 18650 Lithium Ion Cell," *Meeting Abstracts*, vol. MA2016-03, no. 2, p. 1198, 2016.

[82] K.-W. Nam, W.-S. Yoon, H. Shin, K. Y. Chung, S. Choi, and X.-Q. Yang, "In situ x-ray diffraction studies of mixed limn2o4–lini1/3co1/3mn1/3o2 composite cathode in li-ion cells during charge–discharge cycling," *Journal of Power Sources*, vol. 192, no. 2, pp. 652 – 659, 2009.

[83] T. Ohzuku, M. Kitagawa, and T. Hirai, "Electrochemistry of Manganese Dioxide in Lithium Nonaqueous Cell: III X-Ray Diffractional

Study on the Reduction of Spinel-Related Manganese Dioxide," *Journal of The Electrochemical Society*, vol. 137, no. 3, pp. 769–775, 1990.

[84] N. Leifer, F. Schipper, E. M. Erickson, C. Ghanty, M. Talianker, J. Grinblat, C. M. Julien, B. Markovsky, and D. Aurbach, "Studies of Spinel-to-Layered Structural Transformations in LiMn2O4 Electrodes Charged to High Voltages," *The Journal of Physical Chemistry C*, 2017.

[85] W. Dreyer, J. Jamnik, C. Guhlke, R. Huth, J. Moškon, and M. Gaberšček, "The origin of charge-discharge hysteresis in insertion li-ion cathodes," *Meeting Abstracts*, vol. MA2010-01, no. 3, p. 148, 2010.

[86] W. Dreyer, J. Jamnik, C. Guhlke, R. Huth, J. Moškon, and M. Gaberšček, "The thermodynamic origin of hysteresis in insertion batteries," *Nature Materials*, vol. 9, no. 3, p. 448, 2010.

[87] C. R. Birkl, E. McTurk, M. R. Roberts, P. G. Bruce, and D. A. Howey, "A parametric open circuit voltage model for lithium ion batteries," *Journal of The Electrochemical Society*, vol. 162, no. 12, pp. A2271–A2280, 2015.

[88] T. Sasaki, Y. Ukyo, and P. Novák, "Memory effect in a lithium-ion battery," *Nature Materials*, vol. 12, p. 569, 2013.

[89] E. Wikner, J. Lesser, and T. Thiringer, "Accelerated lifetime testing in small SOC intervals on commercial pouch cells, challenges and countermeasures." EPE'17 ECCE Europe, 2017.

[90] T. Grube, *Fuel Cells : Data, Facts and Figures, Chapter 2 Passenger Car Drive Cycles*. Wiley-VCH Verlag GmbH & Co. KGaA, 2016.

[91] T. G. Zavalis, *Mathematical Models for Investigation of Performance, Safety, and Aging in Lithium-Ion Batteries*. PhD thesis, KTH, Applied Electrochemistry, 2013.

[92] A. Nyman, M. Behm, and G. Lindbergh, "Electrochemical characterisation and modelling of the mass transport phenomena in $LiPF_6$–EC–EMC electrolyte," *Electrochimica Acta*, vol. 53, no. 22, pp. 6356 – 6365, 2008.

[93] P. Horsman, *Comprehensive Treatise of Electrochemistry, Vol. 6: Electrodics - Transport: Chapter 1 and 2*. Plenum Press, 1983.

[94] Y. Wang, S. Nakamura, M. Ue, and P. B. Balbuena, "Theoretical Studies to Understand Surface Chemistry on Carbon Anodes for Lithium-Ion Batteries: Reduction Mechanisms of Ethylene Carbonate," *Journal of American Chemical Society*, vol. 123, p. 11708, 2001.

[95] A. Wang, S. Kadam, L. Hong, S. Shi, and Y. Qi, "Review on modeling of the anode solid electrolyte interphase (SEI) for lithium-ion batteries," *npj Computational Materials*, vol. 4, no. 15, pp. 2057–3960, 2018.

[96] C. R. Yang, Y. Y. Wang, and C. C. Wan, "Composition Analysis of the Passive Film on the Carbon Electrode of a Lithium-Ion Battery with an EC-Based Electrolyte," *Journal of Power Sources*, vol. 72, p. 66, 1998.

[97] S.-P. Kim, A. C. T. van Duin, and V. B. Shenoy, "Effect of Electrolytes on the Structure and Evolution of the Solid Electrolyte Interphase (SEI) in Li-Ion Batteries: A Molecular Dynamics Study," *Journal of Power Sources*, vol. 196, p. 8590, 2011.

[98] K. Tasaki, A. Goldberg, J.-J. Lian, M. Walker, A. Timmons, and S. J. Harris, "Solubility of Lithium Salts Formed on the Lithium-Ion Battery Negative Electrode Surface in Organic Solvents," *Journal Electrochemistry Society*, vol. 156, p. A1019, 2009.

[99] A. M. Andersson, M. Herstedt, A. G. Bishop, and K. Edström, "The Influence of Lithium Salt on the Interfacial Reactions Controlling the Thermal Stability of Graphite Anodes," *Electrochimica Acta*, vol. 47, p. 1885, 2002.

[100] K. Ciosek Högström, S. Malmgren, M. Hahlin, H. Rensmo, F. Thébault, P. Johansson, and K. Edström, "The Influence of PMS-Additive on the Electrode/Electrolyte Interfaces in $LiFePO_4$/Graphite Li-Ion Batteries," *The Journal of Physical Chemistry C*, vol. 117, no. 45, pp. 23476–23486, 2013.

[101] D. Pantea, H. Darmstadt, S. Kaliaguine, and C. Roy, "Electrical conductivity of conductive carbon blacks: influence of surface chemistry and topology," *Applied Surface Science*, vol. 217, no. 1, pp. 181 – 193, 2003.

[102] L. O. Valøen and J. N. Reimers, "Transport properties of lipf6-based li-ion battery electrolytes," *Journal of The Electrochemical Society*, vol. 152, no. 5, pp. A882–A891, 2005.

[103] H. LIPSON and A. R. STOKES, "A new structure of carbon," *Nature*, vol. 149, p. 328, 1942.

[104] S. Muhammad, S. Lee, H. Kim, J. Yoon, D. Jang, J. Yoon, J.-H. Park, and W.-S. Yoon, "Deciphering the thermal behavior of lithium rich cathode material by in situ x-ray diffraction technique," *Journal of Power Sources*, vol. 285, pp. 156–160, 2015.

[105] J. Akimoto, Y. Takahashi, Y. Gotoh, and S. Mizuta, "Single crystal X-ray diffraction study of the spinel-type $LiMn_2O_4$," *Chemistry of Materials*, vol. 12, pp. 3246–3248, 2000.

[106] X. Sun, X. Q. Yang, M. Balasubramanian, J. McBreen, Y. Xia, and T. Sakai, "In Situ Investigation of Phase Transitions of $Li_{1+y}Mn_2O_4$ Spinel during Li-Ion Extraction and Insertion ," *Journal of The Electrochemical Society*, vol. 149, no. 7, pp. A842–A848, 2002.

[107] M. C. Smart and B. V. Ratnakumar, "Effects of electrolyte composition on lithium plating in lithium-ion cells," *Journal of The Electrochemical Society*, vol. 158, no. 4, pp. A379–A389, 2011.

[108] M. Levi, E. Levi, and D. Aurbach, "The mechanism of lithium intercalation in graphite film electrodes in aprotic media. part 2. potentiostatic intermittent titration and in situ xrd studies of the solid-state ionic diffusion," *Journal of Electroanalytical Chemistry*, vol. 421, no. 1, pp. 89 – 97, 1997.

[109] P. C. Goonetilleke, J. P. Zheng, and D. Roy, "Effects of surface-film formation on the electrochemical characteristics of limn2o4 cathodes of lithium ion batteries," *Journal of The Electrochemical Society*, vol. 156, no. 9, pp. A709–A719, 2009.

[110] S.-L. Wu, W. Zhang, X. Song, A. K. Shukla, G. Liu, V. Battaglia, and V. Srinivasan, "High Rate Capability of $Li(Ni_{1/3}Mn_{1/3}Co_{1/3})O_2$ Electrode for Li-Ion Batteries," *Journal of The Electrochemical Society*, vol. 159, no. 4, pp. A438–A444, 2012.

[111] D. Aurbach, A. Zaban, Y. Ein-Eli, I. Weissman, O. Chusid, B. Markovsky, M. Levi, E. Levi, A. Schechter, and E. Granot, "Recent studies on the correlation between surface chemistry, morphology, three-dimensional structures and performance of Li and Li-C intercalation anodes in several important electrolyte systems," *Journal of Power Sources*, vol. 68, no. 1, pp. 91 – 98, 1997.

[112] B. Tjaden, S. J. Cooper, D. J. Brett, D. Kramer, and P. R. Shearing, "On the origin and application of the bruggeman correlation for analysing transport phenomena in electrochemical systems," *Current Opinion in Chemical Engineering*, vol. 12, pp. 44 – 51, 2016.

[113] P. Keil, S. F. Schuster, J. Wilhelm, J. Travi, A. Hauser, R. C. Karl, and A. Jossen, "Calendar aging of lithium-ion batteries: I. impact of the graphite anode on capacity fade," *Journal of The Electrochemical Society*, vol. 163, no. 9, pp. A1872–A1880, 2016.

[114] Y. Ito, K. Sato, A. Tamai, and K. Nakao, "Unexpected relation between degradation rate of lithium ion battery and stage structure of graphite anode," *Meeting Abstracts*, vol. MA2018-02, no. 4, p. 216, 2018.

[115] E. Wikner and T. Thiringer, "Extending battery lifetime by avoiding high soc," *Applied Sciences*, vol. 8, no. 10, 2018.

[116] J. Bates and D. Leibling, "Spaced out perspectives on parking policy," 2012.

[117] E. Björklund, *Avoiding ageing: Surface degradation of commercial electrode materials in lithium-ion batteries*. PhD thesis, Uppsala University, Structural Chemistry, 2019.

[118] E. Björklund, "Insights into the surface chemistry of $LiNi_{0.33}Mn_{0.33}Co_{0.33}O_2$ in Li-ion cells," 2017. Licentiate thesis.